The Pennsylvania State University

The Graduate School

College of Earth and Mineral Sciences

FRICTION AND PERMEABILITY EVOLUTION OF FRACUTRES AND FAULTS DURING STATIC REPOSE AND DYNAMIC REACTIVATION

A Dissertation in

Energy and Mineral Engineering

by

Kyungjae Im

Submitted in Partial Fulfillment
of the Requirements
for the Degree of

Doctor of Philosophy

May 2019

The dissertation of Kyungjae Im was reviewed and approved* by the following:

Derek Elsworth
Professor of Energy and Mineral Engineering and Professor of Geosciences
Dissertation Advisor
Chair of Committee

Chris Marone
Professor of Geosciences

Demian Saffer
Professor of Geosciences

Shimin Liu
Associate Professor of Energy and Mineral Engineering

Sanjay Srinivasan
Professor of Petroleum and Natural Gas Engineering
Head of the Department of Energy and Mineral Engineering

*Signatures are on file in the Graduate School.

ABSTRACT

The co-evolution of fault/fracture friction and permeability represent important science/engineering challenges impacting natural and engineered systems. Friction directly controls the characteristics of natural fault slip, including inter-seismic healing, slow creep and earthquake rupture. Permeability evolution during fault slip and repose illuminates our understanding of perturbations to the earthquake-modulated natural hydraulic system and of subsurface engineering in recovering both shale gas and geothermal energy and in the safe subsurface sequestration of CO_2. However, mechanisms controlling the evolution of friction and permeability during slow slip, fast rupture and inter-event repose are not clearly understood. For instance, the evolution of stick-slip amplitudes and recurrence, the role of inertia and its influence on frictional stability and the interdependence of these processes remain unclear. Furthermore, mechanisms of permeability evolution during the earthquake cycle (repose through rupture) are also poorly understood since they are influenced in a complex way by chemo-mechanical effects such as elastic/plastic compaction, shear comminution, mechanical dilation, pressure solution and stress corrosion. In this study, we explore fracture friction and permeability evolution during static and dynamic reactivation using both numerical and experimental approaches. This is described in the four chapters of this dissertation.

Chapters 1 and 2 explore inter-seismic frictional healing, co-seismic stress drop and the role of inertia on unstable sliding.

In Chapter 1, we investigate the direct linkage between stick-slip evolution and rate-and-state friction parameters via a novel numerical method. We use RSF (rate and state friction) laws to demonstrate that the back-projected time of null-healing intrinsically scales with the initial frictional state θ_i. We explore this behavior and its implications for: 1) the short-term cutoff time of frictional healing and 2) the connection between healing rates derived from stick-slip sliding versus slide-hold-slide tests. We use a novel, continuous solution of RSF for a one-dimensional spring-slider system with inertia. The numerical solution continuously traces frictional state evolution (and healing) and shows that stick-slip cut-off time also scales with frictional state at the conclusion of the dynamic slip process $\theta_i\,(=D_c/V_{peak})$. This numerical investigation on the origins of stick slip response is verified by comparing laboratory data for a range of peak slip velocities. Slower slip motions yield lesser magnitude of friction drop at a given time due to higher frictional state at the end of each slip event. Our results provide insight on the origin of log-linear stick slip evolution and suggest an approach to estimating the critical slip distance on faults that exhibit gradual accelerations, such as for slow earthquakes.

In Chapter 2, unstable frictional slip motions are investigated with a rate and state friction law across the transition from quasi-static (slowly loaded) slip to dynamic slip, dominated by inertia. Using a novel numerical method, we conduct simulations to investigate the roles of inertial and quasistatic factors of the critical stiffness defining the transition to instability, K_c. Our simulations confirm theoretical estimates of K_c, which is dependent on mass and velocity. Furthermore, we show that unstable slip motion has two distinct dynamic regimes with characteristic limit cycles: (i) stick-slip motions in the quasi-static (slowly loaded) regime and (ii) quasi-harmonic oscillations in the dynamic (fast

loaded) regime. Simulation results show that the regimes are divided by the frictional instability coefficient, $\eta = MV^2/\sigma a D_c$ and stiffness of the system K. The quasi-static regime is governed by the ratio K/K_c and both the period and magnitude of stick-slip cycles decrease with increasing loading rate. In the dynamic regime, slip occurs in harmonic limit cycles, the frequency of which increases with loading velocity to a limit set by the natural frequency of the system. Our results illuminate the origin of the broad spectrum of slip behaviors observed for systems ranging from manufacturing equipment to automobiles and tectonic faults, with particular focus on the role of elasto-frictional coupling in dictating the transition from slow slip to dynamic instability. We highlight distinct characteristics of friction-induced slip motions (stick-slip and friction-induced vibration) and show that the dynamic frictional instability coefficient (η) is a key parameter that both defines the potential for instability and determines the dynamic characteristics of instability.

Chapters 3 and 4 experimentally explore the evolution of fracture transport properties with concurrent measurement of friction and permeability during static and dynamic reactivation.

In Chapter 3, we show that the evolution of permeability on fractures and faults during the full earthquake cycle is sensitive to sealing during the repose phase. We explore the combined effect of static loading followed by fracture reactivation on permeability evolution via slide-hold-slide experiments. During the hold periods, permeability exhibits a slow but continuous reduction. The permeability decay is consistent with power law compaction of the aperture coupled with cubic law flow. With increasing hold periods, permeability evolves following reactivation from net reduction to net increase with the magnitude of the permeability change dependent on the hold period. This implies that the

tight interlocking of asperities during inter-seismic repose primes the fault for permeability enhancement following reactivation. The inferred mechanism is *via* shear dilation with the probable involvement of unclogging. This result identifies that pre-slip sealing during repose is an essential component in the cyclic permeability evolution throughout the seismic cycle.

The cyclic growth and decay of permeability is further investigated in Chapter 4. We conduct slide-hold-slide experiments that are constrained by measurements of fracture normal deformation and optical surface profilometry. Overall, we observe continuous permeability decay during repose periods (holds) and significant permeability enhancement during reactivation (slide). The permeability decay is accompanied by fault normal compaction. Both hydraulic aperture change (Δb_h) and measured compaction (Δb_s) are consistent with time dependent power law closure with a power exponent of ~0.2-0.4. These dual compaction magnitudes are positively correlated but $\Delta b_h > \Delta b_s$ in late stage holds. Permeability enhancement during shear reactivation is typically also accompanied by fault dilation. However, we also observe some cases where changes in hydraulic aperture and permeability decouple from the measured normal deformation, conceivably driven by mobilization of wear products and influenced by the development of flow bottlenecks. Pre- and post-test surface profiles show that the surface topography of the fractures is planed-down by shear removal. However, the flattened surfaces retain small scale roughness with mating and intergrowth anticipated to develop during the observed slow compaction. Flow simulations, constrained by the surface topography and measured deformation, indicate that small-scale roughness may control permeability at flow bottlenecks within a dominant flow channel. These results suggest cycles of permeability creation and destruction are an intrinsic component of the natural hydraulic system present in faults and fractures and provide an improved mechanistic understanding of the evolution of permeability during fault repose and reactivation.

The chapters of this dissertation correspond with a series of four papers either published or in-submittal. By the order of chapter appearance, these papers are:

Im, K., Elsworth, D., Marone, C., Leeman, J. (2017) The impact of frictional healing on stick-slip recurrence interval and stress drop: Implications for earthquake scaling. **J. Geophys. Res: Solid Earth.** *DOI: 10.1002/2017JB014476*

Im, K., Marone, C., Elsworth, D., (2019) The transition from steady frictional sliding to inertia-dominated instability with rate and state friction. **Journal of the Mechanics and Physics of Solids.** *DOI: 10.1016/j.jmps.2018.08.026*

Im, K., Elsworth, D., Fang, Y. (2018) The influence of pre-slip sealing on the evolution of permeability on fractures and faults. **Geophys. Res. Lett.** *DOI:10.1002/2017GL076216*

Im, K., Elsworth, D., Wang, C., Experimental observation of permeability evolution of fracture and fault during repose and reactivation. **J. Geophys. Res: Solid Earth.** *In-revision*

TABLE OF CONTENTS

LIST OF FIGURES

LIST OF TABLES

ACKNOWLEDGEMENTS

Chapter 1

The Impact of Frictional Healing on Stick-Slip Recurrence Interval and Stress Drop: Implications for Earthquake Scaling

Abstract

Interseismic frictional healing is an essential process in the seismic cycle. Observations of both natural and laboratory earthquakes demonstrate that the magnitude of stress drop scales with the logarithm of recurrence time, which is a cornerstone of the rate and state friction (RSF) laws. However, the origin of this log-linear behavior and short time "cut-off" for small recurrence intervals remains poorly understood. Here we use RSF laws to demonstrate that the back-projected time of null-healing intrinsically scales with the initial frictional state θi. We explore this behavior and its implications for: 1) the short-term cutoff time of frictional healing and 2) the connection between healing rates derived from stick-slip sliding versus slide-hold-slide tests. We use a novel, continuous solution of RSF for a one-dimensional spring-slider system with inertia. The numerical solution continuously traces frictional state evolution (and healing) and shows that stick-slip cut-off time also scales with frictional state at the conclusion of the dynamic slip process θi (=Dc/Vpeak). This numerical investigation on the origins of stick slip response is verified by comparing laboratory data for a range of peak slip velocities. Slower slip motions yield lesser magnitude of friction drop at a given time due to higher frictional state at the end of each slip event. Our results provide insight on the origin of log-linear stick slip evolution and suggest an approach to estimating the critical slip distance on faults that exhibit gradual accelerations, such as for slow earthquakes.

1. Introduction

Stick-slip frictional instability is a fundamental mechanism contributing to our understanding of the earthquake cycle [Brace and Byerlee, 1966; Scholz, 1998]. Periodicity of seismic recurrence and magnitude is widely observed in natural earthquake events [e.g., Schwartz and Coppersmith, 1984; Nadeau and Johnson, 1998; Rubinstein et al., 2012], corresponding to general characteristics of laboratory stick-slip observations. Laboratory observations demonstrate that the magnitude of periodic slip events increase linearly with the logarithm of recurrence time and define a cut-off time where the log-linear trend is back-projected to null healing [Scholz and Engelder, 1976; Karner and Marone, 2000; Ben-David et al., 2010; Beeler et al., 2014; Ikari et al., 2016a]. Interseismic fault healing includes frictional and lithification processes that dictate the trend of slip magnitude (or stress drop) with the logarithm of seismic recurrence interval [Scholz et al., 1986; Vidale et al., 1994; McLaskey et al., 2012]. The slope of the slip magnitude to log time relation can be described in the context of rate and state friction [Marone, 1998a; Beeler et al., 2001]. However, the cut-off time, an essential element in understanding the evolution of earthquake periodicity and magnitude remains poorly understood.

Laboratory friction experiments to explore fault healing (slide-hold-slide experiments) demonstrate a log-linear trend for waiting time vs. peak or ‘static’ friction, with a cut-off time for short aging durations [Dieterich, 1972; Scholz and Engelder, 1976]. A variety of micro-mechanisms have been suggested for the log-linear rate of healing, including growth in the real area of contact and plastic deformation between asperities [Dieterich and Kilgore, 1994; Beeler et al., 1994; Yasuhara et al., 2005; Karner and Marone, 2001; Sleep, 2006; Baumberger and Caroli, 2006; Ikari et al., 2016a; Perfettini and

Molinari 2017]. The same log-linear trends are apparent in stick-slip data recorded at different driving rates and thus different slick-slip recurrence times [e.g., Wong and Zhao, 1990; Karner and Marone, 2000; Mair et al., 2002; Beeler et al., 2014]. The common log-linear dependency observed in slide-hold-slide and stick-slip experiments is logically a consequence of the intervention of frictional healing between successive slip events. However, much work remains to develop a fundamental understanding of healing behavior during the ’stick’ portion of the stick-slip cycle. For instance, the cut-off time for healing in laboratory experiments is typically of the order of $10^{-1} \sim 10$ s [Marone and Saffer, 2015] while for stick-slip this is typically $10^{-3} \sim 10^{-4}$ s [Scuderi et al., 2015&2016; Leeman et al., 2014]. One of the purposes of this paper is to illuminate the origin of such discrepancies.

Laboratory cut-off times for frictional healing are known to be dependent on slip velocity [Marone, 1998b], humidity [Frye and Marone, 2002] and temperature [Blanpied et al., 1998; Nakatani and Scholz, 2004; Yasuhara et al., 2005]. The cut-off time may be expressed by introducing an initial effective contact lifetime that can be represented by prior slip velocity and a characteristic length of a surface asperity [Rabinowicz, 1951; Brechet and Estrin, 1994; Estrin and Brechet, 1996; Rice et al., 2001; Baumberger and Caroli, 2006; Nakatani and Scholz, 2006; Bar-Sinai et al. 2014]. This velocity dependency is also a consequence of rate and state friction and corresponds with laboratory observations [Marone, 1998b] - suggesting that the healing cut-off behavior is a natural consequence of rate and state frictional response. The velocity dependency of the early-time cut-off for healing may be extended to stick-slip motion as previously discussed [Nakatani and Scholz, 2006; Bar-Sinai et al. 2014; Ikari et al., 2016a].

The evolution of healing during the inter-seismic period may be illuminated by numerical simulation of stick-slip motion using rate and state friction laws. However, inertia-controlled stick-slip models have so far required that slow and fast regimes be analyzed separately [Rice and Tse, 1986; Roy and Marone, 1996; He et al., 2003]. These results are inherently dependent on the pre-selection of a slip regime, making the analysis of the full spectrum of stick (slow) and slip (fast/inertial) regimes in a common framework, difficult.

In the following we demonstrate that the observed cut-off time should intrinsically scale with initial frictional state as defined by rate and state friction. We explore this with the analysis of healing and stick slip behavior under a common inertial framework for rate and state friction and confirm this response with laboratory observations.

2. Frictional Healing and Rate and State Friction Laws

Rate and state friction (RSF) laws describe the dependence of frictional resistance on slip velocity (*V*) and an evolving state variable (*θ*). The most widely used form is, [Deiterich, 1979; Ruina, 1983]

$$\mu = \mu_0 + a\ln\left(\frac{V}{V_0}\right) + b\ln\left(\frac{V_0\theta}{D_c}\right) \tag{1}$$

where μ_0 is a reference friction coefficient corresponding to a reference slip velocity V_0, D_c is a critical slip distance and *a* and *b* are non-dimensional parameters that define the magnitudes of the direct (*V* dependent) and evolving (*θ* dependent) effects, respectively. The velocity dependent term is known to depend on activation energy (Arrhenius relationship) [Rice et al., 2001], and the state (*θ*) dependent term is interpreted in terms of changes in real area of contact that scale proportionally to the logarithm of contact age

[Dieterich and Kilgore, 1994;; Ben-David et al., 2010; Ikari et al., 2016a; Svetlizky et al., 2017; Perfettini and Molinari, 2017].

The evolution of friction following a perturbation in slip velocity, for example during cyclic stick-slip sliding, is defined by the evolution of the state variable θ. When the initial reference state θ_i evolves to $\theta_i + \Delta\theta$, the change in friction $\Delta\mu$ due to the evolving effect only (assuming constant hypothetical slip speed V) is given by,

$$\Delta\mu = b\ln\left(\frac{\theta_i + \Delta\theta}{\theta_i}\right) \tag{2}$$

defining a fundamental relation for the rate of frictional healing. Here, the evolution of the state, $\Delta\theta$, is defined by the evolution law as discussed below. Equation 2 shows that the magnitude of healing is innately dependent on the initial state θ_i. When an increment of the state $\Delta\theta$ is small compared to the initial state θ_i, Equation 2 shows that $\Delta\mu$ approaches zero and the magnitude of frictional healing is negligible.

Laboratory experiments and widely used friction state evolution laws show that friction and frictional state (with dimensions of time) evolve with slip and waiting time during slide-hold-slide motion, yielding a log-linear relation between the increase of friction and wait time [Dieterich, 1972, Scholz, 1998]. The log-linear nature of healing shows that the rate of frictional strengthening is large on weakly healed surfaces (where the real area of contact at asperities is small) and conversely small on strongly healed surfaces [e.g., Ikari et al., 2016a]. For sufficiently short waiting times between slip events, the increase in friction is negligible, which defines a short term “cut-off” for frictional healing. This cut-off time is a natural consequence of the logarithmic evolution of frictional state from its initial value. In particular, note that in Equation 2, when initial frictional healing is weak (small θ_i), even a small increase in the frictional "state" ($\Delta\theta$) may yield significant healing. Conversely, if the initial frictional healing is strong, a significant evolution of the state ($\Delta\theta$) is required to yield an observable change in friction, implying that the cut-off time should be scaled to the initial state θ_i. Note that this scaling relation may be generally applied to any state evolution law where $\Delta\theta$ evolves with time.

The evolution of the state variable $\Delta\theta$ is described by two widely-used laws, denoted [Marone, 1998a], as the Dieterich (aging) law [Dieterich, 1979],

$$\frac{d\theta}{dt} = 1 - \frac{V\theta}{D_c} \tag{3}$$

and the Ruina (slip) law [Ruina, 1983]

$$\frac{d\theta}{dt} = -\frac{V\theta}{D_c}\ln\left(\frac{V\theta}{D_c}\right). \tag{4}$$

Both evolution laws return a positive rate of frictional healing ($d\theta/dt > 0$) for a decrease in slip velocity from steady state ($V < D_c/\theta$). For small perturbations around steady state ($\theta \sim D_c/V$) the two evolution laws are similar but they diverge substantially as velocity approaches zero ($V << \theta/D_c$). For the slip evolution law (Ruina), the state variable evolves only at non-zero velocity while the aging law (Dieterich) delivers maximum healing for a static system ($V = 0$).

Figure 1-1 shows a quasi-static simulation of slide-hold-slide motion to illustrate the evolution of friction and frictional healing for both state evolution laws. These are conducted with rate and state parameters best fit to the data in Figure 1-3 [Marone, 1998b] (μ_0=0.7, V_0=10 µm/s, a=0.0066, b=0.0083 and D_c=7.1µm/s and with a system stiffness of

k=1×10^{-3}/μm (k is spring stiffness normalized by normal stress)). The system is initially at steady state (for 5 seconds) with a loading velocity of V_{lp}=10 μm/s before V_{lp} is decremented to zero for 10 seconds before the loading again resumes (Figure 1-1). The solid line denotes the frictional response (rate and state friction, Equation 1) and the dashed line denotes the expected evolution of friction due to healing (Equation 2) from an initial steady state $\theta_i = D_c/V_{ss}$ where V_{ss} denotes steady state velocity prior to hold (i.e. V_{lp} at 'slide'). During the hold period, frictional surfaces heal and frictional state θ increases according to the evolution laws (Figure 1-1) while the measured coefficient of friction decreases because the direct frictional effect (associated with the decrease in slip velocity) dominates over the state evolution healing effect. When loading resumes, the velocity effect and the state evolution that occurred during the hold period are immediately apparent (Figure 1-1) and together yield a peak value of friction, which in past studies was referred to as time dependent 'static' friction [e.g., Coulomb, 1785; Rabinowicz, 1951; 1956].

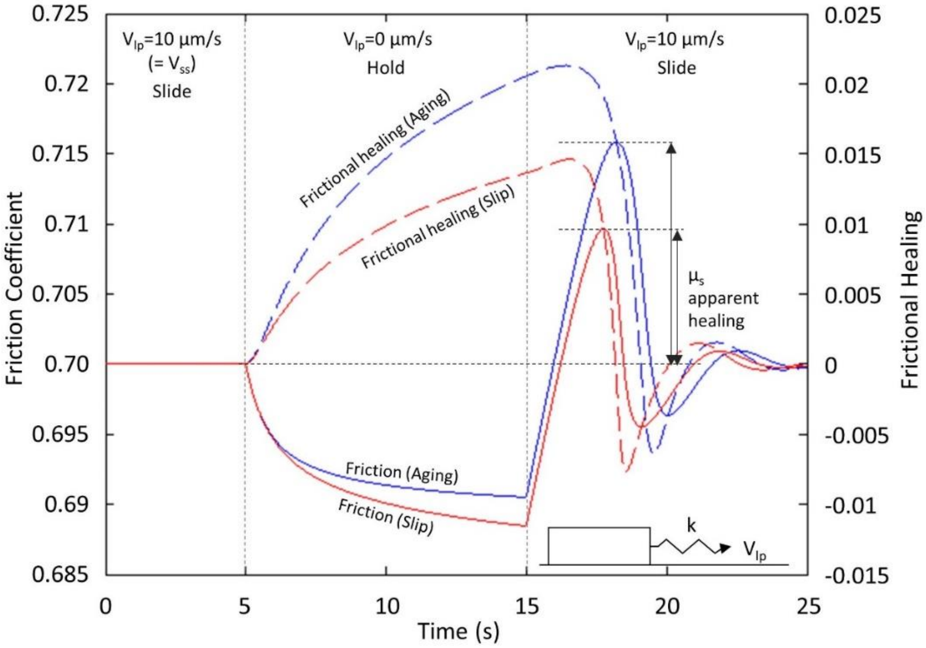

Figure 1-1 Evolution of friction (solid line) and theoretical frictional healing (dashed line) during a slide-hold-slide experiment for a spring-slider system. Laboratory experiments measure apparent healing, which includes both increased frictional state due to healing during quasi-stationary contact and weakening associated with renewed slip. Red lines are Ruina slip law; blues lines are Dieterich aging law.

In the laboratory and on tectonic faults, the effect of frictional healing on shear strength is defined by the observed peak strength. In laboratory slide-hold-slide (SHS) experiments, $\Delta\mu$ ("apparent" healing) is defined as the difference between peak friction and the initial steady state friction (Figure 1-1). Figure 1-1 shows that peak friction in a SHS test is determined by both "actual" frictional healing (dashed line) and the reduction in frictional strength associated with the decrease in frictional state during the acceleration stage before the peak.

Laboratory observations of apparent healing have a linear relation with the logarithm of hold time t_h and may be represented by two constants t_c and β [Dieterich, 1972],

$$\mu_s = \beta \ln\left(\frac{t_h}{t_c}+1\right) \qquad (5)$$

where t_c denotes cut-off time and β denotes the log-linear healing rate. Note that Equation 5 is typically expressed with $\log_{10}$, but we use natural log for consistency with rate and state healing and so that Equations 2 and 5 are described in the same form. Slide-hold-slide experiments confirm that t_c is dependent on steady state slip velocity (V_{ss}) prior to hold [Marone, 1998b]. Also, t_c may be dependent on a characteristic length scale for the asperity population, often defined as "*D*" which is strongly connected to D_c [Nakatani and Scholz, 2006; Marone et al., 2009]. Both of these (V_{ss} and D_c) dependencies are implied from rate and state healing. In typical slide hold slide experiments, the system is set to steady state prior to the application of a hold, i.e., $\theta_i = D_c/V_{ss}$ and Equation 2 indicates that the magnitude of healing is intrinsically dependent on θ_i.

Comparing the change in frictional state $\Delta\theta$ with laboratory healing observation would allow the constants t_c and β to be defined and may suggest which evolution law returns better results. Intriguingly, both evolution laws provide plausible results corresponding to the laboratory observations. The Dieterich aging law innately represents log-linear frictional strengthening for stationary contact. Equation 3 describes $d\theta \sim dt$ when sliding velocity decreases rapidly from an initial condition of steady-state sliding. Substituting this relation into Equation 2 shows, quite simply, that log-linear healing occurs when dt is larger than the initial frictional state θ_i. Conversely, for the Ruina slip law, healing only evolves at finite velocity, such as would be expected during quasi-static creep. Although the 'hold' period in an SHS experiment begins when loading rate is set to zero, the slider velocity never actually reaches zero for a system with finite stiffness. Instead, the fault slip rate and the shear force driving slip decrease continuously with creep motion. Numerical studies indicate that both state evolution laws can plausibly explain laboratory observed healing with time [Marone and Saffer, 2015; Bhattacharya et al., 2017].

The desired evolution law may be determined by other (non-SHS) experimental observations. However, existing evidence is still ambiguous. The response to the Dietrich aging law is supported by direct observation, where the contact area between two stationary surfaces increases in accordance with the description of the aging law [Dieterich and Kilgore, 1994]. Conversely, recent observations from friction response with large velocity steps favor the use of the slip law [Bayart et al., 2006; Rathbun and Marone, 2013; Bhattacharya et al., 2015].

For either law, the complete description of frictional strength recovery with time and (creep) slip, given by Equation 5, depends on the full suite of rate and state parameters a, b, D_c and the elastic stiffness of the fault zone and surroundings [see Marone and Saffer, 2015 for a recent review]. Although critical evaluation of the state evolution law, with possible modification, is beyond the scope of this study, we focus on the need to better understand the origin of log linear healing and the term t_c of Equation 5. Here, we employ numerical experiments and RSF laws to study frictional healing, with particular focus on the parameter t_c. We show that t_c can be predicted by the initial value of frictional state θ_i in Equation 2 for both of the state evolution laws.

Rate and state friction laws indicate that fault healing is observed when $\Delta\theta$ is comparably larger than the initial frictional state θ_i (i.e. D_c/V_{ss} during slide hold slide experiments where V_{ss} denotes V_{lp} prior to hold). We conducted simulations to illustrate the dependency of healing on the parameters D_c and V_{ss} (Figure 1-2). These numerical investigations simulate apparent frictional healing during SHS tests for a range of D_c and sliding velocity values. Figure 1-2 shows the behavior for both state evolution laws and RSF parameters a = 0.007, b = 0.01 and k = 3×10^{-3}/µm (where k is the elastic stiffness normalized by stress). Figure 1-2a shows the evolution of healing as a function of D_c (1, 100 µm) and 2b shows the behavior as a function of V_{ss} (1 and 10 µm/s).

Healing rates (slopes) predicted from the two evolution laws are substantially different (Figure 1-2). With the Dieterich aging law, healing rate (per decade) approaches to an asymptote $b\ln(10)$, (*i.e.* $\mu_s \sim b\ln(t_h)$) at long holds, corresponding to previous studies [e.g. Beeler et al., 1994; Marone and Saffer, 2015] and recent arguments by Bhattacharya et al. [2017]. The healing rate is smaller for the Ruina slip law and is significantly dependent on D_c (Figure 1-2a). Also, the healing rate slightly increases with duration of hold time for the slip law (especially with large D_c). Although the slip law appears to violate the log-linear nature of healing, we note that the non-linearity is greatest at early times which is consistent with laboratory observations and such healing rate increases at long hold times are also experimentally reported [e.g. Carpenter et al., 2014; Ikari et al., 2016b].

Notably, the healing rate simulations can be re-scaled to reveal a non-dimensional hold time or hold-slip, consistent with previous work [Marone, 1998b; Marone and Saffer, 2015]. Figure 1-2 shows that the SHS healing data translate horizontally in proportion to the initial state θ_i regardless of the evolution law. The symbols of Figure 1-2 represent different combinations of V_{ss} and D_c as, circles: V_{ss} = 1 µm/s and D_c = 1 µm, triangles: V_{ss} = 1 µm/s and D_c = 100 µm and squares: V_{ss} = 1 µm/s and D_c = 1 µm. The larger, black symbols on the *x*-axis represent D_c/V_{ss} values for each case (Figure 1-2). Linear trend lines on the aging law (dashed lines), which correspond to long term asymptotic healing rates of previous studies [Bhattacharya et al., 2017], present cut off times that scale with the ratio D_c/V_{ss}. A two-order of magnitude increase in D_c yields a two-order increase in the cut-off time (Figure 1-2a) and one-order of magnitude decrease in velocity yields a 10x increase of cut-off time (Figure 1-2b). Although the trend line cannot be defined from slip law healing, due to its non-linear nature, it is clearly shown that the curves translate horizontally depending on the initial value of frictional state θ_i.

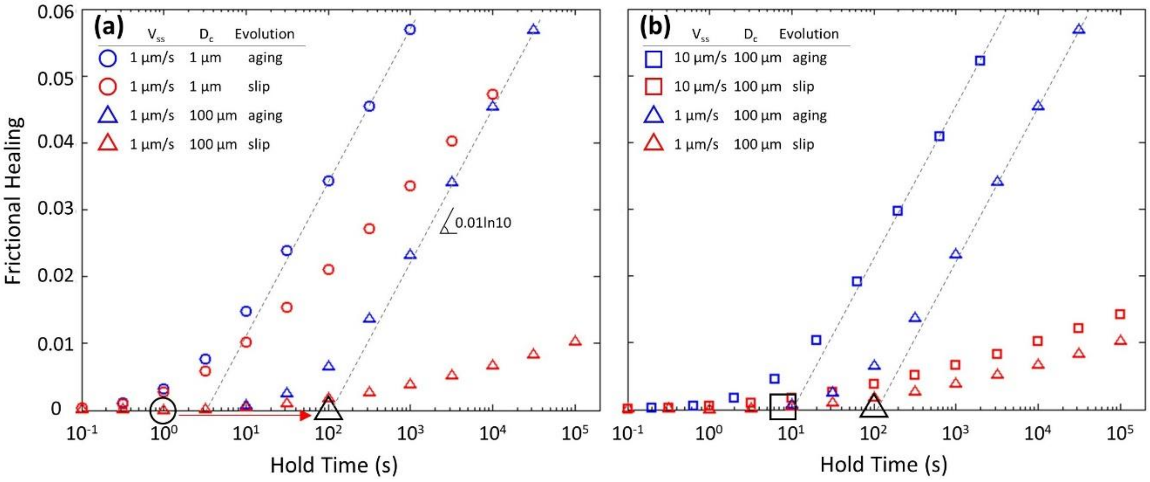

Figure 1-2 Numerical simulation results of apparent healing in SHS experiments. $K/\sigma=3\times10^{-3}$ /μm (normalized stiffness) $a = 0.007$ and $b = 0.01$ with **(a)**: two orders-of-magnitude change in D_c and **(b)**: one order-of-magnitude change in V_{ss}. Symbol colors and shapes denote different input parameters (see key). Black symbols on *x*-axis represent D_c/V_{ss} values of each corresponding case. Dashed lines on aging law are back-projected healing rates based on the two longest hold times in each case.

According to this scaling relation for the cut-off time, assuming log-linear healing, an approximate rate and state frictional healing law may be represented as,

$$\mu_s = \beta \ln\left(1 + \frac{t_h}{\alpha D_c / V_{ss}}\right) \tag{6}$$

where α is a parameter that describes the offset between the cut-off time and D_c/V_{ss} (that is, between the x-intercepts of trend lines and their D_c/V_{ss} on the x-axis in Figure 1-2). In a strict sense, Equation 6 is only valid for the aging law, due to the non-linear nature of the slip law. But we note that slip law healing with small D_c can be (miss-) interpreted as asymptotic on a log-linear plot. The offset α in Equation 6 is dictated by the response time of a system with finite stiffness and, if the system is governed by the slip law, the intrinsically slow rate of state evolution for the slip law may further increase α (moves the curves to the right). In these simulations with the aging law, α is no more than an order of magnitude from unity.

This view assumes that the frictional system obeys RSF with constant parameters. Although this assumption may be acceptable in typical slide-hold-slide experiments, it may not always be valid in nature. Delay or promotion of healing has been observed under hydrothermal condition [Karner et al., 1997; Nakatani and Scholz, 2004; Tenthorey and Cox, 2006; Giger et al., 2008; Chen and Spiers, 2016] and also as a result of the activation of pressure solution [Yashuhara et al., 2005; Neimeijer et al., 2008].

Figure 1-3 compares laboratory observed healing in SHS experiments [Marone, 1998b] with the modified healing law of Equation 6 for two sliding velocities (V_{ss}=1 and 10μm/s). Separately conducted velocity stepping experiments (upper left box) show a critical distance D_c ~7.1μm. Substituting V_{lss} and D_c with the fitting parameters β=0.0042 and α=1 into Equation 6 yields the solid lines of Figure 1-3, which match the laboratory observations (circles) reasonably well.

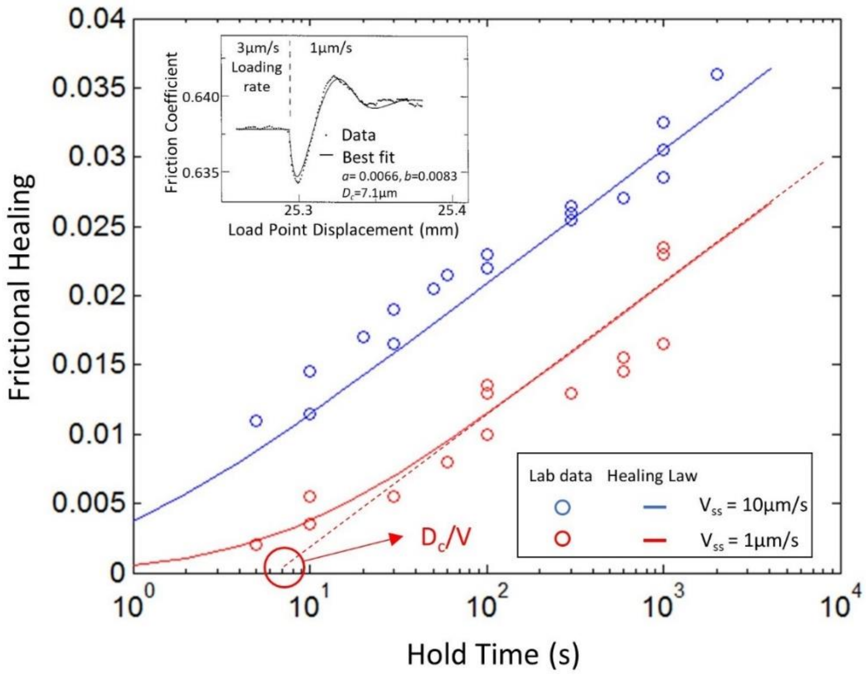

Figure 1-3 Comparison of laboratory measurements of apparent frictional healing [Marone 1998b] and Equation 6. Blue and red symbols represent different loading velocities of V_{ss} = 10 μm/s and V_{ss} = 1 μm/s, respectively. For the healing law, D_c ~ 7.1 μm as measured from velocity stepping experiments (upper left box) in the same study. Solid lines are calculated from Equation 6 using D_c = 7.1 μm, β=0.0042 and α=1. Dashed line is the back-projected trend based on the longest hold times. Plot indicates that D_c/V_{ss} provides a good approximation for the short time cut-off of frictional healing.

3. Numerical Method of Stick-Slip Simulation

In the foregoing we have shown that frictional healing is strongly dependent on the critical slip distance D_c and antecedent slip velocity. This implies that the higher the slip velocity of a preceding earthquake, the larger the immediate frictional healing. Accordingly, in the case of large values of dynamic slip velocity, one would expect a longer interseismic duration and a longer stick-slip recurrence interval - this in turn would result in greater frictional healing and produce a larger stress drop for the anticipated failure (earthquake) event. In the following, we analyze laboratory earthquakes (stick-slip motion) using a unique numerical solution of spring-slider RSF behavior that also accommodates inertia.

Uniquely, this solution spans the full inertial spectrum from slow to fast slip (see Figure S1 and S2), allowing the exploration of relations between healing, recurrence time and stress drop.

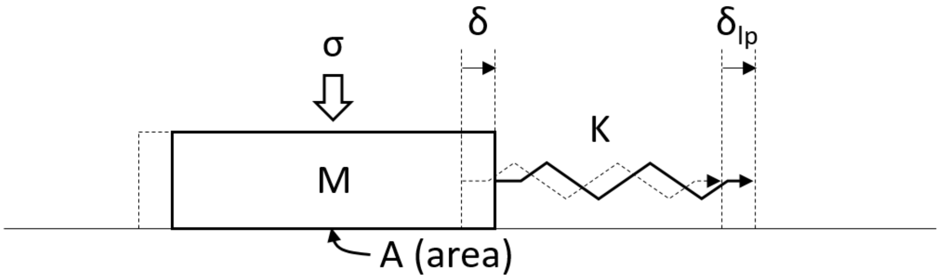

Figure 1-4 Spring-slider system, where δ is displacement of the slider, δlp is displacement of a load point that drives slip, M is mass per unit area A, K is spring stiffness, σ is normal stress at the base of M and A is frictional (contact) surface area. Note that

In a one dimensional spring-slider system (Figure 1-4), the Newtonian force balance governing motion is

$$M\ddot{\delta} = K(\delta_{lp} - \delta) - \mu\sigma \tag{7}$$

where δ is displacement of the slider, δ_{lp} is displacement of the load point, M is mass per unit area (kg/m^2), K is spring stiffness (Pa/m) and σ is normal stress.

Although the stick-slip motion can be simply defined by coupling 3 equations (force balance Equation 7, rate and state Equation 1 and an evolution law as Equation 3 or 4), full solutions for an inertia-dominated system are difficult due to the numerical instability present in the dynamic acceleration process. To condition and thereby improve this stability, we made use of a constant friction solution [e.g., Johnson and Scholz, 1976].

With constant friction μ and load point displacement δ_{lp} and for initial displacement δ_{ini} and velocity V_{ini}, the solution of Equation 7 results in an harmonic oscillation as,

$$\delta(t) = (\delta_{ini} - F)\cos(\omega \mathrm{t}) + \frac{V_{ini}}{\omega}\sin(\omega t) + F \tag{8}$$

where ω is angular velocity defined as $\omega = \sqrt{K/M}$ and $F = \delta_{lp} - \mu\sigma / K$.

We may discretize this equation in time Δt by updating displacement and velocity in each time step as,

$$\delta^{i+1} = [\delta^{i} - (\delta_{lp}{}^{i+1} - \mu^{i+1}\sigma / K)]\cos(\omega\Delta \mathrm{t}) + \frac{V^{i}}{\omega}\sin(\omega\Delta t) + (\delta_{lp}{}^{i+1} - \mu^{i+1}\sigma / K) \tag{9}$$

where superscripts i and $i+1$ denote time steps. Note that load point displacement δ_{lp} can be time dependent in this form since force in the spring is re-calculated in every time step (δ^{i} is updated). Here, friction μ is also discretized in time for further coupling with the rate and state law.

Equation 9 directly provides the displacement in the following time step δ^{i+1} which can be re-substituted for time step i+2. To acquire V^{i+1}, we use the midpoint velocity $V^{i+1/2}$ and acceleration as,

$$V^{i+1/2} = \frac{\delta^{i+1} - \delta^{i}}{\Delta t}. \tag{10}$$

Acceleration between time steps i and i+1/2 is,

$$a = \frac{V^{i+1/2} - V^{i}}{\Delta t / 2}. \tag{11}$$

Assuming that this acceleration is extended to time step *i+1*, the velocity at *i+1* is

$$V^{i+1} = V^{i} + a\Delta t = 2\frac{(\delta^{i+1} - \delta^{i})}{\Delta t} - V^{i}\,. \tag{12}$$

We confirm that coupling Equations 9 and 12 provides an equivalent solution to Equation 8 for small time steps *Δt*, and therefore solves the force balance of Equation 7. Now we further couple the calculated displacement and velocity with rate and state friction. To accomplish this, we begin each time step with the state evolution law. For the Dieterich aging law, we have

$$\theta^{i+1} = \theta^{i} + \left(1 - \frac{V^{i+1}\theta^{i}}{D_c}\right)\Delta t \tag{13}$$

and for the Ruina slip law we have,

$$\theta^{i+1} = \theta^{i} - \left[\frac{V^{i+1}\theta^{i}}{D_c}\log\left(\frac{V^{i+1}\theta^{i}}{D_c}\right)\right]\Delta t\,. \tag{14}$$

For numerical simplicity, we use time step *i* to update the state variable (i.e. $V^{i+1}\cdot\theta^{i}$ in Equations 13 and 14), but a preferred choice will be $V^{i+1}\cdot\theta^{i+1}$ to make the procedure fully implicit. With the Dieterich aging law, the expression for θ^{i+1} can be simply acquired by substituting $V^{i+1}\cdot\theta^{i+1}$ and rearranging Equation 13. An additional numerical procedure is required with the Ruina slip law.

Rate and state friction can be discretized as,

$$\mu^{i+1} = \mu_0 + a\ln\left(\frac{V^{i+1}}{V_0}\right) + b\ln\left(\frac{V_0\theta^{i+1}}{D_c}\right) \tag{15}$$

To track friction as a function of slip and time we couple Equation 13 or 14, 15, 9 and 12 and solve them simultaneously using the Newton-Raphson method until the velocity V^{i+1} converges. We find that the solution satisfies force balance, as illustrated in the following example.

In this method, the velocities in each numerical step are constrained within the solution imposed by force balance ($\Sigma F=ma$). This increases convergence rate and numerical stability. Although restricted here to the two widely-used evolution laws with constant frictional parameters, the method could be extended to accommodate other evolution laws [e.g. Linker and Dieterich, 1992; Nagata et. al., 2012] – and also accommodate strain, slip rate and temperature dependencies of frictional parameters [e.g. Ikari et. al., 2011; Niemeijer et. al., 2016; Svetlizky et. al., 2017].

4. Simulation Results

We conduct a series of numerical simulations using the approach outlined above to illuminate the dependency of healing on prescribed rate and state parameters a, b, D_c and loading rate V_{lp}. To generate unstable stick slip motion, we set $a-b<0$ and $K<K_c$. Here K_c is a critical stiffness that determines slip stability. The critical stiffness of spring slider moving in steady state at velocity V is defined as [Rice and Ruina, 1983; Gu et al., 1984; Roy and Marone 1996]

$$K_c = \frac{(b-a)\sigma}{D_c}\left[1+\frac{MV^2}{\sigma a D_c}\right] \tag{16}$$

where m is mass of the slider. The ‘dynamic’ term (second term in brackets in Equation 16) is negligible in the following study, but we note that it indeed influences stability of stick-slip system (see Figure S2).

In all simulations, initial velocity and frictional state are set to $V_{ini} = V_0$ and $\theta_{ini} = D_c/V_0$ and consequently initial friction is μ_0 (see Equation 1). Given that the arbitrary reference velocity is set as $V_0 = 10^{-9}$m/s, the initial frictional state ($\theta_{ini} = D_c/V_0$) is much larger than at steady state for typical laboratory loading rates $V_{lp} = 10 \sim 1000$ μm/s. Thus, this represents strongly healed surfaces. All simulations initially demonstrate large stress drop due to this strong healing, but the stress drop decreases with the sequence of stick-slip motion and becomes periodic (Figure 1-5). Simulation results with the same set of input parameters yield identical periodic motions regardless of the initial parameter values.

4.1. Stick-slip behavior

Figure 1-5 show results of stick slip with input parameters $\mu_0 = 0.6$, $a = 0.005$, $b = 0.007$, $D_c = 50$ μm $\theta_{initial} = 50000$ s, $\sigma = 1$ MPa, $K = 32$ MPa/m ($0.8K_c$), $V_{lp} = 1$ mm/s and $M = 100$ kg/m^2 for the aging law. Figure 1-5a illustrates stick slip frictional behavior for 20 seconds. The magnitude of the initial frictional drop is significant, due to its high initial healing. The stick-slip behavior becomes nearly perfectly periodic after several cycles. The other panels (b-e) of Figure 1-5 show enlargements of the stick-slip event that is boxed in Figure 1-5a. Each curve in Figure 1-5b denotes a segment of the normalized force balance equation

$$\frac{(\delta_l - \delta)\mathrm{K}}{\sigma} - \frac{M\ddot{\delta}}{\sigma} = \mu \tag{17}$$

which is identical to the Newtonian force balance (Equation 7). The blue curve (Figure 1-5b) denotes the apparent friction (or normalized shear stress, which is the first term on the left hand side of Equation 17) and the red curve (note that it overlaps the black dashed curve) denotes the actual (rate and state) friction, which is the right-hand side of Equation 17. Because the two frictional magnitudes differ due to the large (normalized) inertial force (the second term of the left-hand side of Equation 17), significant decoupling occurs in dynamic slip, with offset proportional to acceleration (Figure 1-5c). The entire left-hand side of Equation 17 is calculated with acceleration (Figure 1-5c) and plotted with the black dashed curve. The curve completely overlaps the red curve in Figure 1-5b, confirming that force balance (Equation 17) is satisfied.

The process of inertia-controlled friction drop can be divided into acceleration and deceleration stages [Gu et al., 1984; Gu and Wong, 1991]. The acceleration is driven by a decrease in frictional state (Fig 5e) in response to increasing velocity. Due to the rapid drop in the frictional state term, the frictional resistance (Figure 1-5b red) becomes smaller than the normalized shear stress (Figure 1-5b blue) and consequently the system accelerates. The magnitude of the friction drop in this acceleration stage is defined as the dynamic friction drop, $\Delta\mu_d$ (See Figure 1-5b). Frictional healing (θ increase) begins at the conclusion of this dynamic friction drop (Figure 1-5e). However, normalized shear stress (apparent friction) continues to decrease due to the inertial effect [e.g., Beeler et al., 2001]. Actual RSF sharply decreases at the conclusion of the slip process due to the velocity effect. This latter part of the friction drop is defined as dynamic overshoot $\Delta\mu_{ov}$ and the total friction drop is defined as the static friction drop, $\Delta\mu_s$ ($=\Delta\mu_d.+\Delta\mu_{ov}$, see Figure 1-5b).

Healing begins at the conclusion of the dynamic friction drop, thus the minimum (and therefore initial) value of frictional state can be observed at maximum velocity. In this specific simulation, the observed minimum value of frictional state is $\theta_i \sim 2.1\times10^{-4}$ s (Figure 1-5e) with a peak velocity of $V_{peak} \sim 0.24$ m/s (Figure 1-5d). Using an input parameter of $D_c=5\times10^{-5}$ m, we find that the steady state relationship $\theta = D_c/V_{peak}$ is satisfied at the initiation of frictional healing.

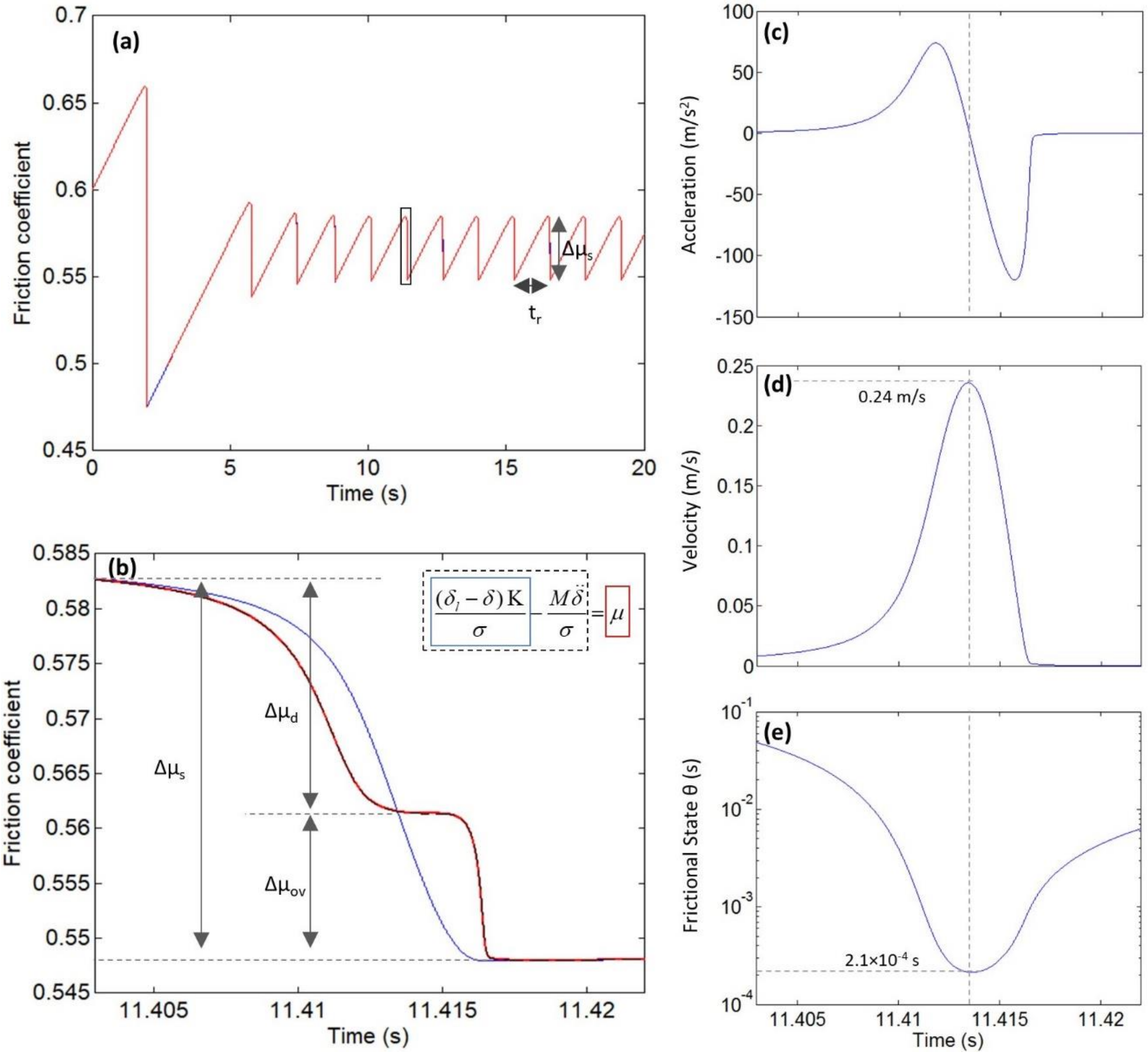

Figure 1-5 Simulation result of stick slip motion. **(a)** Repeated stress build-up and friction-drop during a 20 s period from the initial state. **(b)** Enlargement of one friction drop (rectangle in **a**). Red, blue and black lines denote corresponding terms in the force balance equation shown in the upper inset. Note that red and black curves overlap. The blue curve represents normalized shear stress. Panels **c**, **d** and **e** show velocity, acceleration and state variable during the same period highlighted in **(b)**. Note that state is minimum when slip velocity is maximum and that acceleration/deceleration history is asymmetric.

4.2 Evolution laws and phase diagram

We show simulation results for each state evolution law and for two loading velocities (V_{lp}=0.5 and 5 mm/s) in Figure 1-6. The other RSF parameters are identical to the previous simulation (Figure 1-5). Figure 1-6a and c represent full stick-slip friction behavior and Figure 1-6b and d represent phase diagrams (friction-velocity) of actual friction (rate and state friction, solid line) and apparent friction (normalized shear stress, dashed line). The black dashed lines in the phase diagrams represent steady state where the relation $\theta = D_c/V$ is satisfied.

Point ① in Figures 6a and b represents the initial state, which represents input values $V_{ini} = V_0$ (10^{-9} m/s), $\theta_{ini} = D_c/V_0$ and accordingly, from the rate and state law (Equation 1) $\mu = \mu_0$ (0.6). Friction builds until the slider velocity reaches the loading velocity ① → ② (for the case with V_{lp}=0.5 mm/s). During the dynamic friction drop, velocity rapidly increases and accordingly both actual friction (solid line) and apparent friction (dashed line) decouple due to a large inertial force ② → ③ (highlighted in box figure 1-6a). At this point, friction temporarily reaches a steady state (figure 1-6b black dashed line) at maximum velocity ③ and dynamic overshoot follows ③→④. This frictional build-up and drop is repeated, but this time, with a reduced size of the loop in the phase diagram (④→⑤→⑥→⑦). Note that the magnitude of the friction drop decreases in successive sequences and ultimately stabilizes to a periodic behavior (Figure 1-6).

These simulations demonstrate that greater healing yields longer recurrence time and larger stress drop. For an initially elevated frictional state (θ=50000 s) we find a large initial friction drop in all simulations. Also, the magnitude of the friction drop during periodic motion is larger for slower loading (Figure 1-6), reflecting that a higher degree of healing is induced by a longer recurrence time. Similarly, stress drop and recurrence time are larger and longer with the aging law (Figure 1-6a) compared to the slip law (Figure 1-6c) due to the higher healing rate (see Figures 1-1 and 1-2).

In all simulations, the frictional system remains temporarily at steady state (black dashed line in Figures 6b and d) at the peak velocity of each slip. Accordingly, we can utilize the relationship $\theta_i = D_c/V_{peak}$ to calculate the minimum value of the state variable for each event. Previously, we have shown that frictional healing is strongly dependent on the initial value of the frictional state and therefore, it is expected that the evolution of stress drop during stick-slip motion may also scale to this initial (minimum) value of state θ_i ($=D_c/V_{peak}$).

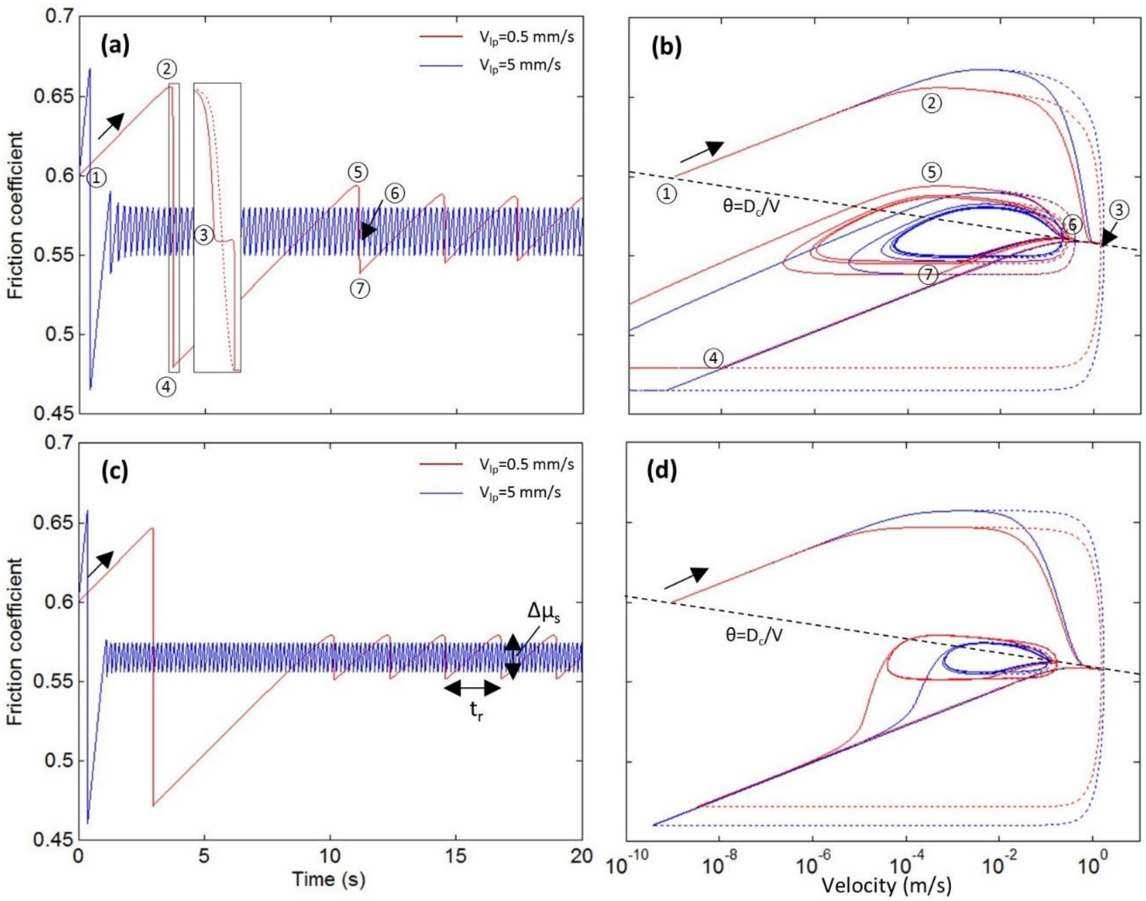

Figure 1-6 Friction response and corresponding phase plane plot (friction-velocity) during stick slip motion with the aging law (**a, b**) and the slip law (**c, d**). Red lines show loading velocity of 0.5 mm/s and blue lines show loading velocity of 5 mm/s. In each case the simulation started from an initial condition of steady sliding at V=10^{-9} m/s. Inset in **(a)** shows a zoom-in of the first stick slip event for loading at 0.5 mm/s. Numbers in upper panels provide fiducial points for comparison. Note that a steady-state stick-slip limit cycle is reached in each case and that the friction drop and velocity excursions scale inversely with loading velocity, reflecting greater frictional healing for lower loading rate.

4.3 Recurrence and friction drop

Figure 1-6 shows that a greater friction drop ($\Delta\mu_s$) is associated with a longer recurrence time (t_r). This is consistent with laboratory data on stick-slip motion, where static stress drop $\Delta\mu_s$ shows a logarithmic dependence on event recurrence time t_r in periodic motion [e.g., Karner and Marone, 2000; Beeler et al., 2001&2014; Ben-David et al., 2012]

$$\Delta\mu_s = (\mathrm{b}-\mathrm{a})(1+\xi)\ln\frac{t_r}{t_0} \tag{18}$$

where t_0 is the empirical cut-off recurrence interval at a projected zero stress drop and ξ represents a factor primarily related to the influence of dynamic overshoot. Equation 18 shows that the slope of the slip-magnitude relation scales with the RSF parameter (*b*-*a*) with a factor of (1+ξ),. The common log-linear dependency of stick-slip (Equation 18) and healing (Equation 5 or 6) suggests that the cut off recurrence interval to a back projected zero stress drop (t_0) may also be scaled with the frictional state at the beginning of healing; this is given by the numerical simulation that $\theta_i = D_c/V_{peak}$.

We conducted multiple stick-slip simulations to determine the relationship between cut-off time and the parameter D_c/V_{peak}. A normal stress σ = 2 MPa was applied for all cases in Figures 7 a, b, c and d (except σ = 20 MPa for D_c = 500 µm to prevent the critical stiffness K_c from becoming too small (Equation 16)). The recurrence time is conditioned by loading velocity - this is varied from 10 µm/s to 1 mm/s (Figure 1-7a), except for the case of D_c = 500 µm where it is varied from 1 mm/s to 2 cm/s (Figure 1-7c). Red and blue symbols and trend lines represent the slip and aging laws, respectively.

We document the evolution of static friction drop vs. recurrence time (Equation 18) for a series of repetitive stick slip events (Figure 1-7). Results reported in each panel (Figure 1-7) use the same parameters except that we vary the RSF parameters *a* and *b* (Figure 1-7a and b), critical distance D_c (Figure 1-7c and d) and critical spring stiffness (Figure 1-7e and f). In figure 1-7e and f, we vary the critical stiffness to explore a range of peak slip velocities during failure, since the stick-slip velocity can be controlled by the ratio of system stiffness and critical stiffness K/K_c [e.g., Leeman et al., 2016]. To mimic the procedure used in laboratory experiments, we use a constant spring stiffness (K = 640 MPa/m) and vary normal stress to change the critical stiffness over the range s σ = 2 MPa, 1.68 MPa and 1.61 MPa yielding $K = 0.8K_c$, $K = 0.95K_c$ and $K = 0.99K_c$ respectively. All plots clearly show that the magnitude of friction drop increases linearly with the logarithm of recurrence time.

Table 1-1 provides our parameter values and the results for the evolution of static stress drop in periodic motion. The evolution rates (stated in natural log $\ln(t_r)$ to enable direct comparison with Equation 18) and cut-off values for each set of simulations are also given in Table 1-1. Note that the log-linear evolution rates of friction drop are not distinct between aging and slip law cases, which is in contrast to observations of slide-hold-slide healing (Figure 1-2). This was similarly reported in previous numerical simulation results [Beeler et al., 2001; He et al., 2003], and shows that the state evolution for healing based on SHS and stick-slip seems to follow a somewhat different path. The healing rates are close to $2(a\text{-}b)$ with both evolution laws, which yields $\xi \sim 1$ in Equation 18. Note that this suggests that ξ embodies more than just dynamic overshoot. The simulation results show that the ratio of dynamic to static stress drop (expressed as friction drop $\Delta\mu_d/\Delta\mu_s$) varies in the range 0.6~0.75, indicating that the dynamic friction drop is larger than the frictional overshoot in the simulations (see Figure 1-5b ratio of $\Delta\mu_s$, $\Delta\mu_d$ and $\Delta\mu_o$).

Table 1-1 Simulation input and resulting slope of the natural logarithm and x-intercept of the friction drop trend line (Figure 1-7)

Evolution Law	D_c (μm)	a	b	K/K_c	Fric. Drop vs. t_r (Figure 1-7 a, c, e)		Fric. Drop vs. $t_r \times V_{peak}$ (Figure 1-7 b, d and f)	
					Slope $\ln(t_r)$	Cut-off (s)	Slope $\ln(t_r \cdot V)$	Cut-off (m)
Slip law	5	0.003	0.005	0.80	0.0038	7.79×10^{-4}	0.0032	1.52×10^{-5}
	5	0.004	0.007	0.80	0.0058	8.08×10^{-4}	0.0049	2.13×10^{-5}
	5	0.005	0.01	0.80	0.0088	4.31×10^{-4}	0.0077	1.88×10^{-5}
	500	0.003	0.005	0.80	0.0038	2.68×10^{-3}	0.0032	1.76×10^{-3}
	5	0.003	0.005	0.95	0.0036	2.22×10^{-3}	0.0029	1.79×10^{-5}
	5	0.003	0.005	0.99	0.0033	3.79×10^{-3}	0.0026	1.43×10^{-5}
Aging law	5	0.003	0.005	0.80	0.0034	1.93×10^{-5}	0.0032	9.72×10^{-7}
	5	0.004	0.007	0.80	0.0050	1.70×10^{-5}	0.0047	1.05×10^{-6}
	5	0.005	0.01	0.80	0.0081	1.65×10^{-5}	0.0076	1.22×10^{-6}
	500	0.003	0.005	0.80	0.0037	1.62×10^{-4}	0.0032	1.52×10^{-5}
	5	0.003	0.005	0.95	0.0030	6.55×10^{-5}	0.0028	1.58×10^{-6}
	5	0.003	0.005	0.99	0.0029	1.57×10^{-4}	0.0032	1.52×10^{-5}

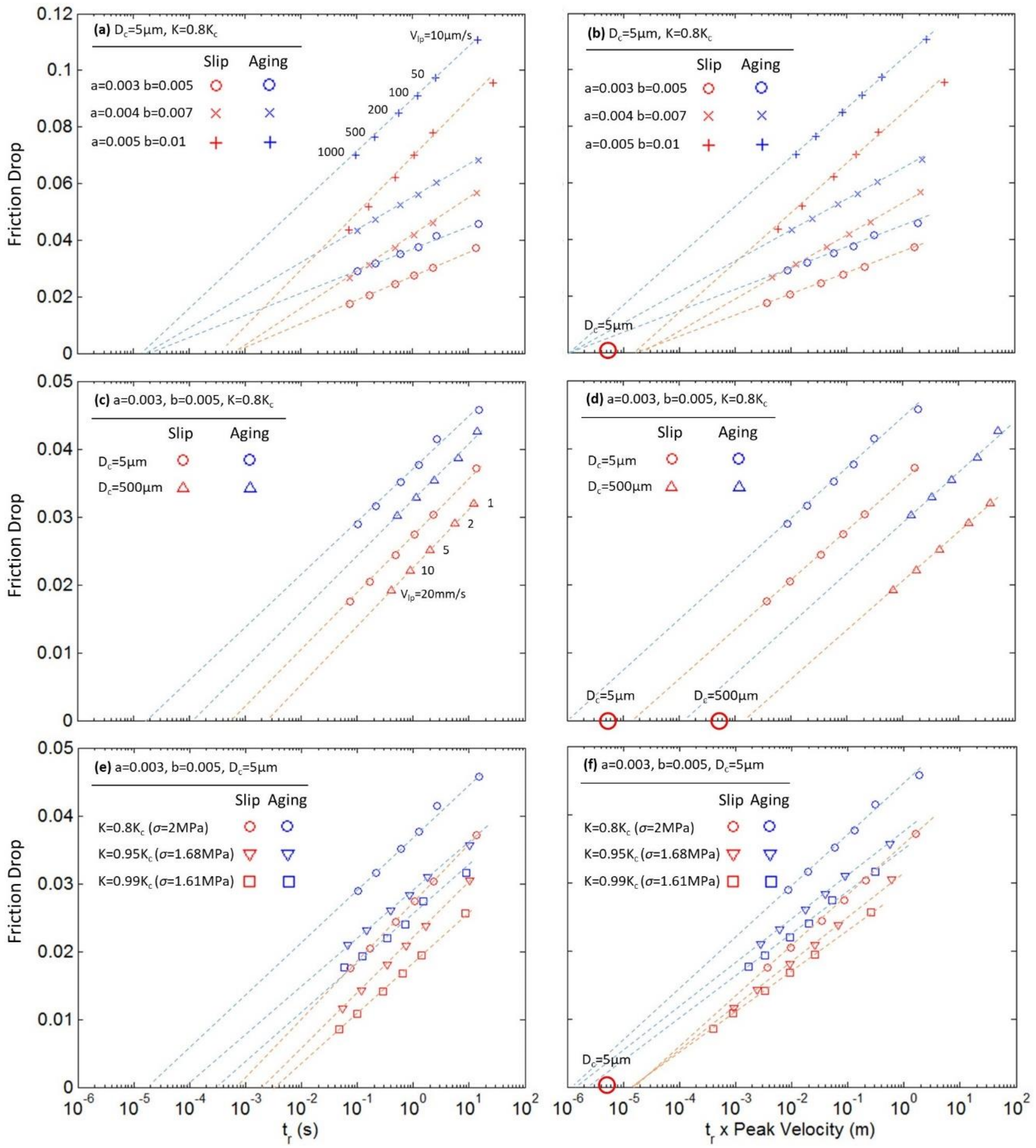

Figure 1-7 Results of stick-slip simulations (e.g., Figure 1-6). (Static) Friction drop $\Delta\mu_s$ is plotted vs. recurrence time (left hand set of panels) and vs. a measure of potential slip given by the product of recurrence time and peak slip velocity (right hand panels). Three sets of parameters are studied: **(a, b)** RSF parameters *a* and *b*, **(c, d)** critical distance D_c, and **(e, f)**: stiffness. Red denotes the slip law and blue denotes the aging law. Recurrence time is varied via loading rate which ranges from 10 to 1000 μm/s in all cases except the case for D_c=500 μm (triangle) in plots c and d. Loading rates are marked in **(a)** and **(c)**. Red circles in panels **(b)**, **(d)** and **(f)** show that the short term cut-off for inter-event frictional healing clearly scales with D_c.

The simulation results suggest that the cut-off time during stick-slip evolution is indeed dependent on D_c and V_{peak}. With the same evolution law, the observed cut-off values clearly diverge when D_c and V_{peak} are different (Figures 7d and f) while they are roughly identical with similar value of D_c and V_{peak} (Figure 1-7b). The difference between aging and slip laws can clearly be observed in the cut-off behavior. Using the same input parameters, the aging law always yields an approximately one order-of-magnitude smaller cut-off time, yielding larger friction drop at a given recurrence time.

Figures 7b, d and f represent the same friction drop with respect to panels a, c and e with peak velocity scaling on the recurrence time of each periodic event. This is intended to remove the velocity effect on the cut-off behavior so that the observed cut-off value can be directly scaled to D_c. Assuming that the stick-slip evolution has a cut-off time at D_c/V_{peak} (*i.e.*, $\Delta\mu_s \sim \ln(t_r/(D_c/V_{peak},))$, then the cut-off value in the plot $\Delta\mu_s$ vs. $\ln(t_r \times V_{peak})$ is required to scale with D_c, only. The plots clearly indicate that all cut-off values of the log-linear trend line are back projected around their input D_c (red circle) value. In the D_c control group (Figure 1-7d), the cut-off values of each evolution law are located adjacent to their input D_c values (D_c=5 μm and 500 μm). The range of cut-off times in Figure 1-7e converge around D_c after multiplication by V_{peak} (Figure 1-7f). These results clearly show that the cut-off time in the evolution of friction drop also scales with D_c/V_{peak}, similarly to the cut-off behavior during the hold portions of slide-hold-slide experiments.

5. Experimental Observations

We perform double direct shear experiments at two different normal stresses of 5 MPa and 7 MPa to confirm the validity of the numerical simulation results. A decrease in normal stress reduces the critical stiffness (Equation 16) and consequently enhances system stability. Laboratory observations on the spectrum of stick-slip modes [Leeman et al., 2016; Scuderi et al., 2016] show that peak slip velocity in the dynamic slip mode drops significantly as system stiffness (K) approaches the critical stiffness (K_c). Using this phenomenon, we successfully generate stick-slip motions with two groups of distinct peak velocities (Figure 1-8). Stick-slip motions with normal stress of 5 MPa always exhibit slow stick-slip ($V_{peak} < 100$ µm/s) while at 7 MPa, the behavior evolves from initially slow (but still faster than the 5 MPa case) to regular (V_{peak} of the order of cm/s) stick slip (Figure 1-8c and d). Further details of the experimental method are reported in Leeman et al. [2016]. An identical experimental configuration and conditions are used except that the loading velocity is varied in these experiments to control the recurrence time (see V_{lp} in figure 1-8a and b).

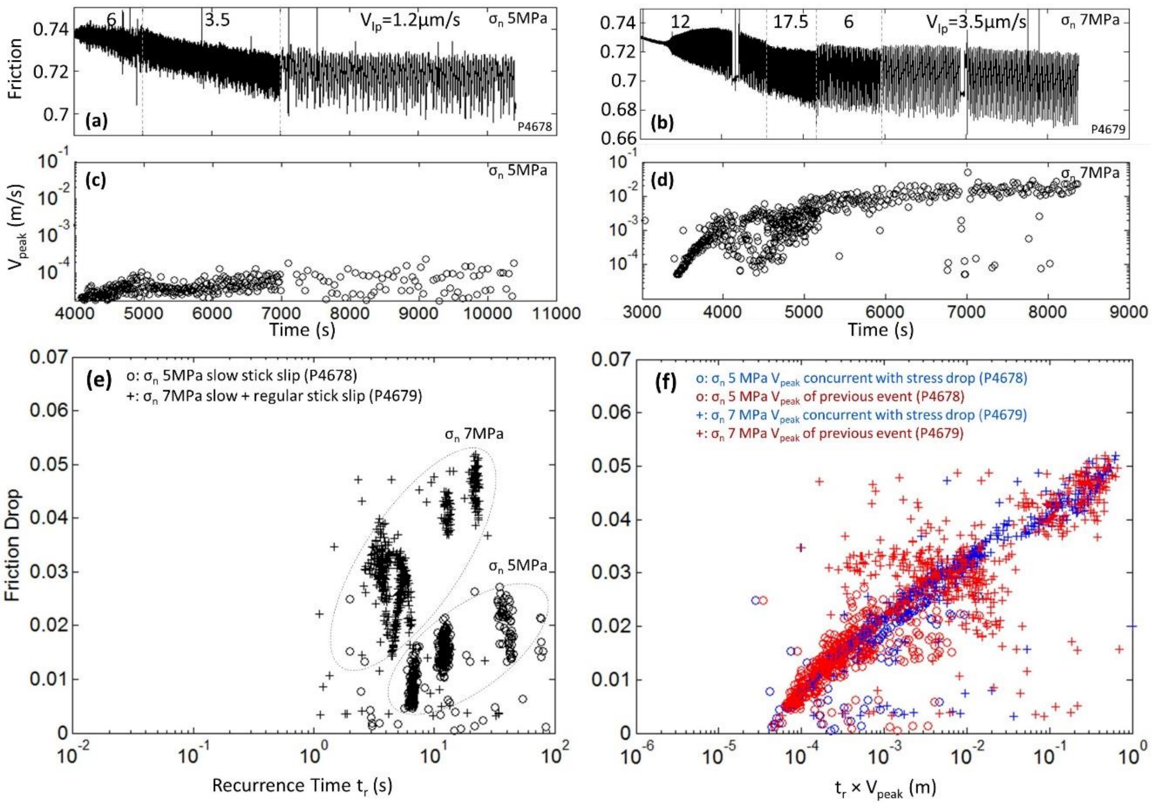

Figure 1-8 Lab data for friction vs time during repetitive stick-slip sliding at 5 MPa (**a**) and 7 MPa case (**b**). Loading velocities are given in each panel. Panels **c** and **d** show peak slip velocity for each slip event. Note that V_{peak} is largest ta 7 MPa and that it varies inversely with loading velocity, reflecting the result of greater inter-event frictional healing at lower loading rates. Panel **e** shows friction drop evolution with recurrence time for the two experiments, 5 MPa (o) and 7 MPa (+). Friction drop generally increases with t_r although the scatter is large. **(f)**: Friction drop vs. $t_r \times V_{peak}$, using concurrent peak velocity (blue) and previous peak velocity (red).

Figure 1-8e represents evolution of friction drop with recurrence time (crosses: 7 MPa, circles: 5MPa). The stick slip motions are not perfectly periodic - rather they are spread vertically - but the magnitude of the stress drop increases with the logarithm of recurrence as observed in the numerical study. This vertical spread is significantly contributed by variation in the peak slip velocity. The friction drop evolution with slow slip (5MPa) is clearly delayed over that of faster slip (7 MPa). This evolution of slip magnitude clearly represents that when peak velocity is high (*i.e.* at 7 MPa), friction drop is greater within a given recurrence interval. The behavior resembles laboratory observations of the healing cut-off behavior (*i.e*. Figure 1-3) implying that rate and state healing governs the stick-slip evolution. This observation suggests that the cut-off time has an inverse relation to peak velocity and supports the prior numerical observation that cut-off time scales to the minimum value of the frictional state θ_i ($=D_c/V_{peak}$).

Recurrence time is multiplied by the peak velocity of each slip event in Figure 1-8f to compensate for velocity variation effect. As discussed for Figures 7b, d and f, if the cut-off time scales with D_c/V_{peak} this will make the cut-off value dependent on D_c, alone. Since the stick-slip is not perfectly periodic, velocities and friction drops vary within the same loading rate. We use peak velocities (V_{peak}) both (i) concurrent with the stress drop event (blue symbols) and (ii) from the previous slip event (red symbols). The velocity of the concurrent event is intrinsically related to the magnitude of the stress drop of the event while the velocity of the previous event may define the initial value of the frictional state and healing. In the numerical simulations, the two effects converge to a periodic stick-slip motion. Figure 1-8f strongly supports the internal mechanistic consistency of the numerical and theoretical explanations of stick-slip evolution. After multiplication of V_{peak}, the two trends for 5 MPa and 7 MPa converge with a single cut-off value. Using the concurrent velocity (blue) shows a distinct linear trend probably due to its intrinsic relation between slip velocity and stress drop. The trend with the previous velocity (red), albeit with some spread, also shows a clear linear trend overall. The scatter appears at $t_r \times V_{peak}$ $10^{-3} \sim 10^{-2}$ m is significantly contributed by occasional non-periodic stick-slip behavior, as observed by velocity variation in Figure 1-8c (7000s ~) and 8d (4000 ~ 5000s). The scatter is strongly reduced in the other ranges that exhibit nearly periodic stick-slips (as implemented in the numerical simulations). The back projected value to zero friction drop (a few tens of microns) is within a reasonable range for an appropriate D_c value of the gouge material used in this experiment (silica powder). These observations imply that the periodicity (friction drop and recurrence) of laboratory stick-slip motion is strongly conditioned by D_c and V_{peak}, i.e. initial value of frictional state.

6. Conclusion

Rate and state frictional response defines frictional healing as a logarithm of the ratio between the initial frictional state (θ_i) and the evolution of this frictional state ($\theta_i+\Delta\theta$). The definition demonstrates an essential and prominent physical property of healing in that frictional strengthening is rapid on weakly healed surfaces (small θ_i) and conversely slow on strongly healed surface (high θ_i). Therefore, for the same change of frictional state ($\Delta\theta$), healing can be significant with a small initial state while it may be negligible at a large initial state. This property suggests that the magnitude of healing at a given time should be scaled to initial state θ_i. In typical slide-hold-slide experiments, θ_i is always regulated by D_c/V_{lp}. We show that in log-linear healing, the cut-off time is scaled to D_c/V_{lp}.

As applied to earthquake faults, our results predict that higher earthquake slip velocity will cause a larger initial rate of frictional healing and therefore longer recurrence time with a given tectonic loading rate. Our novel continuous numerical solution of spring slider motion demonstrates that the cut-off recurrence interval in periodic stick-slip evolution also scales with frictional state at the conclusion of the dynamic slip process and that this frictional state can be evaluated from $\theta_i = D_c/V_{peak}$. Laboratory observations strongly support this explanation of evolution in friction drop. It is clearly shown that when peak velocity is slow the evolution of friction drop is delayed.

Our results suggest that seismic hazard analysis based on the seismic cycle and earthquake periodicity should account for the frictional state at the conclusion of coseismic slip. We show that the magnitude of the anticipated earthquake event is conditioned by healing and modulated by antecedent behavior. Faster and larger healing follows after larger (lower frictional state due to higher peak slip velocity) events and consequently increased recurrence time is expected. The magnitude of the stress drop of the following slip event is determined by the amount of healing that occurs during this interseismic recurrence interval. These processes dictate earthquake periodicity. Both the earthquake magnitude (friction drop) and recurrence in repeating earthquakes are strongly conditioned by the (minimum) frictional state at the conclusion of dynamic friction drop.

Supplementary Material

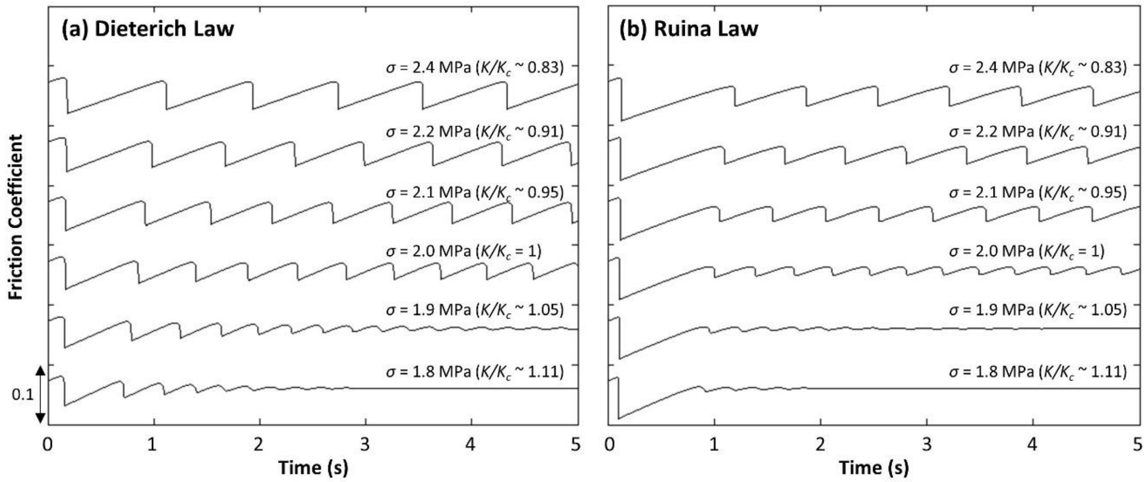

Figure 1-9 Spectrum of fault slip behavior. Simulations are conducted mimicking previous laboratory experiments [Leeman et al., 2016] with (a) Dieterich law and (b) Ruina law. We varied normal stress to cross the stability transition (see Equation 16). Applied normal stresses and consequent stability parameters (K/K_c) are listed above each case. The simulations interrogate the stability threshold from both directions. The results show that the convergence from stick-slip to stable sliding occurs at $K = K_c$. We used rate and state parameters a = 0.003, b = 0.006 and D_c= 20 μm with K= 300 MPa/m, M = 100 kg/m^2 and V_{lp} = 0.5mm/s at initial steady state with V_{ini} = 10 μm/s. With these parameters, the dynamic term of critical stiffness (second term in the brackets in Equation 16) is negligible.

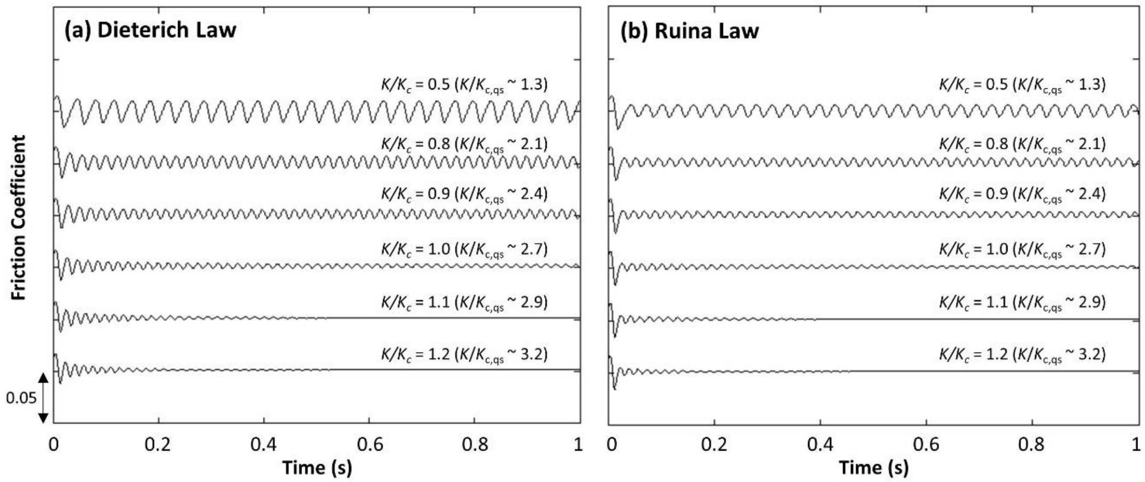

Figure 1-10 Spectrum of fault slip behavior with large mass and high loading rate. We used rate and state parameters a = 0.003, b = 0.006 and D_c= 30 µm with σ = 2 MPa/m, M = 3000 kg/m^2 and V_{lp} = 10 mm/s at initial steady state with V_{ini} = 1 mm/s. In this case, the dynamic critical stiffness (Equation 16) becomes substantially larger than the quasi-static critical stiffness ($K_{c,qs} = (b-a)\sigma/D_c$), K_c~2.7$K_{c,qs}$. Simulations are conducted at constant normal stress with stiffness variation K = 0.5 ~ 1.2K_c. Applied stability parameters (K/K_c) and ratio to quasi-static critical stiffness ($K/K_{c,qs}$) are listed above each case. Note that all cases are conducted at well above the quasi-static critical stiffness. The result show that the convergence from stick-slip to stable sliding occurs at $K = K_c$, where K_c is the dynamic value rather than the quasi-static values.

Simulation code (Matlab 2013)

```
% Inertia controlled spring slider motion simulator with RAS friction
% Written by KJ Im (kxi123@psu.edu, limkjae10@gmail.com)
% Refer to -
% Im, K et al., The effect of frictional healing on stick-slip
% recurrence interval and stress drop: Implications for earthquake scaling
% J. Geophys. Res.

clear all

% Input Parameters
DorR=1; % 1:Dieterich, 2:Ruina
EorI=1; % Theta update 1: explicit, 2: implicit
a=0.003;
b=0.006;
Dc=10e-6; % [m]
Vl=1e-3; % Loading Rate [m/s]
Vini=1e-6; % Initial Velocity [m/s]
ThetaI=Dc/Vini; % Initial State - set Start from steady state
NormalStress=2e6; % 2Mpa
V0=1e-9; % Reference velocity [m/s]
Friction0=0.6; % reference friction
FrictionI=Friction0+a*log(Vini/V0)+b*log(ThetaI*V0/Dc); % Initial friction
Mass=1000; % per unit area [kg/m^2] (10kg on 0.1 m by 0.1 m]
Kc_QS=(b-a)*NormalStress/Dc; % Critical Stiffness
Kc_Dyn=Kc_QS*(1+Mass*Vl^2/NormalStress/a/Dc);
K=0.8*Kc_Dyn; % Set stiffness 0.8 of critical stiffness
Xl=FrictionI*NormalStress/K; % initial load point

% Time Step Control
Dt=1e-5; % Time step [second]
TotalTime=2; % Total time [second]
TotalStep=round(TotalTime/Dt); % Total steps

% Convergence control
V_eps=1e-7 % Convergence criterion in NR
% DV=1e-15   % Denominator of NR - this will be changed with tested Velocity
Theta_eps=1e-6; % Convergence criterion for Theta update (implicit only)
DelTheta=1e-5; % Denominator of NR for Theta update (implicit only)


% Simulation begins
XlOld=Xl
Omega=sqrt(K/Mass);
Step=0;
for i=1:TotalStep

    Xl=XlOld+Dt*Vl; % Load point displacement
    if i==1
        Friction=FrictionI;
        DispOld=0;
        Disp=0;
        Theta=ThetaI;
        ThetaOld=Theta;
        VOld=Vini;
    end

    % Newton Rhapson Begins
    VDiff=10; % Arbitrary for initiation
    Iteration=0; % Number of iteration
    BREAK=0; % This only used when convergence is hard to made
    V=1e-11; % Arbitrary initial velocity (good to be small to pick up small V)
    while abs(VDiff-1)>V_eps
        Iteration=Iteration+1;
        VTest=V; % Velocity tested in this NR iteration
        DV=V/1e5; % Denominator of NR - changes with tested velocity

        % Finding Initial Value
        VOldIter=V;
        if DorR==1; % Deterich law
```

```
    if EorI==1; % explicit theta update
        Theta=ThetaOld+(1-V*ThetaOld/Dc)*Dt; % Equation (13) Deterich Evolution
    else % implicit theta update
        Theta=(ThetaOld+Dt)/(1+V*Dt/Dc); % Deterich Evolution explicit
    end
else % Ruina law
    if EorI==1;  % explicit theta update
        if V==0; Theta=ThetaOld; % when convergence is difficult to made
        else Theta=ThetaOld-V*ThetaOld/Dc*log(V*ThetaOld/Dc)*Dt; % Equation (14)
        end
    else  % implicit theta update
        if V==0; Theta=ThetaOld; % when convergence is difficult to made
        else
            Thetadiff=0;
            Theta=ThetaOld;
            while abs(Thetadiff-1)>Theta_eps
                ThetaTest=Theta;
                FT=Theta-ThetaOld+V*Theta/Dc*log(V*Theta/Dc)*Dt;
                Theta=Theta+DelTheta;
                FT_Dev=Theta-ThetaOld+V*Theta/Dc*log(V*Theta/Dc)*Dt;
                Theta=ThetaTest-FT*DelTheta/(FT_Dev-FT);
                Thetadiff=ThetaTest/Theta;
            end
        end

    end
end
Friction=Friction0+b*log(V0*Theta/Dc)+a*log(V/V0); % Equation (15)
F=Xl-Friction*NormalStress/K;
Disp=(DispOld-F)*cos(Omega*Dt)+(VOld/Omega)*sin(Omega*Dt)+F; % Equation (9)
V=(Disp-DispOld)/Dt*2-VOld; % Equation (12)

FOriginal=VOldIter-V; % testing this Function. Send this to zero

if V<0; BREAK=1 % Only used when convergence is failed
    break; end

% Finding deviated value for NR
V=VOldIter+DV;
VOldIter=V;
if DorR==1;  % Deterich law
    if EorI==1; % explicit theta update
        Theta=ThetaOld+(1-V*ThetaOld/Dc)*Dt; % Equation (13) Deterich Evolution
    else % implicit theta update
        Theta=(ThetaOld+Dt)/(1+V*Dt/Dc); % explicit Deterich Evolution
    end
else  % Ruina law
    if EorI==1; % explicit theta update
        if V==0; Theta=ThetaOld; % when convergence is difficult to made
        else Theta=ThetaOld-V*ThetaOld/Dc*log(V*ThetaOld/Dc)*Dt; % Equation (14)
        end
    else  % implicit theta update
        if V==0; Theta=ThetaOld; % when convergence is difficult to made
        else
            Thetadiff=0;
            Theta=ThetaOld;
            while abs(Thetadiff-1)>Theta_eps
                ThetaTest=Theta;
                FT=Theta-ThetaOld+V*Theta/Dc*log(V*Theta/Dc)*Dt;
                Theta=Theta+DelTheta;
                FT_Dev=Theta-ThetaOld+V*Theta/Dc*log(V*Theta/Dc)*Dt;
                Theta=ThetaTest-FT*DelTheta/(FT_Dev-FT);
                Thetadiff=ThetaTest/Theta;
            end
        end

    end
end
Friction=Friction0+b*log(V0*Theta/Dc)+a*log(V/V0); % Equation (15)
F=Friction*NormalStress/K;
Disp=(DispOld-Xl+F)*cos(Omega*Dt)+(VOld/Omega)*sin(Omega*Dt)+Xl-F; % Equation (9)
```

```
        V=(Disp-DispOld)/Dt*2-VOld; % Equation (12)

        NRF=VOldIter-V; % Recalculate NR testing function with this velocity

        DF=(NRF-FOriginal)/DV; % tangent of the NR function
        V=VTest-FOriginal/DF; % Update velocity

        if V<0; BREAK=1 % Only used when convergence is failed
            break; end

        VDiff=abs(VTest/V); % Calculate the Convergence criterion
        if Iteration>100; V_eps=V_eps*2 % Just in case it is too hard to be converged
        end
    end % End of NR iteration


    if BREAK==1  % only if we could not get convergence
        V=0; % set it just zero
        if DorR==1; Theta=ThetaOld+Dt; else Theta=ThetaOld; end
        % dTheta=1 for Detrich and dTheta=0 for Ruina
        Disp=DispOld;
    end


    if rem(i,5)==0 % save the data in every 5 steps
        T=i*Dt
        Step=Step+1;
        BreakHisotry(Step)=BREAK; % Did it not converged?
        VHistory(Step)=V; % velocity
        Accel(Step)=(V-VOld)/Dt; % acceleration
        APPFrictionHistory(Step)=((Xl-Disp)*K/NormalStress); % Apparent friction
        if VHistory(Step)==0; RASFricHistory(Step)=NaN;
           else
           RASFricHistory(Step)=Friction;
        end % Rate and State Friction
        DispHistory(Step)=Disp; % Displacement
        ThetaHistory(Step)=Theta; % State variable
        Time(Step)=i*Dt; % Time
        XlHistory(Step)=Xl; % Load Point
        VepsilonHistory(Step)=V_eps; % was it difficult to converge?
    end

    DispOld=Disp;
    ThetaOld=Theta;
    VOld=V;
    XlOld=Xl;
end


% Plots
figure(1)
hold on
set(gcf, 'color', 'w')
set(gca,'fontsize', 13)
ylabel('Friction coefficient')
xlabel('Time (s)')
plot(Time,APPFrictionHistory)
plot(Time,RASFricHistory,'r')
box on

figure(2)
hold on
ylabel('Friction coefficient')
xlabel('Velocity (m/s)')
set(gcf, 'color', 'w')
set(gca,'fontsize', 13)
plot(VHistory,RASFricHistory,'r')
plot(VHistory,APPFrictionHistory,'b')
set(gca,'Xscale', 'log')
box on
```

Acknowledgement

Data from numerical modeling are generated by the code available in the supporting information with all laboratory data available on request from the data repository hosted by Chris Marone at the Pennsylvania State University. This work is a partial result of support under projects DE-EE0006761 and DE-FE0023354. This support is gratefully acknowledged.

References

Bar-sinai, Y., Spatschek, R., Brener, E.A., and Bouchbinder, E., 2014, On the velocity-strengthening behavior of dry friction: J. Geophys. Res. Solid Earth., v. 119, p. 1738–1748, doi: 10.1002/2013JB010586.

Baumberger, T., and Caroli, C., 2006, Solid friction from stick-slip down to pinning and aging: adv. phys., v. 55, p. 279–348, doi: 10.1080/00018730600732186.

Bayart, E., A. M. Rubin, and C. Marone (2006), Evolution of fault friction following large velocity jumps, Eos Trans. AGU, 87(52), Fall Meet. Suppl., Abstract S31A–0180.

Beeler, N.M., Tullis, T.E., and Weeks, J.D., 1994, The roles of time and displacement in the evolution effect in rock friction: Geophys. Res. Lett., v. 21, p. 1987–1990.

Beeler, N.M., Hickman, S.H., and Wong, T., 2001, Earthquake stress drop and laboratory-inferred interseismic strength recovery: J. Geophys. Res, v. 106.

Beeler, N.M., Tullis, T., Jenni Junger, Kilgore, B., and Goldsby, D., 2014, Laboratory constraints on models of earthquake recurrence: J. Geophys. Res. Solid Earth, v. 119, p. 8770–8791, doi: 10.1002/2014JB011184.

Ben-david, O., Rubinstein, S.M., and Fineberg, J., 2010, Slip-stick and the evolution of frictional strength: Nature, v. 463, p. 76–79, doi: 10.1038/nature08676.

Bhattacharya, P., Rubin, A.M., Bayart, E., Savage, H.M., and Marone, C., 2015, Critical evaluation of state evolution laws in rate and state friction : Fitting large velocity steps in simulated fault gouge with time- , slip- , and stress-dependent constitutive laws: J. Geophys. Res. Solid Earth, p. 6365–6385, doi: 10.1002/2015JB012437.

Bhattacharya, P., Rubin, A.M., and Beeler, N.M., 2017, Does fault strengthening in laboratory rock friction experiments really depend primarily upon time and not slip ? J. Geophys. Res. Solid Earth, v. 122, p. 6389–6430, doi: 10.1002/2017JB013936.

Blanpied, M.L., Marone, C.J., Lockner, D.A., Byerlee, J.D., and King, D.P., 1998, Quantitative measure of the variation in fault rheology due to fluid-rock interactions: J. Geophys. Res., v. 103, p. 9691–9712.

Brace, W.F., and Byerlee, J.D., 1966, Stick-slip as a mechanism for earthquakes: Science, v. 153, p. 990–992.

Brechet, Y., and Estrin, Y., 1994, The effect of strain rate sensitivity on dynamic friction of metals: Scripta Metallurgica et Materialia, v. 30, p. 1449–1454.

Carpenter, B.M., Scuderi, M.M., Collettini, C., and Marone, C., 2014, Frictional heterogeneities on carbonate-bearing normal faults: Insights from the Monte Maggio Fault, Italy: J. Geophys. Res. Solid Earth, v. 119, doi: 10.1002/2014JB011337.

Carpenter, B.M., Ikari, M.J., and Marone, C., 2016, Laboratory observations of time-dependent frictional strengthening and stress relaxation in natural and synthetic fault gouges: J. Geophys. Res. Solid Earth, p. 1183–1201, doi: 10.1002/2015JB012136.

Chen, J., and Spiers, C., 2016, Rate and state frictional and healing behavior of carbonate fault gouge explained using microphysical model: J. Geophys. Res. Solid Earth, v. 121, p. 8642–8665, doi: 10.1002/2016JB013470.

Coulomb, C.A., 1785, Théorie des machines simples, en ayant égard au frotement de leurs parties, et a la roideur des cordages, *Mem. Math. Phys*., X, Paris, 161-342.

Dieterich, J.I., 1972, Time-dependent friction in rocks: J. Geophys. Res., v. 77, p. 3690–3697.

Dieterich, J., and Kilgore, B., 1994, Direct observation of frictional contacts: new insights for state-dependent properties: Pageoph, v. 143.

Estrin, Y., and Brechet, Y., 1996, On a model of frictional sliding: Pageoph., v. 147.

Frye, K.M., and Marone, C., 2002, Effect of humidity on granular friction at room temperature: J. Geophys. Res., v. 107, p. 1–13, doi: 10.1029/2001JB000654.

Giger, S.B., Cox, S.F., and Tenthorey, E., 2008, Slip localization and fault weakening as a consequence of fault gouge strengthening — Insights from laboratory experiments: Earth Planet. Sci. Lett., v. 276, p. 73–84, doi: 10.1016/j.epsl.2008.09.004.

Gu, J.-C., Rice, J.R., Runia, A., and Tse, S., 1984, Slip motion and stability of a single degree of freedom elastic system with rate and state dependent friction: Journal of the Mechanics and Physics of Solids, v. 32, p. 167–196, doi: 10.1016/S0022-5096(98)00113-6.

Gu, Y., and Wong, T., 1991, Effects of loading velocity, stiffness, and inertia on the dynamics of a single degree of freedom spring-slider system: J. Geophys. Res., v. 96.

He, C., Wong, T., and Beeler, N.M., 2003, Scaling of stress drop with recurrence interval and loading velocity for laboratory-derived fault strength relations: J. Geophys. Res., v. 108, p. 1–13, doi: 10.1029/2002JB001890.

Ikari, M.J., Marone, C., and Saffer, D.M., 2011, On the relation between fault strength and frictional stability: Geology, v. 39, p. 83–86, doi: 10.1130/G31416.1.

Ikari, M.J., Carpenter, B.M., and Marone, C., 2016a, A mocrophysical interpretation of rate- and state-dependent friction for fault gouge: Geochem. Geophys. Geosyst., v. 17, p. 1660–1677, doi: 10.1002/2016GC006286.

Ikari, M.J., Carpenter, B.M., Vogt, C., and Kopf, A.J., 2016b, Elevated time-dependent strengthening rates observed in San Andreas Fault drilling samples: Earth Planet. Sci. Lett., v. 450, p. 164–172, doi: 10.1016/j.epsl.2016.06.036.Johnson, T.L., and Scholz, C.H., 1976, Dynamic Properties of Stick-Slip Friction of Rock: J. Geophys. Res., v. 81, p. 881–888.

Karner, S.L., Marone, C., and Evans, B., 1997, Laboratory study of fault healing and lithification in simulated fault gouge under hydrothermal conditions: Tectonophysics, v. 277, p. 41–55.

Karner, S., and Marone, C., 2000, Effects of loading rate and normal stress on stress drop and stick slip recurrence interval: Geocomplexity and the Physics of Earthquakes,, Geophys Monogr. Ser., vol. 120, edited by J. B. Rundle et al., pp. 187-198, AGU, Washington D. C.

Karner, S.L., and Marone, C., 2001, Karner_Frictional restrengthening in simulated fault gouge: Effect of shear load perturbations: J. Geophys. Res., v. 106, p. 19319–19337.

Lapusta, N., and Liu, Y., 2009, Three-dimensional boundary integral modeling of spontaneous earthquake sequences and aseismic slip: J. Geophys. Res., v. 114, p. 1–25, doi: 10.1029/2008JB005934.

Lapusta, N., Rice, R., Ben-Zion, Y., and Zheng, G., 2000, Elastodynamic analysis for slow tectonic loading with spontaneous rupture episodes on faults with rate- and state-dependent friction: J. Geophys. Res., v. 105.

Leeman, J.R., Saffer, D.M., Scuderi, M.M., and Marone, C., 2016, Laboratory observations of slow earthquakes and the spectrum of tectonic fault slip modes: Nature Communications, v. 7, p. 1–6, doi: 10.1038/ncomms11104.

Leeman, J.R., Scuderi, M.M., Marone, C., Saffer, D.M., and Shinbrot, T., 2014, On the origin and evolution of electrical signals during frictional stick slip in sheared granular material: J. Geophys. Res.: Solid Earth, doi: 10.1002/2013JB010793.

Li, Q., Tullis, T.E., Goldsby, D., and Carpick, R.W., 2011, Frictional ageing from interfacial bonding and the origins of rate and state friction: Nature, v. 480, p. 233–236, doi: 10.1038/nature10589.

Linker, M.F., and Dieterich, J.H., 1992, Effects of variable normal stress on rock friction: Observations and constitutive equations: J. Geophys. Res., v. 97, p. 4923–4940.

Marone, C., 1998a, Laboratory-Derived Friction Laws and Their Application to Seismic Faulting: Annual Review of Earth and Planetary Sciences, v. 26, p. 643–696, doi: 10.1146/annurev.earth.26.1.643.

Marone, C., 1998b, The effect of loading rate on static friction and the rate of fault healing during the earthquake cycle: Nature, p. 69–72, doi: 10.1038/34157.

Marone, C., Cocco, M., Richardson, E., and Tinti, E., 2009, The critical slip distance for seismic and aseismic fault zones of finite width: Fault-Zone Properties and Earthquake Rupture Dynamics Chapter 6, Academic Press, 135-162 p.

Marone, C., and Saffer, D.M., 2015, The Mechanics of frictional healing and slip instability during the seismic cycle: Treatise on Geophysics Elsevier B.V., 111-138 p.

Marone, C., Vidale, J., and Ellsworth, W., 1995, Fault healing inferred from time dependent variations in source properties of repeating earthquakes: Geophys. Res. Lett., p. 3095–3098.

Mclaskey, G.C., Thomas, A.M., Glaser, S.D., and Nadeau, R.M., 2012, Fault healing promotes high-frequency earthquakes in laboratory experiments and on natural faults: Nature, v. 490, p. 101–104, doi: 10.1038/nature11512.

Nadeau, R.M., and Johnson, L., 1998, Seismological Studies at Parkfield VI : Moment Release Rates and Estimates of Source Parameters for Small Repeating Earthquakes: Bulletin of Seismological Society of America, v. 88, p. 790–814.

Nakatani, M., and Scholz, C.H., 2004, Frictional healing of quartz gouge under hydrothermal conditions : 1 . Experimental evidence for solution transfer healing mechanism: J. Geophys. Res., v. 109, doi: 10.1029/2001JB001522.

Nakatani, M., and Scholz, C.H., 2006, Intrinsic and apparent short-time limits for fault healing : Theory , observations , and implications for velocity-dependent friction: J. Geophys. Res., v. 111, p. 1–19, doi: 10.1029/2005JB004096.

Niemeijer, A., Marone, C., and Elsworth, D., 2008, Healing of simulated fault gouges aided by pressure solution : Results from rock analogue experiments: J. Geophys. Res., v. 113, p. 1–15, doi: 10.1029/2007JB005376.

Niemeijer, A.R., Boulton, C., Toy, V.G., Townend, J., and Sutherland, R., 2016, Large-displacement, hydrothermal frictional properties of DFDP-1 fault rocks, Alpine Fault, New Zealand: Implications for deep rupture propagation: J. Geophys. Res. Solid Earth, p. 624–647, doi: 10.1002/2015JB012593.

Perfettini, H., and Molinari, A., 2017, A micromechanical model of rate and state friction: 1. Static and dynamic sliding: J. Geophys. Res., v. 122, p. 2590–2637, doi: 10.1002/2016JB013302.

Rabinowicz, E. (1951), The nature of static and kinetic coefficients of friction, J. Appl. Phys., 22, 1373–1379.

Rabinowicz, E. (1956), Stick and Slip, Sci. Am., 194(5), 109–119, doi:10.1038/scientificamerican0556-109.

Rathbun, A.P., and Marone, C., 2013, Symmetry and the critical slip distance in rate and state friction laws: J. Geophys. Res., v. 118, p. 1–14, doi: 10.1002/jgrb.50224.

Rice, J.R., 1993, Spatio-temporal Complexity of Slip on a Fault Rate- dependent friction: J. Geophys. Res., v. 98, p. 9885–9907.

Rice, J.R., and Ruina, A.L., 1983, Stability of Steady Frictional Slipping: J. Appl. Mech., v. 50, p. 343–349

Rice, J.R., and Tse, S.T., 1986, Dynamic Motion of a Single Degree of Freedom System Following a Rate and State Dependent Friction Law: J. Geophys. Res., v. 91, p. 521–530.

Rice, J.R., Lapusta, N., and Ranjith, K., 2001, Rate and state dependent friction and the stability of sliding between elastically deformable solids: J. Mech. Phys. Solids., v. 49, p. 1865–1898.

Roy, M., and Marone, C., 1996, Earthquake nucleation on model faults with rate and state friction: Effects of inertia: J. Geophys. Res., v. 101, p. 13919–13932.

Rubinstein, J.L., Ellsworth, W.L., Chen, K.H., and Uchida, N., 2012, Fixed recurrence and slip models better predict earthquake behavior than the time- and slip-predictable models: 1. Repeating earthquakes: J. Geophys. Res., v. 117, p. 1–23, doi: 10.1029/2011JB008724.

Ruina, A., 1983, Slip instability and state variable friction law: J. Geophys. Res., v. 88, p. 10359–10370, doi: 10.1029/JB088iB12p10359.

Scholz, C.H., 1982, Scaling laws for large earthquakes: consequences for physical models: Bull. Seism. Soc. Am, v. 72, p. 1–14.

Scholz, C.H., 1998, Earthquakes and friction laws: Nature, v. 391, p. 37–42, doi: 10.1038/34097.

Scholz, C.H., Aviles, A., and Wesnousky, S.G., 1986, Scaling differences between large interplate and intraplate earthquakes: Bill. Seismol. Soc. Am., v. 76, p. 65–70.

Scholz, C.H., and Engelder, J.T., 1976, The role of asperity indentation and ploughing in rock friction - I: int. J. Rock Mech. Min. Sci & Geomech., v. 13, p. 149–154.

Schwartz, D.P., and Coppersmith, K.J., 1984, Fault behavior and characteristic earthquakes: Examples from the Wasatch and San Andreas Fault Zones: J. Geophys. Res., v. 89, p. 5681–5698.

Scuderi, M.M., Marone, C., Tinti, E., Stefano, G. Di, and Collettini, C., 2016, Precursory changes in seismic velocity for the spectrum of earthquake failure modes: Nature Geoscience, v. 9, p. 695–700, doi: 10.1038/NGEO2775.

Scuderi, M.M., Carpenter, B.M., Johnson, P.A., and Marone, C., 2015, Poro mechanics of stick-slip frictional sliding and strength recovery on tectonic faults: J. Geophys. Res., p. 6895–6912, doi: 10.1002/2015JB011983.Received.

Scuderi, M.M., Carpenter, B.M., and Marone, C., 2014, Physicochemical processes of frictional healing: Effects of water on stick-slip stress drop and friction of granular fault gouge: J. Geophys. Res. Solid Earth, doi: 10.1002/2013JB010641.Received.

Sleep, N.H., 2006, Real contacts and evolution laws for rate and state friction: Geochem. Geophys. Geosyst., v. 7, p. 1–17, doi: 10.1029/2005GC001187.

Svetlizky, I., Bayart, E., Cohen, G., and Fineberg, J., 2017, Frictional Resistance within the Wake of Frictional Rupture Fronts: Phys. Rev. Lett., v. 118, p. 1–5, doi: 10.1103/PhysRevLett.118.234301.

Tenthorey, E., and Cox, S.F., 2006, Cohesive strengthening of fault zones during the interseismic period : An experimental study: J. Geophys. Res., v. 111, doi: 10.1029/2005JB004122.

Tse, S.T., and Rice, J.R., 1986, Crustal Earthquake Instability in Relation to the Depth Variation of Frictional Slip Properties: J. Geophys. Res., v. 91, p. 9452–9472.

Vidale, J.E., Ellsworth, W.L., Cole, A., and Marone, C., 1994, Variations in rupture process with recurrence interval in a repeated small earthquake: Nature, v. 368, p. 624–626.

Yasuhara, H., Marone, C., and Elsworth, D., 2005, Fault zone restrengthening and frictional healing : The role of pressure solution: J. Geophys. Res., v. 110, p. 1–11, doi: 10.1029/2004JB003327.

Chapter 2

The Transition from Steady Frictional Sliding to Inertia-Dominated Instability with Rate and State Friction

Abstract

Unstable frictional slip motions are investigated with a rate and state friction law across the transition from quasi-static (slowly loaded) slip to dynamic slip, dominated by inertia. Using a novel numerical method, we conduct simulations to investigate the roles of inertial and quasistatic factors of the critical stiffness defining the transition to instability, K_c. Our simulations confirm theoretical estimates of K_c, which is dependent on mass and velocity. Furthermore, we show that unstable slip motion has two distinct dynamic regimes with characteristic limit cycles: (i) stick-slip motions in the quasi-static (slowly loaded) regime and (ii) quasi-harmonic oscillations in the dynamic (fast loaded) regime. Simulation results show that the regimes are divided by the frictional instability coefficient, $\eta = MV^2/\sigma a D_c$ and stiffness of the system K. The quasi-static regime is governed by the ratio K/K_c and both the period and magnitude of stick-slip cycles decrease with increasing loading rate. In the dynamic regime, slip occurs in harmonic limit cycles, the frequency of which increases with loading velocity to a limit set by the natural frequency of the system. Our results illuminate the origin of the broad spectrum of slip behaviors observed for systems ranging from manufacturing equipment to automobiles and tectonic faults, with particular focus on the role of elasto-frictional coupling in dictating the transition from slow slip to dynamic instability. We highlight distinct characteristics of friction-induced slip motions (stick-slip and friction-induced vibration) and show that the dynamic frictional

instability coefficient (*η*) is a key parameter that both defines the potential for instability and determines the dynamic characteristics of instability.

1. Introduction

Friction plays a key role in the mechanical behavior of systems that involve slipping contacts. In many situations, the transition from stable to unstable slip motion is of primary interest. When such systems are loaded slowly, frictional motion often occurs as repeated episodes of quasi-stationary contact followed by rapid slip, which defines the classical 'stick-slip' instability [Bridgman, 1936, 1951; Rabinowicz, 1951, 1956; Singh, 1960; Shimamoto et al., 1980; Baumberger et al., 1994]. When loading is more rapid, frictional motion often occurs as a high frequency quasi-harmonic oscillation [Brockley and Ko, 1970], which is referred to as friction-induced vibration. The stick-slip instability has been analyzed intensely in earthquake science as it is directly analogous to natural earthquakes [Brace and Byerlee, 1966] as well as in slowly loaded mechanical systems [Kammer et al., 2014, 2015; Svetlizky et al., 2017]. Friction induced vibration has also received much attention, because of its importance in engineering systems where it causes surface wear, damage and noise [Ibrahim, 1994]. However, the transition from stick-slip to frictional vibration has received less attention, despite its importance in engineered and natural systems.

The conditions for the stability transition from stable to unstable sliding with rate and state friction are presented by Rice and Ruina [1983]. They showed that stable sliding at a certain velocity can only be achieved when system stiffness is larger than a critical value K_c. The parameter K_c represents a critical rate of frictional weakening with slip.

Notably, K_c depends not only on friction parameters, but also on dynamic variables, *i.e.*, mass and velocity [Ruina, 1983; Rice and Ruina, 1983; Gu et al., 1984; Rice, 1993; Baumberger and Caroli, 2006; Ranjith and Rice, 1999; Rice et al., 2001; Perfettini and Molinari, 2017]. This analysis shows that a system can become significantly unstable with increased mass and slip velocity, indicating that dynamic (inertial) factors are key parameters controlling slip stability in the high velocity slip regime.

Modern constitutive laws for sliding recognize the importance of frictional slip rate and past states of the sliding surfaces. These effects form the basis for the rate and state friction constitutive laws [Dieterich, 1979a,b; Runia, 1983; Rice and Ruina, 1983], which have been applied to a wide range of systems ranging from tectonic faults [Scholz, 2002; Luo and Ampuero, 2017; van den Ende et al., 2017] to nanoscale, atomic contacts [e.g., Tian et al., 2017]. Rate and state friction (RSF) laws successfully capture laboratory observations of macroscopic friction for a range of loading rates [Marone, 1998a; Baumberger and Caroli, 2006]. The laws were originally developed to describe frictional behavior in rock [Dieterich, 1979a; Ruina, 1983], but later it was shown that they are applicable to wide variety of materials [Dieterich and Kilgore 1994, Heslot et al., 1994; Baumberger and Caroli, 2006].

For frictional systems that are loaded slowly, both analytic and laboratory observations of stick-slip magnitude show a strong inverse relationship with the logarithm of loading rate (*i.e.* magnitude decreases with increased velocity) [Gu and Wong 1991; Karner and Marone, 2000; Mair et al., 2002; Beeler et al, 2001, 2014; Scuderi et al., 2015]. One may expect that the magnitude of stick-slip will decrease continuously with increased velocity. However, this expectation is at odds with the stability analysis of Rice and Ruina

[1983], which predicts that slip will become unstable at high slip velocity. One may assume a smooth transition from the quasi-static (low velocity) regime to the dynamic (high velocity) regime. However, the dynamic regime for systems exhibiting rate and state friction has received relatively little attention [c.f., Rice, 1993], with few works focused on complete solutions that account for the transition from stable sliding to fully dynamic motion with inertia.

Here, we use a novel numerical solution to address the full spectrum of slip modes for a system with rate and state friction and 1D elastic coupling [Im et al., 2017]. We focus on numerical observations of dynamic friction behavior throughout the transition from quasi-static to dynamic motion. We investigate frictional behaviors of (i) the stable to unstable transition induced by dynamic effects and (ii) dynamic characteristics of frictional slip throughout the transition from quasi-static (slow loading) to dynamic loading.

2. Background Summary

2.1. Rate and state friction law

In the framework of RSF, frictional resistance is dependent on slip velocity V and the history of sliding, which is characterized in terms of a state variable θ [Dieterich, 1979; Ruina, 1983]. The most widely used form is:

$$\mu = \mu_0 + a\ln\left(\frac{V}{V_0}\right) + b\ln\left(\frac{V_0\theta}{D_c}\right) \tag{1}$$

where μ_0 is a reference friction coefficient that corresponds to steady state friction at reference slip velocity V_0, D_c is a critical slip distance that characterizes the evolution of friction following a perturbation, and the non-dimensional parameters a and b represent the magnitude of the direct change in friction following a change in slip velocity and the subsequent evolution of friction.

The evolution of friction following a perturbation imposed during steady sliding is modulated by time via contact aging processes and slip. Although a multitude of processes may affect friction evolution, two evolution laws have received the most attention [Marone, 1998a]. The Dieterich (or aging) law focuses on the evolution of state with time:

$$\frac{d\theta}{dt} = 1 - \frac{V\theta}{D_c} \tag{2}$$

whereas the Ruina (or slip law) characterizes friction evolution strictly in terms of the sliding distance. For the Ruina law, the rate of state evolution vanishes as velocity goes to zero:

$$\frac{d\theta}{dt} = -\frac{V\theta}{D_c}\ln\left(\frac{V\theta}{D_c}\right). \tag{3}$$

The two evolution laws behave similarly for small perturbations around steady state ($\theta \sim D_c/V$) but they diverge substantially when velocity is far from steady state [Ampuero and Rubin, 2008; Bhattacharya et al., 2015, 2017].

2.2. Elastic coupling

In a frictional system with one dimensional elastic interaction, the force balance governing motion is

$$\frac{M\ddot{\delta}}{\sigma} = \frac{K(\delta_{lp} - \delta)}{\sigma} - \mu \tag{4}$$

where M is mass per unit area (kg/m^2), K is a stiffness expressed in units of shear stress (Pa/m), and σ is normal stress (see Figure 2-1 inset). Note that the force balance is divided by contact area and normal stress in Equation 4, which shows that normalized shear stress (first term on the RHS) and friction (μ) decouple when the inertial term (LHS) is significant. For a system where the mechanical response is stiff ($\delta \approx \delta_{\mathrm{lp}}$) and motion is quasi-static ($\mathrm{M} \approx 0$), the RSF response to an e-fold increase in slip velocity can be illustrated according to Equations 1-3. For a sudden jump in velocity by a factor of e, friction increases immediately by a magnitude corresponding to a (direct effect) and then decays by a magnitude corresponding to b (evolution effect) over an e-folding slip distance given by D_c (Figure 2-1). After sufficient slip, friction reaches a new steady state. The difference in steady state friction between the original slip rate V_o and the new slip rate V is given by $(a\text{-}b)\ \ln(V/V_o)$.

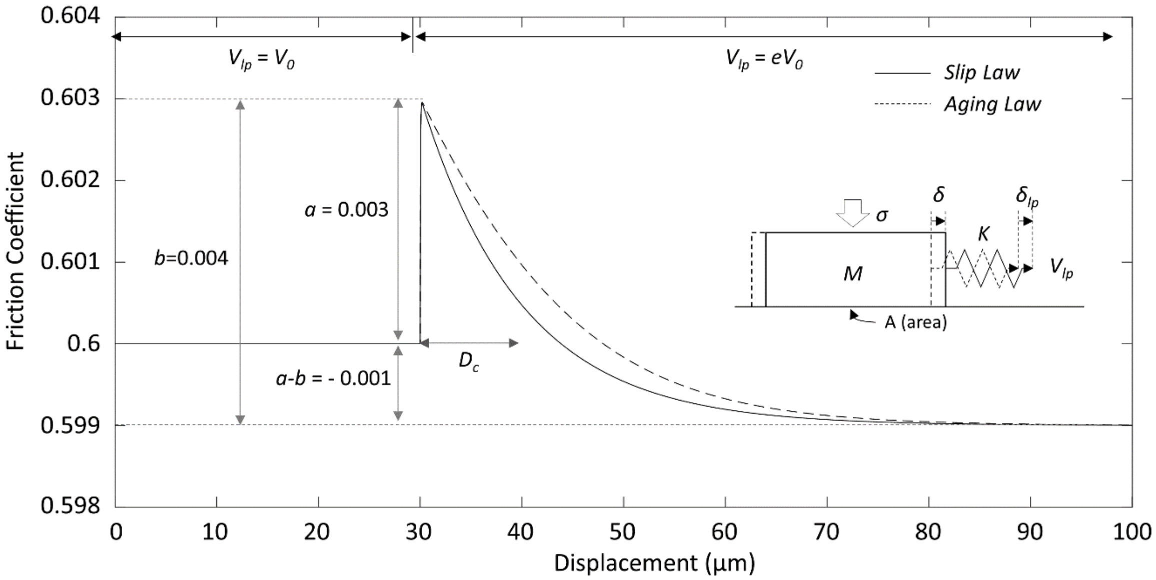

Figure 2-1 Friction response to an *e*-fold velocity step for a stiff ($\delta \approx \delta_{lp}$) spring-slider system undergoing quasi-static ($M = 0$) motion. Results are shown for both the Ruina (slip) and Dieterich (aging) state evolution laws. RSF parameters are: $a = 0.003$, $b = 0.004$, $D_c = 10$ µm, $V_0 = 30$ µm/s and normalized stiffness $K/\sigma = 1\times10^5$/m. Inset shows spring-slider system. Gravitational force is included in σ.

2.3. Critical stiffness and stability criterion

Figure 2-1 implies that unstable sliding may occur when $(a - b) < 0$, because frictional resistance decreases with increased velocity and this may induce self-driven acceleration. Several studies have shown that this condition is indeed necessary for unstable slip but not sufficient [Runia, 1983; Rice and Ruina, 1983; Rice, 1993; Ranjith and Rice, 1999]. Steady sliding at velocity V occurs when the elastic stiffness K is larger than the critical stiffness K_c:

$$K_c = -\frac{V d\tau_{ss}(V)/dV}{D_c}\left[1 + \frac{MV}{D_c \partial\tau(V,\theta)/\partial V}\right] \tag{5}$$

where τ is shear stress and $\tau_{ss}(V)$ is the steady state shear stress at velocity V [Rice and Ruina, 1983]. Equation 5 is general and not strongly restricted to RSF. For a one state variable RSF law, Equation (5) can be further simplified to [Gu et al., 1984; Roy and Marone, 1996; Baumberger and Caroli, 2006],

$$K_c = \frac{(b-a)\sigma}{D_c}\left[1+\frac{MV^2}{\sigma a D_c}\right]. \tag{6}$$

For quasi-static motion, Equation (6) can be simplified by substituting $M = 0$, *i.e.* $K_{c,qs} = (b\text{-}a)\sigma/D_c$ [Ruina, 1983]. These relations show that velocity weakening, $(a - b) < 0$, is required for frictional instability, because if K_c is negative, only stable sliding is possible given that K is positive. The value of K_c dictates the potential for frictional instability for a sliding system. As K_c increases, higher system stiffness is required for stable sliding.

The second bracketed term in Equation (6) is a dimensionless number representing a “dynamic” effect. Given its importance for slip stability and the transition from stick-slip to frictional vibration, we define the dynamic frictional instability coefficient η

$$\eta = \frac{MV^2}{\sigma a D_c}. \tag{7}$$

The parameter η represents the dynamic contribution to frictional instability and can be compared to the purely quasi-static factor. Equation 6 shows that mass M and velocity V play a key role in frictional motion. The dynamic effect on K_c can be negligible at slow velocity ($V^2 << \sigma a D_c/M$), but it can be significant when mass and velocity are high and $\eta \geq 1$, which represents the value at which the dynamic effect exceeds the quasi-static effect on K_c. Note that η can increase without limit and is strongly sensitive to slip velocity

($\eta \sim V^2$), indicating that any system with $a - b < 0$ has potential for unstable sliding at sufficiently large velocity.

3. Simulation Results

The simulations are conducted using a recent solution that provides increased numerical stability over the full range of deformational modes - from stable sliding to fully dynamic, unstable motion [Im et al., 2017]. In this method, RSF and velocity are solved for each numerical step as constrained within the solution imposed by force balance. The time-discretized equation for displacement is

$$\delta^{i+1} = [\delta^i - ({\delta_{lp}}^{i+1} - \mu^{i+1}\sigma / K)]\cos(\omega\Delta\,\mathrm{t}) + \frac{V^i}{\omega}\sin(\omega\Delta t) + ({\delta_{lp}}^{i+1} - \mu^{i+1}\sigma / K) \qquad (8)$$

where superscripts *i* and *i+1* denote successive time steps and ω is angular velocity defined as $\omega = \sqrt{K / M}$. Using the midpoint velocity, we define

$$V^{i+1} = 2\frac{(\delta^{i+1} - \delta^i)}{\Delta t} - V^i\ . \qquad (9)$$

Rate and state friction at each numerical step is calculated using V^{i+1} and simultaneously solved with equation (8) and (9) (see Im et al., [2017] for details).

We conducted two sets of numerical experiments. The first set is conducted for $K > K_{c,qs}$. According to Equation (6), this condition yields stable sliding at slowly slipping motion while it can become unstable at sufficiently fast velocity. Our second set of numerical experiments are conducted with $K < K_{c,qs}$, which always yields unstable slip motion regardless of the slip velocity. It is well known that this condition yields stick-slip instability when the system is loaded slowly [Rice and Tse, 1986; Im et. al., 2017]. Here, we go beyond the earlier work and study the full range from slow to fast loading velocity, spanning this transitional area with a single solution method, including cases where the dynamic effect becomes significant ($\eta > 1$).

3.1 Velocity stepping over stable/unstable boundary

For a constant elastic stiffness K, Equation 6 defines a critical velocity V_c as,

$$V_c = \sqrt{\frac{\sigma a D_c}{M}\left(\frac{K D_c}{(b-a)\sigma} - 1\right)} \tag{10}$$

The critical velocity represents a stability condition, such that for loading at subcritical rates ($V_{lp} < V_c$), friction will be eventually stabilized at the loading velocity. Conversely, if the system is loaded at supercritical velocities ($V_{lp} > V_c$), slip will be unstable.

We conducted numerical simulations of the frictional response to step changes in loading velocity using sub- and supercritical velocity steps (Figure 2-2). RSF parameters were fixed at $\mu_0 = 0.6$, $V_0 = 10^{-9}$ m/s, $D_c = 10$ µm, $a = 0.003$ and $b = 0.006$ which roughly typify polished granite surfaces or shear within granular layers used to simulate the wear and breccia (fault gouge) found in tectonic fault zones [Marone, 1998a]. We used $\sigma = 2$ MPa, $M = 3000$ kg/m^2 and an elastic stiffness K of $1.5K_{\mathrm{c,qs}}$ ($K = 900$ MPa/m; $K_{\mathrm{c,qs}} = 600$ MPa/m). For these parameters Equation (10) yields a critical velocity V_c of ~ 3.16 mm/s. Our simulations begin with stable sliding at an initial velocity $V = 0.1$ mm/s, which is well below V_c, and then step changes in loading velocity V_{lp} are imposed using three values (Figure 2-2) that correspond to: (i) strongly subcritical velocity (0.3 mm/s), (ii) slightly subcritical velocity (3.1 mm/s) and (iii) slightly supercritical velocity (3.2 mm/s). Figure 2-2b shows the dynamic critical stiffness (Equation (6)) for each case along with the elastic stiffness K. The stability transition is predicted to occur between V_{lp} = 3.1 and 3.2 mm/s, corresponding to V_c ~ 3.16 mm/s (Figure 2-2b).

The friction responses for the three cases studied (Figure 2-2a) clearly demonstrate that sliding stability is indeed determined by the "dynamic" critical stiffness, consistent with Equation (6). All three cases show initially unstable oscillations immediately following the velocity jump, but their subsequent behaviors are significantly different (Figure 2-2a). For the strongly subcritical case (black line; V_{lp} = 0.3 mm/s), the oscillation rapidly attenuates and sliding quickly becomes steady at the new loading velocity. For the two higher loading rate cases, the initial response involves a large stress drop and rapid acceleration. Slip velocity oscillates to a large magnitude and gradually decreases to steady sliding for the jump to 3.1 mm/s, whereas the jump to 3.2 mm/s produces sustained harmonic oscillations that range from ~ 2.6 to 4 mm/s (Figure 2-2a inset).

The convergence behaviors of the two near critical cases are compared in the phase plane diagram (Figure 2-2a) for an extended duration of 10 s after the velocity steps. Note that the two cases are initially similar but that their final behaviors are significantly different. The oscillation for the subcritical case (red line) converges to its theoretical steady state point (marked by the × in the inset to Figure 2-2a), while the supercritical case converges to a periodic limit cycle.

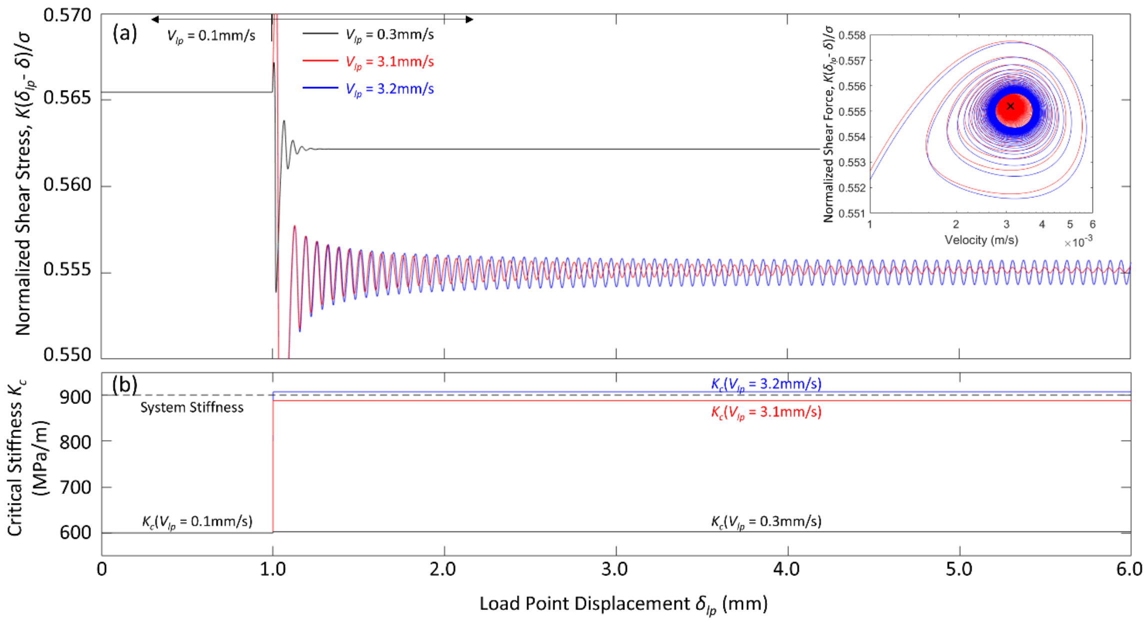

Figure 2-2 . (a): Friction response to three velocity steps: (i) strongly subcritical velocity (0.3mm/s; black), (ii) slightly subcritical velocity (3.1 mm/s; red) and (iii) slightly supercritical velocity (3.2 mm/s; blue). Simulations used the Ruina law with $\mu_0 = 0.6$, $V_0 = 10^{-9}$ m/s, $D_c = 10$ µm, $a = 0.003$, $b = 0.006$, $\sigma = 2$ MPa and $M = 3000$ kg/m^2 with stiffness K set to 1.5 of the quasi-state critical stiffness ($K = 900$ MPa/m; $K_{c,qs} = 600$ MPa). These input parameters yield a critical velocity of 3.16 mm/s. Note that the subcritical velocity step (red) converges to the predicted value of slip velocity (marked with an × on the phase diagram, inset to panel a) while the supercritical velocity case (blue) results in a limit cycle oscillation. (b) Calculated critical stiffness for each case (colors correspond to those of panel a) with system stiffness also shown (black dashed line). The identical simulation results for the Dieterich law are presented in the supplement.

We conducted multiple simulations to further examine the transition from stable to unstable motion (Figure 2-3). We used the same set of RSF parameters as above (Figure 2-2) while varying the mass and velocity. We tested 12 values of M and 13 velocities, for a total of 156 cases. Figure 2-3 shows results in terms of the magnitude of the normalized shear stress oscillation for the limit cycle (e.g., Figure 2-2a). The boundary between stable (empty circles) and unstable (filled circles) motion corresponds to the prediction of the Rice-Ruina dynamic stability criteria (red dashed line; Equation (10)).

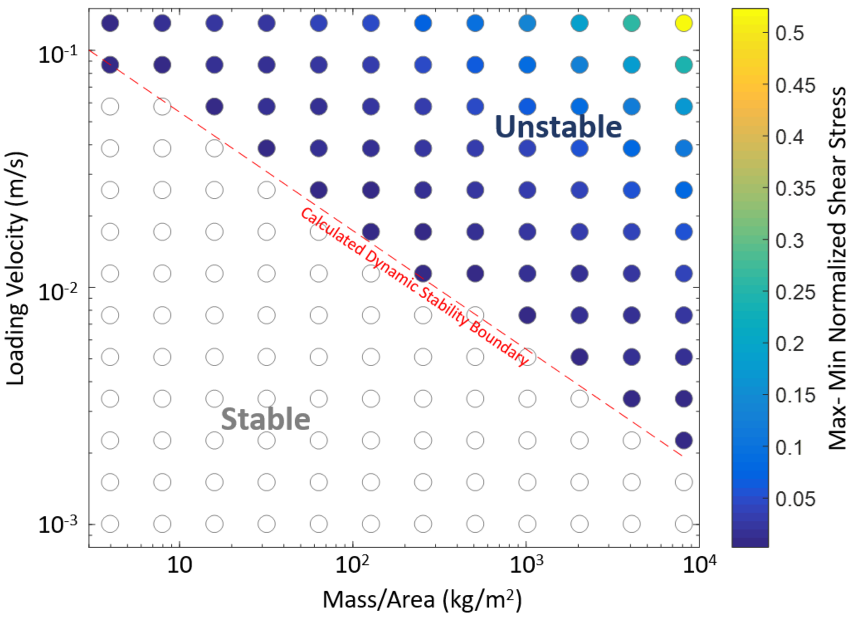

Figure 2-3 Magnitudes of the normalized shear stress oscillation at the limit cycle (10s after velocity step) for 12 values of M and 13 loading velocities V_{lp}. Input parameters are identical to simulations in Figure 2-2 except M and V_{lp}. Empty circles denotes stable frictional motion. Red dashed line shows that the Rice-Ruina dynamic stability criterion predicts our results.

3.2 Dynamic characteristics of instability

The periodic limit cycles demonstrated in Figure 2-2a are clearly not a stick-slip instability, but rather represent a harmonic oscillation. As stick-slip instabilities at slow loading rates are well documented with rate and state friction [Rice and Tse, 1986; Im et al., 2017], these observations show that the two different dynamical frictional regimes (stick-slip and harmonic vibration) can be integrated within a single framework of frictional response, provided inertia is correctly incorporated. The quasi-harmonic oscillations we observe (Figure 2-2) can be understood *via* the inertial term of the force balance ($M\ddot{\delta} = K(\delta_{lp} - \delta)$) and therefore should be related to the dynamic frictional instability coefficient, η.

We studied a suite of cases to illustrate how limit-cycles vary with loading velocity and dynamical parameters and summarize results using the magnitude of the limit cycle oscillation (Figure 2-4). The simulations of Figure 2-4 are conducted with the Ruina law (see supplement for Dieterich Law results) and $a = 0.005$, $b = 0.008$, $D_c = 10$ μm and $\sigma = 4$ MPa, which yields $K_{c,qs} = 1.2$ GPa/m. We used elastic stiffness $K = 0.96$ GPa/m (black) and $K = 0.60$ GPa/m (gray) that yield $K = 0.8\ K_{c,qs}$ and $K = 0.5\ K_{\mathrm{c,qs}}$ respectively. Thus, the systems always yield unstable motion regardless of mass or velocity (Figures 4 b and c). We varied loading velocity across five orders of magnitude using a constant value of mass per unit area $M = 100$ kg/m^2. All simulations converged to periodic limit cycles.

Our results define two distinct regimes, with stick-slip motion occurring for loading velocities below a critical value and harmonic oscillations occurring above (Figure 2-4). For slower loading rates, the oscillation magnitude decreases roughly log-linearly with V_{lp}, which is a well-documented behavior of stick-slip friction drop [Karner and Marone, 2000; Beeler et al., 2001&2014; Ben-David et al., 2012; He et al., 2003, Tian et al., 2017]. One way to understand this is to consider that peak friction increases with contact age, which scales inversely with stick-slip recurrence interval [Marone, 1998b]. Our results also show that the trend of decreasing stick slip magnitude with loading rate becomes nonlinear, with stick-slip stress drop reaching a minimum at loading velocities of ~3 ~ 5 cm/s, depending on stiffness K (Figure 2-4). With increased loading velocity, the magnitude of harmonic oscillations increases with loading rate, which defines the dynamic regime.

The transition from quasi-static stick slip to quasi harmonic oscillations can be described by the emergence of dynamic instability coefficient η. Figure 2-4a shows that the oscillation magnitude begins to deviate from the linear trend when the dynamic instability coefficient (blue line) starts to increase. In fact, it is expected that the decreasing trend of stress drop in the quasi-static regime does not extend to zero, because the elastic stiffness for stable sliding increases strongly as loading rate increases, due to the dynamic effects included in η. Note that η is negligible at low velocity ($V^2 << \sigma a D_c /M$), however once it reaches a value of ~ 1, it increases rapidly, as the square of velocity.

The dynamic characteristics of frictional instability show clear differences between the two regimes illustrated in Figure 2-4. In the quasi-static regime, the stick-slip limit cycle is apparent (Figure 2-4b). Conversely in the dynamic regime, friction exhibits a high frequency quasi-static oscillation (Figure 2-4c) similar to what we saw in Figure 2-2.

It is clear that inertia plays a key role in distinguishing the two regimes. In Figure 2-4b&c, the gap between normalized shear stress (black line; first term of RHS equation (4)) and rate and state friction (red dashed line; second term of RHS equation (4)) is a direct consequence of inertia; in particular the magnitude of the normalized inertial force (LHS of Equation (4)). During stick-slip motion (Figure 2-4b), the inertial term is apparent only in the short dynamic slip phase (see inset Figure 2-4b). Conversely, inertia is significant throughout the limit cycles observed during quasi-harmonic oscillations (Figure 2-4c).

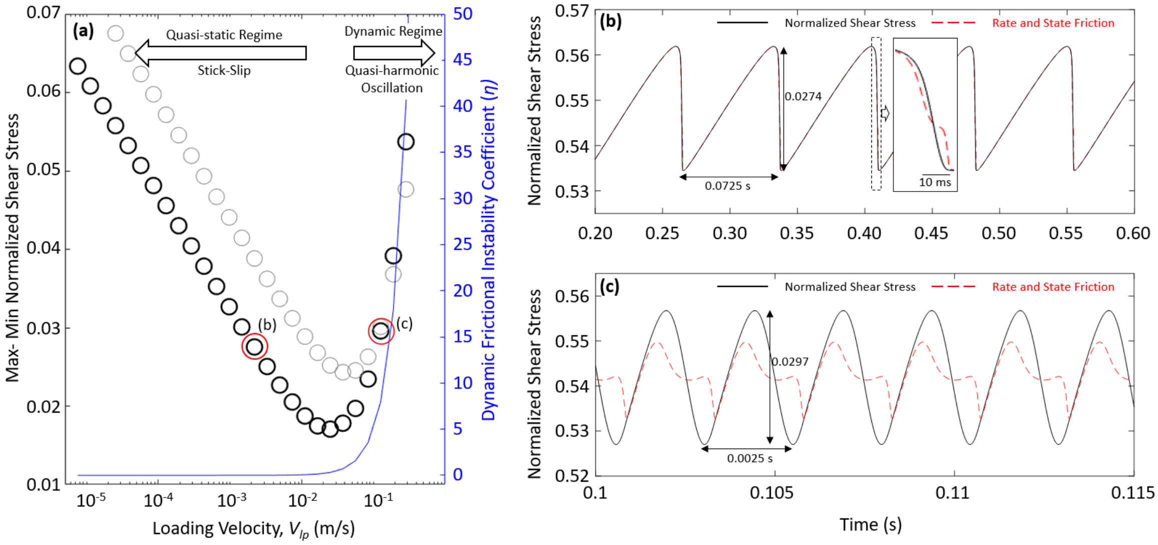

Figure 2-4 (a) Magnitude of friction limit cycles during stick-slip and harmonic oscillations for a range of loading velocities. We used the Ruina law with a = 0.005, b = 0.008, D_c = 10 μm, σ = 4 MPa and M = 100 kg/m^2 with K = 0.96 GPa/m (black) and K = 0.60 GPa/m (gray). These input parameters yield $K = 0.8\ K_{c,qs}$ and $K = 0.5\ K_{\mathrm{c,qs}}$ and therefore result in unstable motion regardless of the loading velocity. Panel (a) defines two distinct regimes: stick-slip sliding with quasi-static slip rates and dynamic motion defined by harmonic oscillations. The emergence of the dynamic regime coincides with the instability coefficient η (blue line) becoming ≥ 1. Panels (b) and (c) show examples of friction in each regime, stick-slip in (b) and quasi-harmonic oscillation in (c). Red and black curves represent normalized shear stress and rate and state friction, respectively. According to the force balance (Equation (4)), the gap between the black (normalized shear stress) and red (friction) curves represents the effect of inertia. In the stick-slip regime, inertia is only apparent during a short period of dynamic slip (panel (b) inset) whereas it is always significant in the dynamic regime of (c). Identical simulations with the Dieterich law are presented in the supplement.

It is also instructive to evaluate the two frictional instability regimes in terms of event frequency (Figure 2-5). Note the similarity to Figure 2-4a, which is expected given that an increase in loading rate results in an increase in event frequency. The log-linear relation between shear stress drop (magnitude) and frequency (or recurrence time) also appears in the quasi-static regime, showing that a larger magnitude of friction drop is associated with a longer duration of recurrence time. This behavior is well documented analytically, in lab data, and for natural earthquake cycles [Vidale et al., 1994; Marone et al., 1995; McLaskey et al., 2012; Beeler et al., 2001 and 2014; Im et al., 2017]. For higher frequency oscillations, the event magnitude reaches a minimum and increases significantly as loading rate increases (Figure 2-5). However, our results indicate that the increase in event frequency is limited by the natural frequency of the system ($f_n = (1/2\pi)\sqrt{K/M}$), which is 493 Hz for K = 0.96 GPa and 390 Hz for K = 0.60 GPa in these simulations (vertical red lines; M = 100 kg/m^2).

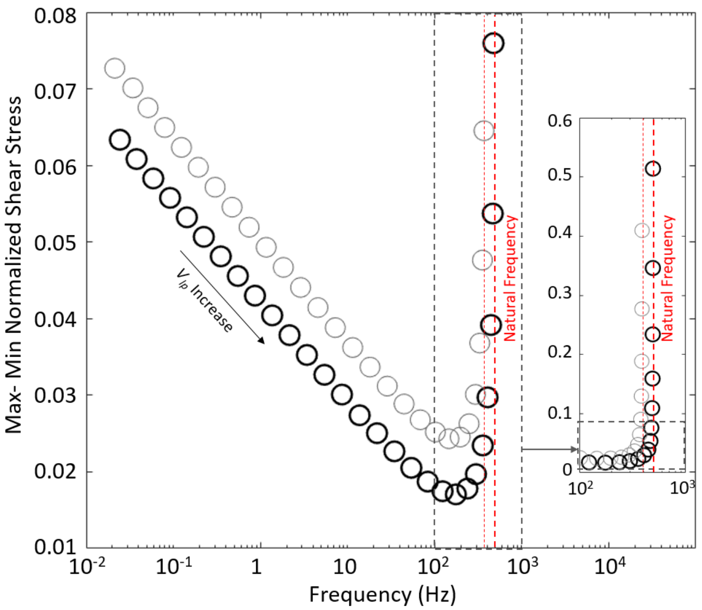

Figure 2-5 Max-min normalized shear stress vs. frequency at limit cycle with identical simulation results to Figure 2-4. Frequency generally increases with V_{lp}. However, frequency increases are limited at the natural frequency f_n (493 Hz for black and 390 Hz for gray) of the system. Extended simulation results to a larger loading rate are presented in inset, confirming that same limit is applied at the larger loading rates.

4. Discussion

4.1. Slow stick-slip at $K \sim K_c$

We observed that a quasi-harmonic oscillation emerges when $K < K_c$ and η is significant. Here we conduct a stable to unstable velocity stepping simulation similar to that in figure 2, but with only a small increase of η to observe the characteristics of friction with $K < K_c$ but where η is insignificant. We used identical friction parameters to the simulations in figure 2, but the loading velocity is increased from 10 µm/s to 200 µm/s - yielding $\eta = 0.002$ at $V_{lp} = 200$ µm/s. To achieve a stable to unstable transition for the given η, the stiffness of the system is set only slightly larger than the quasi-static critical stiffness ($K = 1.0005K_{c,qs}$) so that the stiffness become slightly smaller than the dynamic critical stiffness at $V = 200$ µm/s ($K = 0.9985K_c$).

The resulting friction is shown in figure 6, representing a stable – unstable transition at the loading velocity jump. The normalized shear stress (black line) and rate and state friction (red dashed line) almost fully overlap, representing that the inertial effect ($M\ddot{\delta}/\sigma$ in equation (4)) is insignificant. A zoomed-in plot (figure 6 inset) shows that the inertial effect is still insignificant even in the friction drop phase. This characteristic is inconsistent with general stick-slip motion which shows significant decoupling of normalized shear stress and friction at the friction drop (figure 4b and inset). Apparently the “slip” phase in figure 6 is much slower than that of stick-slip (figure 4b). In fact, this slow stick-slip motion at $K \sim K_c$ has been recognized in quasi-static (no inertia consideration) numerical simulations [e.g., Ruina, 1983] and, more recently, with experimental observation over a wide range of critical stiffnesses [Leeman et al., 2016]. Figure 6 shows that slow stick-slip also emerges even with full consideration of inertia, and the inertial effect remains insignificant throughout the whole process.

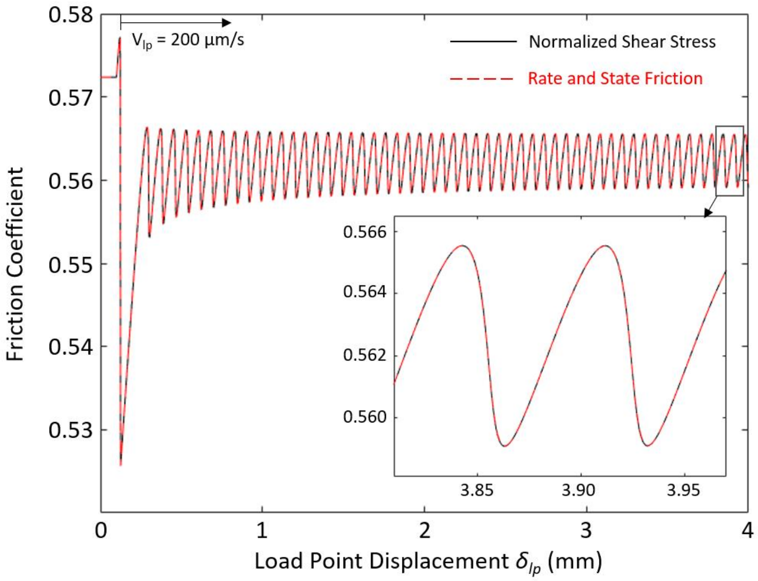

Figure 2-6 Friction response for velocity steps from 10 μm/s to 200 μm/s at load point displacement 0.1 mm. Frictional parameters, mass and normal stress are identical to the simulation in figure 2, but stiffness K is set to 1.0005 $K_{c,qs}$ to prompt an instability transition with only a slight increase is η. The dynamic frictional instability coefficient at 200 μm/s is η = 0.002. Black line denotes normalized shear stress and red dashed line denotes rate and state friction. Note that the black line and red dashed lines almost fully overlap.

4.2. Potential for frictional instability

The potential for the emergence of a dynamic instability significantly increases with slip velocity. Our analysis indicates that friction-induced vibration (harmonic oscillation) can potentially emerge in any system exhibiting velocity weakening friction (a - b < 0). The emergence of unstable sliding merely requires a sufficiently high slip velocity ($V > V_c$). Moreover, since the critical stiffness (or dynamic frictional instability coefficient η) increases with V^2, this velocity requirement can be easily met in fast slipping contacts such as those in mechanical parts for example, vehicle brake system. The potential for this emergence of instability can be decreased by reducing mass (η decrease) which, at the same time, will increase oscillation frequency once emerged.

The dynamic frictional instability coefficient (η) not only represents the potential for the emergence of frictional instability but also determines the instability regime. There is no clear boundary between the regimes presented in these simulations as transition from stick-slip to quasi-harmonic oscillation occurs gradually and it is also dependent on the stiffness of the system. However, one may use $\eta = 1$ to characterize instability regimes as suggested by Roy and Marone [1996], since it denotes the state where quasi-static and dynamic effects are identical and after this point, η increases rapidly with velocity. With the input parameters of the simulation in Figure 2-4, this is at $V = 4.47\times10^{-2}$ m/s which corresponds well with our transition zone.

4.3. Dynamic instability in natural fault system

Quasi-harmonic oscillations can also be observed in natural fault slip, as, so called, harmonic tremor. Harmonic tremors are frequently observed where applied loading rate or slip rate on the fault is temporarily increased, for example, by subsurface magma transfer (volcanic tremor) [Choudt, 1996; Dmitrieva et al., 2013] or by injection-induced slip [Das and Zoback, 2013; Derode et al., 2015]. In both cases, the fault contacts are forced to slip under continuous loading at increased velocity. This condition should significantly enhance the dynamic frictional instability coefficient ($MV^2/\sigma a D_c$), and may result in quasi-harmonic oscillation on the fault.

5. Conclusion

We show that frictional stability on high velocity slipping contacts is indeed controlled by inertia and related to dynamic effects. Furthermore, we observe that these dynamic effects determine the dynamic characteristics of the resulting unstable slip motions: stick-slip and quasi-harmonic oscillation. Magnitudes of shear stress oscillations decrease with increased velocity in the quasi-harmonic (stick-slip) regime while, it significantly increases with velocity in the dynamic (quasi-harmonic oscillation) regime. Frequency increases with increased velocity but there exists a frequency limit at the natural frequency of the system. Dynamic frictional instability coefficient ($\eta = MV^2/\sigma a D_c$) is a key parameter that defines the potential for dynamic instability and determines the dynamic characteristics of unstable slip motions.

Supplementary Material

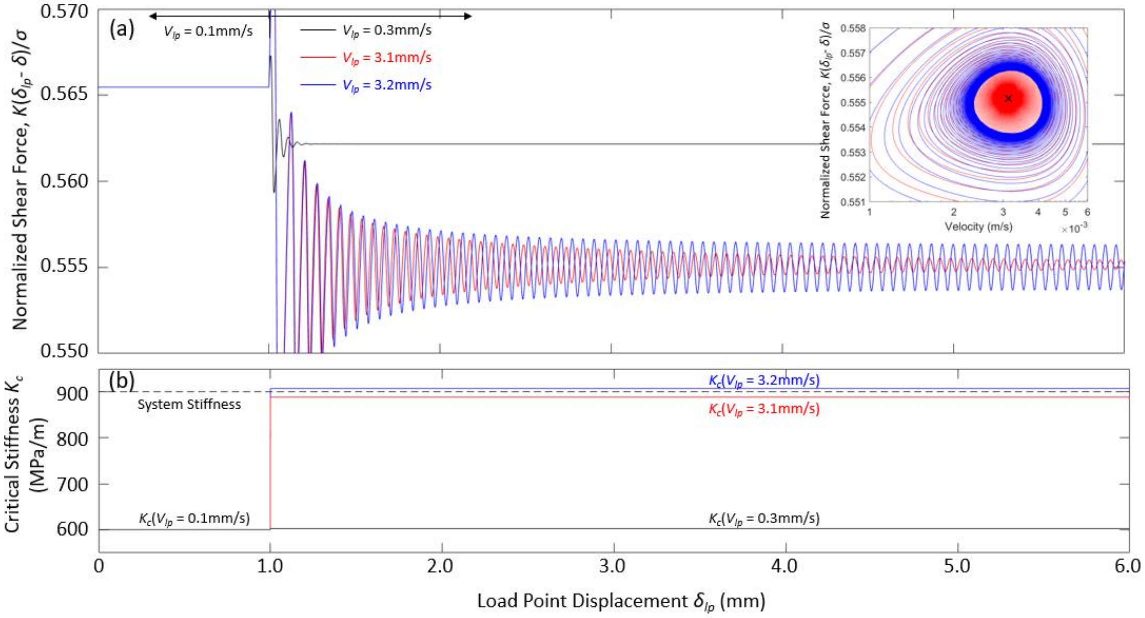

Figure 2-7 Simulation result identical to Figure 2 but with the Dieterich law. (a): Friction response to three velocity steps: (i) strongly subcritical velocity (0.3mm/s; black), (ii) slightly subcritical velocity (3.1 mm/s; red) and (iii) slightly supercritical velocity (3.2 mm/s; blue). Simulations used the Dieterich law with μ_0 = 0.6, $V_0 = 10^{-9}$ m/s, D_c = 10 µm, a = 0.003, b = 0.006, σ = 2 MPa and M = 3000 kg/m^2 with stiffness K set to 1.5 of the quasi-state critical stiffness (K = 900 MPa/m; $K_{c,qs}$ = 600 MPa). (b) Calculated critical stiffness for each case (colors correspond to those of panel a) with system stiffness also shown (black dashed line).

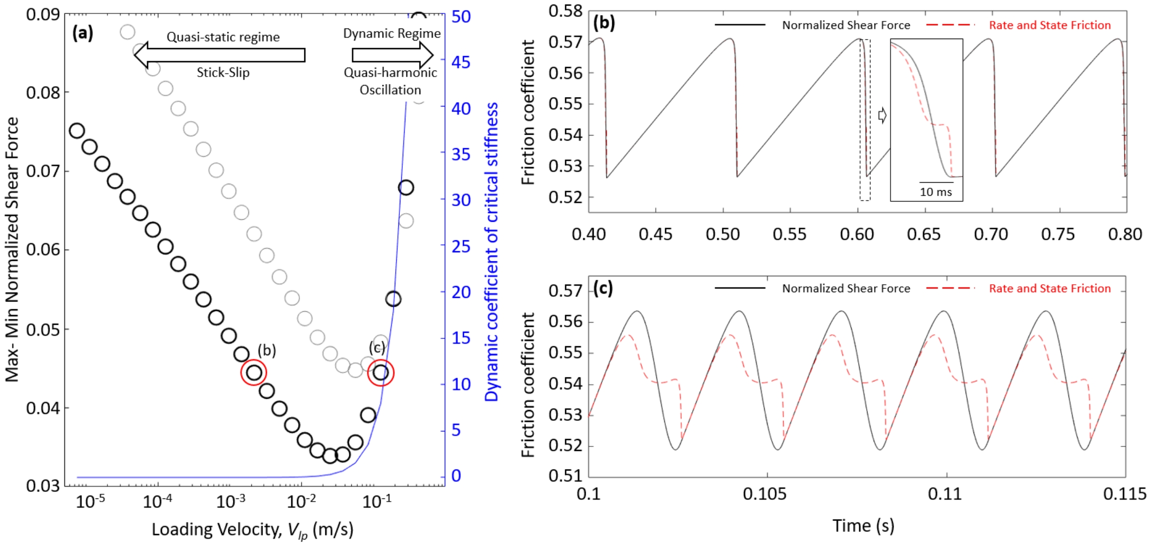

Figure 2-8 Simulation result identical to figure 4 but with the Dieterich law. (a) Magnitude of friction limit cycles during stick-slip and harmonic oscillations for a range of loading velocities. We used the Dieterich law with a = 0.005, b = 0.008, D_c = 10 µm, σ = 4 MPa and M = 100 kg/m^2 with K = 0.96 GPa/m (black) and K = 0.60 GPa/m (gray). These input parameters yield K = 0.8 Kc,qs and K = 0.5 Kc,qs and therefore result in unstable motion regardless of the loading velocity. Panels (b) and (c) show examples of friction in each regime, stick-slip (b) and quasi-harmonic oscillation (c). Red and black curves represent normalized shear stress and rate and state friction, respectively.

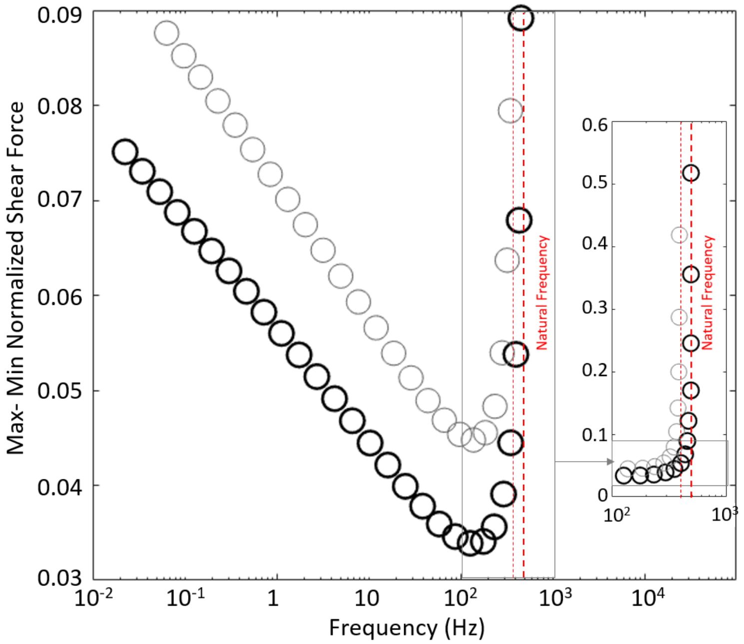

Figure 2-9 Simulation result identical to figure 5 but with the Dieterich law. Max-min normalized shear stress vs. frequency at limit cycle with identical simulation results to Figure S2. Frequency generally increases with V_{lp}. However, frequency increases are limited at the natural frequency f_n (493 Hz for black and 390 Hz for gray) of the system. Extended simulation results to a larger loading rate are presented in inset, confirming that same limit is applied at the larger loading rates.

Acknowledgement

This work is a partial result of support from the U.S. Department of Energy under projects DE-FE0023354. This support is gratefully acknowledged.

References

Ampuero, J.-P., and A. M. Rubin (2008), Earthquake nucleation on rate and state faults – Aging and slip laws, J. Geophys.Res., 113, B01302, doi:10.1029/2007JB005082

Baumberger, T., & Caroli, C. (2006). Solid friction from stick-slip down to pinning and aging. *Advances in Physics*, *55*(3–4), 279–348. https://doi.org/10.1080/00018730600732186

Baumberger, T., F. Heslot, and B. Perrin (1994), Crossover from creep to inertial motion in friction dynamics, Nature, 367, 544–546.

Bhattacharya, P., Rubin, A. M., Bayart, E., Savage, H. M., & Marone, C. (2015). Critical evaluation of state evolution laws in rate and state friction: Fitting large velocity steps in simulated fault gouge with time-, slip-, and stress-dependent constitutive laws. Journal of Geophysical Research: Solid Earth, 120, 6365–6385. https://doi.org/10.1002/2015JB012437

Bhattacharya, P., Rubin, A. M., & Beeler, N. M. (2017). Does fault strengthening in laboratory rock friction experiments really depend primarily upon time and not slip? Journal of Geophysical Research: Solid Earth, 122, 6389–6430. https://doi.org/10.1002/2017JB013936

Beeler, N. M., Hickman, S. H., & Wong, T. -f. (2001). Earthquake stress drop and laboratory-inferred interseismic strength recovery. *J. Geophys. Res.*, *106*(B12), 30701–30713. https://doi.org/10.1029/2000JB900242

Beeler, N. M., Tullis, T., Junger, J., Kilgore, B., & Goldsby, D. (2014). Laboratory constraints on models of earthquake recurrence. *Journal of Geophysical Research: Solid Earth*, *119*(12), 8770–8791. https://doi.org/10.1002/2014JB011184

Ben-David, O., Rubinstein, S. M., & Fineberg, J. (2010). Slip-stick and the evolution of frictional strength. *Nature*, *463*(7277), 76–79. https://doi.org/10.1038/nature08676

Brace, W.F., and Byerlee, J.D. (1966). Stick-slip as a mechanism for earthquakes: Science, v. 153, p. 990–992.

Bridgman, P. W. (1936). Shearing Phenomena at High Pressure of Possible Importance for Geology, The Journal of Geology 44, 653-669.

Bridgman, P.W. (1951). Some implications for geophysics of high-pressure phenomena. Geol. Sot. Am, Bull., 62: 533-536.

Brockley, C. A., & Ko, P. L. (1970). Quasi-Harmonic Friction-Induced Vibration. *Journal of Lubrication Technology*, 550–556.

Chouet, B. A. (1996). Long-period volcano seismicity: its source and use in eruption forecasting. *Nature*. https://doi.org/10.1038/380309a0

Das, I., & Zoback, M. D. (2013). Long-period long-duration seismic events during hydraulic stimulation of shale and tight-gas reservoirs — Part 2: Location and mechanisms. *Geophysics*, *78*(6), KS109-KS117. https://doi.org/10.1190/geo2013-0165.1

Derode, B., Guglielmi, Y., De Barros, L., & Cappa, F. (2015). Seismic responses to fluid pressure perturbations in a slipping fault. *Geophysical Research Letters*, *42*(9), 3197–3203. https://doi.org/10.1002/2015GL063671

Dieterich, J. H. (1979a). Modeling of rock friction: 1. Experimental results and constitutive equations. *J. Geophys. Res.*, *84*, 2161–2168.

Dieterich, J. H. (1979b). Modeling of rock friction: 2. Simulation of preseismic slip. *J. Geophys. Res.*, *84*, 2169–2175.

Dieterich, J. H., & Kilgore, B. D. (1994). Direct observation of frictional contacts: New insights for state-dependent properties. *Pagoeph.*, *143*(1–3), 283–302. https://doi.org/10.1007/BF00874332

Dmitrieva, K., Hotovec-Ellis, A. J., Prejean, S., & Dunham, E. M. (2013). Frictional-faulting model for harmonic tremor before Redoubt Volcano eruptions. *Nature Geoscience*, *6*(8), 652–656. https://doi.org/10.1038/ngeo1879

Gu, J.-C., Rice, J.R., Runia, A., and Tse, S., (1984), Slip motion and stability of a single degree of freedom elastic system with rate and state dependent friction: Journal of the Mechanics and Physics of Solids, v. 32, p. 167–196, doi: 10.1016/S0022-5096(98)00113-6.

Gu, Y., & Wong, T. (1991). Effects of loading velocity, stiffness, and inertia on the dynamics of a single degree of freedom Spring-Slider System. *J. Geophys. Res.*, *96*, 21677–21691. https://doi.org/10.1029/91JB02271

He, C., Wong, T., & Beeler, N. M. (2003). Scaling of stress drop with recurrence interval and loading velocity for laboratory-derived fault strength relations. *J. Geophys. Res.*, *108*(B1), 2037. https://doi.org/10.1029/2002JB001890

Heslot, F., Baumberger, T., Perrin, B., Caroli, B., & Caroli, C. (1994). Creep, stick-slip and dry-friction dynamics: Experiments and a heuristic model. *Physical Review E*, *49*(6).

Ibrahim, R. A. (1994). Friction-induced vibration, chatter, squeal, and chaos Part I : Mechanics of contact and friction. *Appl. Mech. Rev.*, *47*, 209–226.

Im, K., Elsworth, D., Marone, C., & Leeman, J. (2017). The impact of frictional healing on stick-slip recurrence interval and stress drop: Implications for earthquake scaling. *Journal of Geophysical Research: Solid Earth*. https://doi.org/10.1002/2017JB014476

Kammer, D.S., VA Yastrebov, G Anciaux, JF Molinari, (2014) The existence of a critical length scale in regularised friction, Journal of the Mechanics and Physics of Solids 63

Kammer, DS, M Radiguet, JP Ampuero, JF Molinari, (2015) Linear elastic fracture mechanics predicts the propagation distance of frictional slip, Tribology Letters 57

Karner, S. L., & Marone, C. J. (2000). Effects of loading rate and normal stress on stress drop and stick slip recurrence interval. *GeoComplexity and the Physics of Earthquakes*.

Leeman, J. R., Saffer D.M., Scuderi, M.M & Marone, C., (2016). Laboratory observations of slow earthquakes and the spectrum of tectonic fault slip modes. Nat. Commun. 7:11104 doi: 10.1038/ncomms11104

Luo, Y., & Ampuero, J.-P. (2018). Stability of faults with heterogeneous friction properties and effective normal stress. *Tectonophysics*, *733*, 257–272. https://doi.org/10.1016/J.TECTO.2017.11.006

Mair, K., Frye, K. M., & Marone, C. (2002). Influence of grain characteristics on the friction of granular shear zones. Journal of Geophysical Research, 107(B10), 2219. https://doi.org/10.1029/2001JB000516

Marone, C., Vidale, J. E., & Ellsworth, W. L. (1995). Fault healing inferred from time dependent variations in source properties of repeating earthquakes. *Geophys. Res. Lett.* https://doi.org/10.1029/95GL03076

Marone, C. (1998a). Laboratory-Derived Friction Laws and Their Application To Seismic Faulting. *Annual Review of Earth and Planetary Sciences*, *26*(1), 643–696. https://doi.org/10.1146/annurev.earth.26.1.643

Marone, C. (1998b). The effect of loading rate on static friction and the rate of fault healing during the earthquake cycle. Nature, 391(6662), 69–72. https://doi.org/10.1038/34157

McLaskey, G. C., Thomas, A. M., Glaser, S. D., & Nadeau, R. M. (2012). Fault healing promotes high-frequency earthquakes in laboratory experiments and on natural faults. *Nature*, *491*(7422), 101–104. https://doi.org/10.1038/nature11512

Perfettini, H., & Molinari, A. (2017). A micromechanical model of rate and state friction: 1. Static and dynamic sliding. *J. Geophys. Res.: Solid Earth*, *122*(4), 2590–2637. https://doi.org/10.1002/2016JB013302

Rabinowicz, E. (1951). The nature of the static and kinetic coefficients of friction. *J. Appl. Physc*, *22*, 1373–1379.

Rabinowicz, E. (1956), Stick and Slip, Sci. Am., 194(5), 109–119, doi:10.1038/scientificamerican0556-109.

Ranjith K and Rice JR (1999) Stability of quasi-static slip in a single degree of freedom elastic system with rate and state dependent friction. Journal of the Mechanics and Physics of Solids 47: 1207–1218.

Rice, J. R. (1993). Spatio-temporal complexity of slip on a fault. *J. Geophys. Res.*, *98*(B6), 9885. https://doi.org/10.1029/93JB00191

Rice, J. R., N. Lapusta, and K. Ranjith (2001), Rate and state dependent friction and the stability of sliding between elastically deformable solids, J. Mech. Phys. Solids, 49(9), 1865–1898, doi:10.1016/S0022-5096(01)00042-4.

Rice, J. R., & Ruina, A. L. (1983). Stability of Steady Frictional Slipping. *Journal of Applied Mechanics*, *50*(2), 343. https://doi.org/10.1115/1.3167042

Rice, J. R., & Tse, S. T. (1986). Dynamic motion of a single degree of freedom system following a rate and state dependent friction law. *J. Geophys. Res.*, *91*(1), 521–530.

Roy, M., & Marone, C. J. (1996). Earthquake nucleation on model faults with rate and state friction: Effects of inertia. *J. Geophys. Res.*

Ruina, A. (1983). Slip instability and state variable friction laws. *J. Geophys. Res.*, *88*, 10359–10370.

Scholz, C. H. (2002), The mechanics of earthquakes and faulting, Cambridge university press.

Scuderi, M. M., Carpenter, B. M., Johnson, P. A., & Marone, C. (2015). Poro mechanics of stick-slip frictional sliding and strength recovery on tectonic faults. Journal of Geophysical Research, 120, 6895–6912. https://doi.org/10.1002/2015JB011983

Singh, B. R. (1960). Study of Critical Velocity of Stick-Slip Sliding. J. Eng. Ind 82(4), 393-398 doi:10.1115/1.3664261

Shimamoto, T., Handin, J., & Logan, J. M. (1980) Specimen-apparatus interaction during stick-slip in a triaxial compression machine: A decoupled two-degree-of-freedom model, Tectonophysics, 67, 175- 205, doi: 10.1016/0040-1951(80)90234-6

Svetlizky, I., Bayart, E., Cohen, G., & Fineberg, J. (2017). Frictional Resistance within the Wake of Frictional Rupture Fronts. *Phys. Rev. Lett.*, *118*(23), 1–5. https://doi.org/10.1103/PhysRevLett.118.234301

Tian, K., Gosvami, N. N., Goldsby, D. L., Liu, Y., Szlufarska, I., Carpick, R. W. (2017) Load and time dependence of interfacialchemical bondinduced friction at the nanoscale. Phys. Rev. Lett., 118 (7), 076103

van den Ende, M. P. A., Chen, J., Ampuero, J.-P., & Niemeijer, A. R. (2018). A comparison between rate-and-state friction and microphysical models, based on numerical simulations of fault slip. *Tectonophysics*, *733*, 273–295. https://doi.org/10.1016/J.TECTO.2017.11.040

Vidale, J. E., Ellsworth, W. L., Cole, A., & Marone, C. J. (1994). Variations in rupture process with recurrence interval in a repeated small earthquake. *Nature*, *368*(6472), 624–626. https://doi.org/10.1038/368624a0

Chapter 3

The Influence of Pre-Slip Sealing on the Permeability Evolution on Fractures and Faults

Abstract

The evolution of permeability on fractures and faults during the full earthquake cycle is shown to be sensitive to sealing during the repose phase. We explore the combined effect of static loading followed by fracture reactivation on permeability evolution via slide-hold-slide experiments. During the hold periods, permeability exhibits a slow but continuous reduction. The permeability decay is consistent with power law compaction of the aperture coupled with cubic law flow. With increasing hold periods, permeability evolves following reactivation from net reduction to net increase with the magnitude of the permeability change dependent on the hold period. This implies that the tight interlocking of asperities during inter-seismic repose primes the fault for permeability enhancement following reactivation. The inferred mechanism is *via* shear dilation with the probable involvement of unclogging. This result identifies that pre-slip sealing during repose is an essential component in the cyclic permeability evolution throughout the seismic cycle.

1. Introduction

The evolution of permeability on fractures and faults is known to be sensitive to changes in effective stresses. Permeability evolves as a result of both static and dynamic stress perturbations throughout the earthquake cycle [Rojstaczer and Wolf, 1992; Roeloffs, 1998; Brodsky et al., 2003; Manga et al., 2003; Elkhoury et al., 2006; Manga et al., 2011; Wang and Manga, 2015; Wang et al., 2016], as a result of reservoir stimulation [Zoback et al., 2012; Mukuhira et al., 2017] and potentially in the sequestration of energy wastes [Fang et al., 2017]. Shear dilation contributes to increases in permeability and has been explored with analytic models [Elsworth and Goodman, 1986; Liu et al., 2000; Hossain et al., 2002] and field scale observations [Guglielmi et al., 2015]. Not surprisingly, this response exhibits some of the attributes of rate dependent properties of fault friction [Ishibashi et al., 2016; Fang et al., 2017] as implied by rate-state characterizations of fault friction and shear dilation [Segal and Rice, 1995; Samuelson et al., 2009].

Observations have demonstrated the importance of comminution/compaction in conditioning permeability evolution [Zhang et. al., 1998; Faoro et. al., 2009; Fang et. al., 2017], especially at the initiation of slip. However, this response may be spuriously influenced by artifacts of the initial experimental conditions (an artificial surface and fresh contacts) and do not necessarily represent a fault that has healed and sealed during its interseismic repose. Pressure solution and stress corrosion during static loading [Lehner, 1995; Polak et. al., 2003; Yasuhara and Elsworth, 2004 & 2008; Yasuhara et al, 2006; Gratier et al., 2014; Chen and Spiers, 2016] may tightly interlock asperities and develop local roughness on the contact surface. Shear slip on the tightly mated surface may subsequently induce sustained (long-duration) dilation *via* asperity dislocation. Thus, the incorporation of healing and concomitant sealing during repose may be an essential requirement to follow the correct evolution of permeability. Such sealing has been inferred both at field and laboratory scales [Elkhoury et. al., 2006 & 2011; Giger et al., 2007; Xue et al., 2013; Wang et al., 2016], over periods of years to hours, together with permeability enhancement at the onset of dynamic loading and slip.

In the following, we investigate the combined effect of static loading and shear deformation on fracture permeability. We measure permeability continuously during shear reactivation of fractures with intervening periods of static loading on samples of Westerly granite and Green River shale.

2. Experimental Method

We explore this response through fluid-through-flow experiments in a triaxial pressure cell with independent application of confining pressure, shear stress and pore pressure (see Fig. 1a). A prismatic rock coupon in double direct shear configuration (35mm × 24mm × 3 mm) is sandwiched between half-cylindrical cores within a latex jacket. This experimental configuration enables accurate measurement of friction by minimizing the impact of jacket/membrane restraint. Experimental variables include surface roughness (ground with #150 grit (rougher) and #600 grit (smoother) aluminum powder) and mineralogy (Westerly granite (WG, tectosilicate > 90%) and Green River shale (GRS, tectosilicate ~ 46%, carbonate ~ 52% and phyllosilicate ~2% [Fang et al., 2017])).

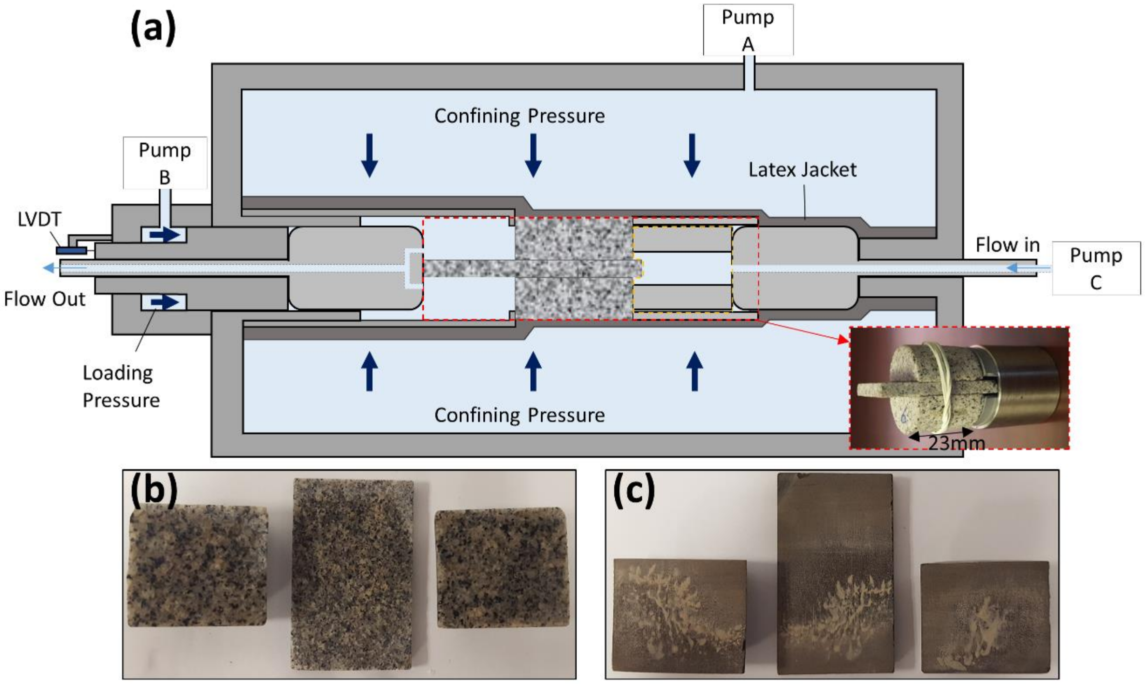

Figure 3-1 (a): Experimental configuration. Servo pumps control confining stress (pump A), loading pressure (pump B) and flow pressure difference (pump C). Bottom right picture in (a) shows the Westerly granite sample used in this experiment. (b) and (c) shows surface conditions after experiments for Westerly granite and Green River shale respectively. Orange dashed box denotes inlet chamber that affects apparent permeability (see text).

The permeating fluid is de-ionized and de-aired water supplied from an upstream pump and flowing along the two parallel fractures (Figure 3-1). The confining/normal stress, inlet/outlet pressure difference and shear loading rate are independently controlled by three servo-controlled pumps. Pump A controls confining pressure which is retained constant at 3 MPa. Loading rate and induced shear stress are controlled/measured by pump B with prescribed flowrate. Displacement rates are confirmed through the volume rates of pump B together with measurements of an LVDT connected to the loading piston. Resulting flow rates are recorded continuously during multiple slide and hold experiments by pump C, with longitudinal fluid pressure differences limited to 30kPa to 200 kPa (~7% of total stress) for all experiments.

Permeability (k) is calculated from Darcy's law as:

$$k = \frac{\mu L}{A} \frac{Q}{\Delta P} \tag{11}$$

where μ is fluid viscosity (8.9×10^{-4} Pa·s), L flow path length (23mm), A is cross sectional area of the sample perpendicular to the flow path (4.71×10^{-4} m^2), Q is flow rate and ΔP is the pressure difference across the sample. In this configuration, flow rate Q is directly proportional to the permeability evolution as L, A and ΔP are constant.

This novel experimental configuration enables concurrent and continuous measurement of both permeability and friction throughout static and dynamic motion - but entrains a minor artifact that appears in the experimental results. When the upstream reservoir volume (orange dashed line in Figure 3-1a) is reduced by shear slip, an identical volume is also reduced in the flow rate of pump C to maintain constant pressure. Due to this effect, a false step reduction of "apparent" permeability appears at the activation of shear slip (and step increase at hold). This effect is generally trivial, but can be observable when the flow rate is also small. Apparently, these effects are inconsequential for the experiments reported here.

We conduct slide-hold-slide (SHS) experiments in modes involving: (i) five single long holds and also as (ii) three repeating slide-hold-slides (see table S1 for experiment list). All experiments initiate with the application of confining pressure (3 MPa) followed by the pressure-saturation of the sample until flow stabilizes. The samples are sheared-in at a constant velocity 10 μm/s. The single long hold mode is designed to investigate sealing behavior during the hold period therefore only one long hold is applied after initial shear reaches a preset distance (3~7 mm). For the repeating slide-hold-slide mode, initial shear displacements are set to 2 mm followed by hold periods punctuated by reactivations (slide-hold-slide). The hold periods, representing interseismic repose, are systematically increased for the SHS experiment between intervening shear phases. Successive incremental hold periods are of 10s, 30s, 100s, 300s, 1000s, 3000s and 10000s with intervening reactivations of 1 mm at a velocity of 10 μm/s. Exceptions to these conditions are where the pump was already empty before the final 10000s hold (rougher granite) and where an extra hold (5000 s) was applied after the final slip period (smoother granite).

3. Results

3.1 Sealing

Figures 2 present five long hold mode experiment results. All specimens exhibit continuous decay without evidences of stabilization within the experimental duration. The curves initially appear to follows linear trend in log-log plot. However, after a few hours, the curves deviate from the linear trend towards faster decay.

Interestingly, these results are plausibly described as power law compaction (in time) [e.g. Gratier et al., 2014], coupled with permeability evaluated from the cubic law. Assuming that compaction follows a power law, time-dependent aperture reduction (Δb) can be described by a power exponent n as,

$$\Delta b = \alpha t^{n} \tag{12}$$

where t is time and α is the compaction displacement at t = 1. Permeability k may be defined relative to compaction in aperture (Δb) [Witherspoon et al., 1980; Ouyang and Elsworth, 1993] as

$$k = k_0 \left(1 - \frac{\Delta b}{b_0} \right)^3 \tag{13}$$

where k_0 and b_0 denote an initial permeability and aperture, respectively. Substituting equation (2) into (3) yields,

$$k = k_0 \left(1 - \frac{\alpha}{b_0} t^n \right)^3 . \tag{14}$$

The resulting model fits and experimental results are presented Figures 3-2a and b using Equation (4) with parameters (k_0, α/b_0 and n) presented Figure 3-2c. The plots show that the model adequately represents permeability reduction behaviors with the power exponents n = 0.3 ~ 0.4.

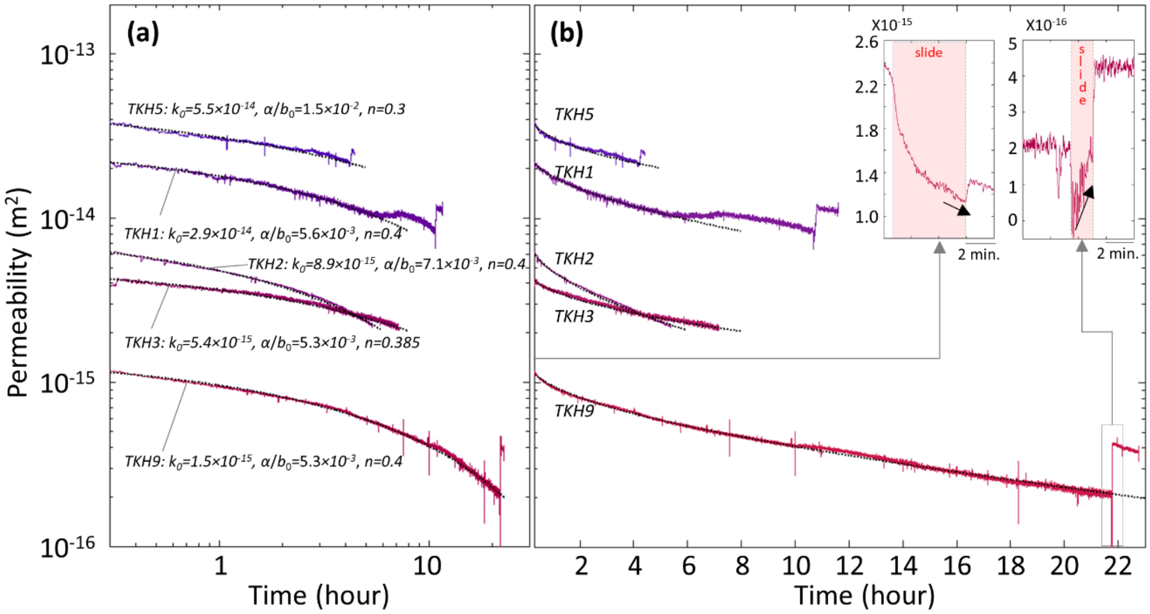

Figure 3-2 Permeability decay with time. Five single long hold experiments conducted with Westerly Granite with different roughnesses shown on (a) log-log and (b) log-linear scales. Time-zero is set when normal stress reaches 3MPa. Black dotted lines, overlapping on the experimental result, are model fits using power law compaction and cubic law for flow (see text for method) with fitting parameters listed in panel (a). Insets in figure (b) shows permeability response of TKH9 for an initial 3 mm slip (left) and further 1mm slip after ~21 hours of hold (right). The temporal permeability reductions during slip in the insets are artifacts due to the volume of sample intrusion into the inlet chamber. Step increase of permeability of TKH1 and TKH5 result from shear slip. We do not have a clear explanation for the gradual permeability enhancement of TKH1 shown at time ~6-8 h, but find that it occurs with gradual shear stress reduction (not shown here).

We estimate the magnitude of compaction during the hold by converting the permeability to equivalent hydraulic aperture (h) of each fracture with the cubic law relation [Witherspoon et al., 1980],

$$h = \left(\frac{Q}{2} \frac{L}{\Delta P} \frac{12\mu}{w} \right)^{\frac{1}{3}} \tag{15}$$

where the notations are identical to equation (1) with w denoting fracture width (21mm). Note that Q is halved since our experimental configuration embeds two fractures. Figure 3-2 shows that the longest hold experiment (TKH9) resulted in an ~85%

permeability decline during ~22 hours of hold (from $k = 1.4\times10^{-15}$ m^2 to 2.1×10^{-16} m^2). From equations (5) and (1), this yields 2.6 µm of equivalent hydraulic aperture change (from 5.7 µm to 3.1 µm), illustrating the extreme sensitivity of permeability to aperture change.

The shear permeability responses of TKH9 are zoomed-in in the upper right portion of Figure 3-2b, showing a clear conversion from shear-induced permeability destruction to enhancement. The left inset shows permeability response with the initial 3 mm slip and the right inset shows permeability response with 1 mm slip after ~22 hours of hold (note that these plots include small artificial permeability reductions at the slide/hold boundary noted in section 2). A trend of permeability decrease for the initial 3 mm of slip (red background) continues until the hold phase begins (shear/hold boundary shows the artifacts discussed in section 2). This declining trend reverses into significant enhancement after 22 hours of hold, resulting in a roughly 100% increase in permeability during the subsequent 1mm of slip.

3.2 Permeability response to repeating slide-hold-slide motion

Figure 3-3 shows shear stress and flow rate responses during slide-hold-slide experiments extending for ~6 hours. Periods of slip and intervening hold are denoted by the top bar of Figure 3-3a with experiments exhibiting typical rate-state frictional response. Applied shear stresses decline during the hold then increase sharply to a peak during reactivation before stabilizing following rate and state friction [Marone 1998]. The magnitude of the peak stress increases with the increased duration of the prior hold period, representing time-dependent frictional healing.

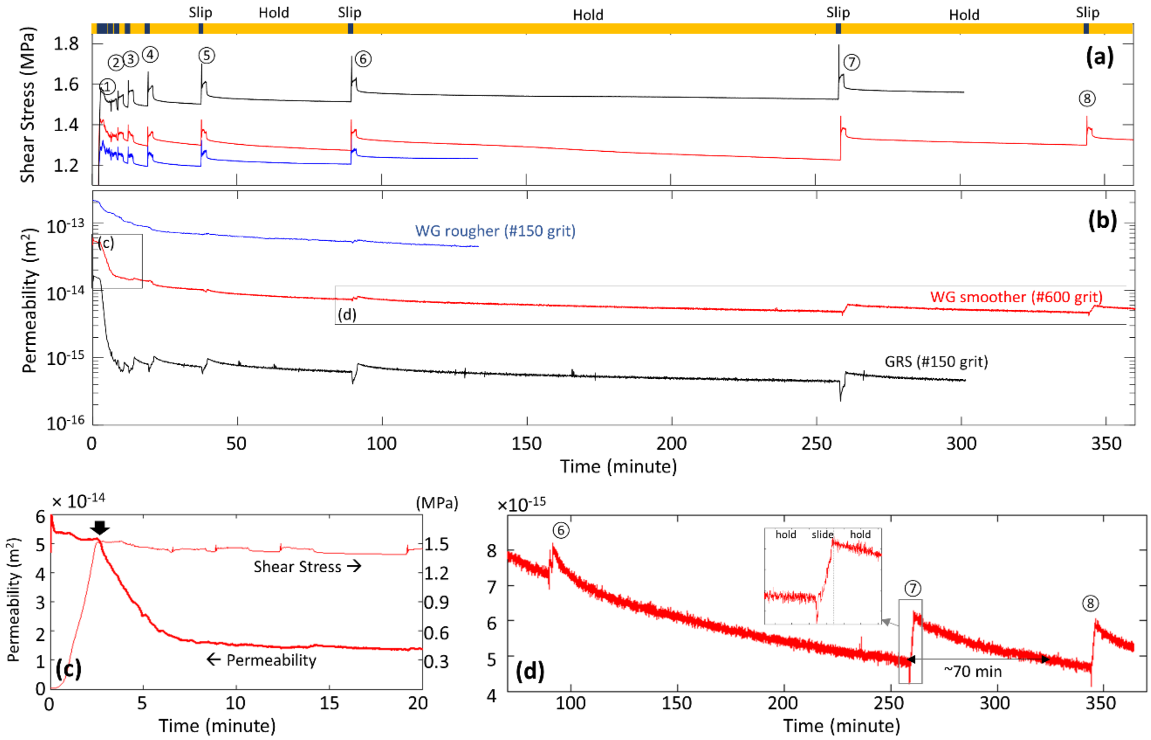

Figure 3-3 Friction and permeability response during slide and hold experiments. Each color denotes rock and surface roughness: blue: Westerly granite rougher sample (#150 grit); red: WG smoother (#600 grit); and black: Green River shale (#150 grit). Panels (a) and (b) are shear stress and permeability response during the overall experiment respectively. Slip and hold periods are denoted on the top of (a) by blue and orange bar respectively. Panels (c) and (d) are zoomed-in views of the box insert in panel (b). The downward arrow in (c) represents the initiation of shear slip. Single responses to sliding are highlighted in the small box in (d). Detailed view of WG rougher and GRS cases are provided in the supplement (Figure 3-5).

Figure 3-3b presents permeability evolution for all cases. It shows that the permeability is larger for rougher sample (#150 grit) than smoother sample (#600 grit) and harder sample (WG) than weaker sample (GRS). This observation naturally resulted from larger aperture (or pore throat) with rougher surface, and may reflect significant pore throat destruction during application of normal stress on weak rock surface (GRS).

Early time response in figure3b shows the decline rate in permeability is anomalously large during the initial shearing-in period for all samples. A zoomed-in view of the initial decline (Figure 3-3c) shows that this initial permeability reduction immediately follows the initiation of shear slip (i.e., driven by slip) and the decline rate is significantly reduced after a few millimeters of slip. Normalized permeability reduction during this initial period is greater for weaker rock (GRS) than for stronger/harder rock (WG) and with smoother rather than rougher surfaces (see Figure 3-2b early time). These observations, together with the observed production of comminution products (shale) during the experiment (Figure 3-1c) suggest that the initial strong permeability reduction is mainly as a result of comminution/compaction and wear products from the fracture surfaces. This is especially dominant on fresh artificial samples which may not necessarily represent natural faults and fractures.

Further reactivations following incremented durations of static loading (hold periods) show significant permeability enhancements. Figure 3-3d highlights the permeability responses of the later stage reactivations and inter-slip holds of smoother WG (period identified by rectangles in Figure 3-2b). This plot clearly identifies a cyclic repetition of permeability destruction (inter-slip sealing) and then creation (shear permeability enhancement). For instance, permeability continuously decreases during the 10000s hold between slips ⑥ and ⑦ yielding a permeability reduction of ~37.5 % (from ~ 8×10^{-15} m^2 to ~ 5×10^{-15} m^2). In the following slip ⑦, permeability increases by ~ 25% within 1 mm of shear deformation (< 5% of sample length) before permeability again decreases at the conclusion of the slip phase. It takes ~70 minutes to recover to the original permeability prior to the slip ⑦.

Zoomed-in views in Figure 3-3d shows that the permeability enhancement behaviors are gradual as observed in the inset of Figure 3-2b. Permeability continues to increase over 1 mm slips. This length scale (> 1 mm) is far larger than critical displacements for the evolution of friction observed in these experiments (10 ~ 20 μm, see Figure S1). The permeability evolution does not show an abrupt destruction at the beginning of the hold phase - conversely it exhibits a sustained and slow decline. These behaviors are similarly observed in the two other cases (see Figure S2).

3.3 Permeability enhancement and hold duration

SHS experiments (Figure 3-3) shows initial reactivation results in a strong reduction in permeability but this switches to significant enhancement after an extended period of healing (later stage slips). These are exhibited in Figure 3-4a (rougher WG), 4b (smoother WG) and 4c (GRS) with response typified by Figure 3-4a (rougher granite). This represents sequential changes in permeability response that show significant net initial declines (①, ②, ③ and ④), transitioning to a net increases (⑤) that becomes more significant (⑥).

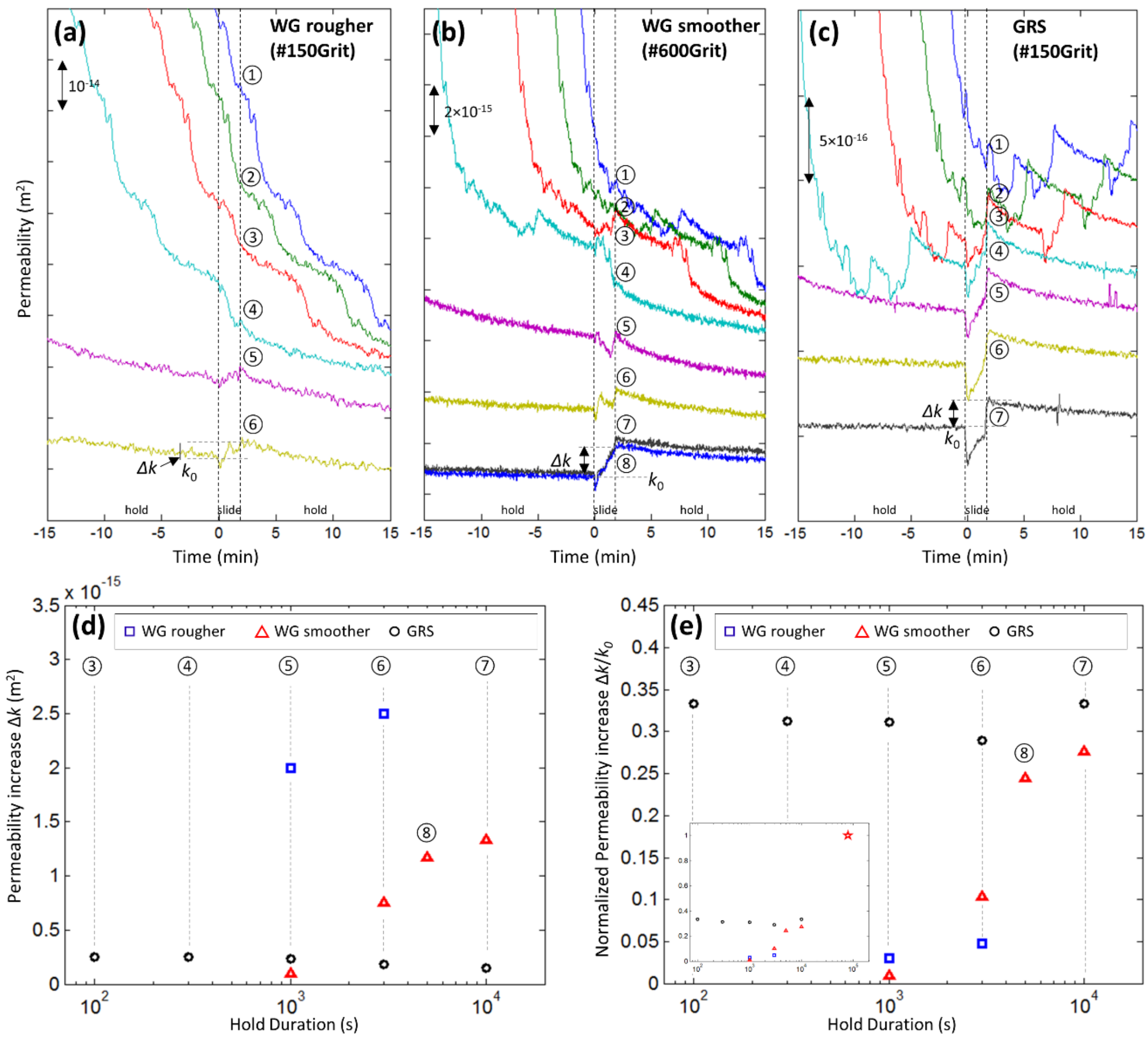

Figure 3-4 Sequence of permeability evolution of (a): WG rougher, (b): WG smoother and (c): GRS. All slip events are aligned with reactivation (t=0s). Panels (d) and (e) exhibit absolute (d) and normalized (e) permeability enhancement vs. hold duration. Definition of permeability enhancement *Δk* and initial permeability k_0 are shown in Figures (a), (b) and (c). Circled numbers correspond to event number in Figure 3-2. The colors and symbols denotes rock and roughness: WG rough (blue square), WG smooth (red triangle), and GRS (black circle). Inset in panel (e) includes TKH9 results (Figure 3-3c insets) denoted by red star.

Permeability enhancements resulting from various hold durations are shown in Figures 4d (absolute increase Δ*k*) and 4e (normalized increase, $\Delta k/k_0$). The larger ultimate enhancements scale increasing roughness and hardness, implicating the essential role of shear dilation. The magnitude of absolute permeability enhancement (Figure 3-4d) is largest with stiffer/stronger/rougher granite and smallest with weaker/smoother shale. Conversely, the magnitude of normalized permeability enhancement (Figure 3-4e) is largest with shale and smallest with rougher granite. This behavior is substantially implied by the cubic law (Equation (3)). Although shear aperture increase ($-\Delta b$) is largest with a rougher/hard surface, normalized permeability enhancement can be smallest due to the large initial aperture (b_0).

The permeability enhancement of westerly granite significantly increases with an extended duration of healing in both absolute (Figure 3-4d) and relative magnitudes (Figure 3-4e), implying, especially for hard rock, that the magnitude of shear permeability enhancement is dependent on the pre-slip healing/sealing. For the case of the smoother granite (Figure 3-4d), no shear permeability enhancement appears after only short healings, ~1% of enhancement induced after 1000 seconds of healing and ~27% after 10000 seconds. Permeability enhancement appears approximately log-linear with pre-slip hold duration. The inset in Figure 3-4e shows the largest normalized permeability enhancement is achieved with the longest hold time (TKH9, Figure 3-3c insets)

4. Discussion

4.1 Mechanism for permeability evolution

Shear slip may destroy the permeability by comminution/compaction or conversely create it by breaching the mated contact surface. These two contrasting behaviors may be controlled by the fidelity of the interlocking surfaces, *i.e.* sealing. For instance, if the two surface asperities are strongly mated *via* long-duration healing and sealing, shear slip may result in permeability enhancement. Conversely, if the surfaces are artificially prepared, fresh, and unsealed, shear slip may collapse bridging contacts and result in strong permeability reduction.

Strong permeability reduction is observed upon initial shear reactivation. Normalized permeability reduction is larger for weaker rocks (GRS) and smoother surface textures (#600 grit). The presence of observable wear product with GRS (Figure 3-1c) suggests that initial strong permeability reduction is driven by shear comminution effects. These observations, and those of prior studies [e.g. Zhang et. al. 1998, Faoro et. al. 2009, Tanikawa et. al. 2010, Ishibashi et. al, 2016, Fang et. al. 2017], demonstrate that this strong permeability reduction is especially significant during the initial shear-in process on fresh, laboratory-prepared surfaces.

Conversely, sealing is always active even when the influence of comminution becomes trivial. In our experiments, permeability decay can be plausibly described by power law compaction coupled with the cubic law. The slow but continuous permeability decay may imply that mechano-chemical effects governs the sealing behavior observed in these experiments. Interestingly, despite the difference in contact geometry, power law compaction is analogously observed with solution driven transport around a rigid indenter and exhibits a similar range of power exponents (0.3~0.4) [Gratier et al., 2014]. Since the dissolution rate of quartz is known to be insignificant at room temperature [Dove and Crerar, 1990], stress corrosion [Polak et al. 2003; Yasuhara and Elsworth, 2008] may primarily drive this slow compaction process. This may be aided by pressure solution of fine wear products that may be bridged in between the contacts, by mineral precipitation on the pore space and by flux driven wear product clogging.

Dilation is inferred by the absolute magnitude of permeability creation being largest for harder (granite) and rougher surfaces. The process of shear dilation and frictional properties (rate and state) imply a rate dependency of permeability consistent with strength evolution on faults [Ishibashi et al., 2016; Fang et al., 2017]. The rate dependency of fracture aperture (porosity) model is suggested by anticipated dilation rates [Segall and Rice, 1995; Samuelson et al., 2009],

$$\phi_{ss} = \phi_0 + \varepsilon \ln\left(\frac{v}{v_0}\right) \tag{16}$$

where ϕ_{ss} is steady state porosity, ϕ_0 is reference porosity, ε is dilatancy coefficient, v is velocity and v_0 is reference velocity. If coefficients ϕ_0 and ε are constants, then, absent the production of wear products, permeability enhancement via constant shear velocity is only dependent on the magnitude of pre-slip sealing. Where permeability scales as $k/k_0 = (1 + \Delta\phi/\phi_0)^3$ (Equation 3), a significant shear permeability enhancement will result on a strongly sealed fracture. Dilation is inferred by the observation that the absolute magnitude of permeability creation is largest for the harder (granite) and rougher surfaces.

We observe a gradual enhancement in shear permeability. Permeability enhancement occurs over a longer distance (> 1mm) than the critical frictional slip distance (D_c~10-20 µm, Figure S1). And the permeability reduction is also slow and gradual as observed by natural permeability response to earthquakes [Elkhoury et. al., 2006; Xue et al., 2013]. Such a gradual evolution has been observed in some existing studies on shear dilation [Neimeijer et al., 2008 & 2010; Chen et al., 2015] and permeability evolution [Ishibashi et al., 2016; Fang et al., 2017] including models of granular friction and permeability [Wang et al., 2017].

The presence of wear products in GRS sample (figure 3-1c) suggest that the permeability enhancement may be associated with flux-driven unclogging of the fracture [Elkhoury et al., 2011; Candela et al., 2014; Candela et al., 2015]. Although our experiments are conducted with constant pressure, pore throat expansion due to shear dilation may trigger the release of trapped wear products and unclog any colloidal seal. We mimic prior oscillatory pressure pulse experiments with WG (see Figure S3) and confirm that significant permeability enhancement may result. Moreover, these experiments confirm that permeability can be further enhanced when shear slip (induced seismicity) is triggered by the pressure pulse. The difference in the amount of visible wear product between WG and GRS (figure 3-1b and 1c) suggests that the observed difference in permeability response to shear (Figure 3-4d and e) can also be influenced by the unclogging process.

4.2 Implication to natural systems

These experiments suggest that commonly observed co- and post-seismic permeability enhancements may also be contributed to by shear slip. Our experiments suggests pre-slip sealing is an essential process to allow shear permeability enhancement. Indeed, the sealing process is inferred by field observations that show permeability reduction [Elkhoury et. al., 2006; Xue et al., 2013] and hydraulic decoupling of aquifers [Wang et al., 2016] following co-seismic reactivation. A long duration of inter-seismic sealing can reset the fault permeability, priming it for another cycle of co-seismic permeability enhancement followed by its slow destruction.

These experimental results recall the potential of permeability characterizations as potentially sensitive earthquake precursors [e.g. Roeloffs, 1998 & 2006]. Seismic events may transition through an aseismic nucleation phase until the slip patch reaches a critical size [Dieterich, 1992; Rice, 1993], which may generate detectable signals. Recently, active measurements of reduction in seismic velocity, have been linked to pre-slip frictional weakening [Scuderi et al., 2016]. Similarly, permeability enhancement during nucleation, which is potentially driven by the same fundamental mechanism to frictional weakening [Segall and Rice, 1995; Samuelson et al., 2009] could be viewed as a sensitive precursor. This would require a sufficiently long duration of inter-seismic healing together with a pre-slip distance large enough and an observation wellbore sufficiently hydraulically well connected to the pre-slip fault plane. In the experimental results, we show that even one millimeter of slow-fault reactivation can result in a significant permeability enhancement.

Fracture permeability has been observed to be enhanced by transient stresses induced by distant earthquakes [Brodsky et al., 2003; Manga et al, 2012]. The behavior has been attributed to transient-flux-driven (sloshing) unclogging of colloidal seals [Brodsky et al., 2003; Elkhoury et al., 2011; Candela et al., 2014; Candela et al., 2015]. Our experiments suggest that remotely triggered seismicity (and therefore fault shear) [e.g. Hill et al., 1993; Van der Elst et al., 2013] should also be considered in explaining permeability enhancement. Transiting seismic waves from distant earthquakes will selectively reactivate the local fault patches that are near-critically stressed. The model can explain why the permeability response can be observed only in particular wellbores [e.g. Brodsky et al., 2003; Wang et al., 2016] since the response will be only significant for wellbores that are hydraulically connected to any reactivated fault patches. Further, earthquake induced hydraulic connection between vertically-stacked aquifers, observed by Wang et al. [2016], can be described by simply assuming that the reactivated fault transects the boundary between the two aquifers.

5. Conclusion

Our experiments demonstrate a cycle of the creation then destruction of permeability during laboratory slide-hold-slide experiments which substantially reproduce natural observations [Elkhoury et al., 2006]. We observe that both comminution and dilation can be driven by shear slip. The comminution effect is mostly dominant during initial shear-in on artificial fresh surfaces and for short healing/sealing periods – which may not be broadly representative of natural systems. Conversely, the effects of dilation become increasingly significant with the increased duration of healing – conditions much more representative of natural condition on faults subject to inter-seismic repose. During experimentally imposed periods of hold the permeability continuously declines, described by power law compaction and cubic law flow. Upon reactivation, the magnitude of permeability increase scales with an increase in repose period. Indeed, applying a substantial pre-reactivation repose period is essential to follow the correct path of permeability evolution present through the seismic cycle.

Supplementary Material

Table 3-1 List of experiments and experimental procedure.

Mode	Experiment	Rock Type	Abrasive Grit	Procedure
Single Long Hold	TKH1	WG	#150/#600	7mm initial slip – hold(~11hrs) – slip
	TKH2	WG	#150/#600	7mm initial slip – hold(~5hrs) – slip
	TKH3	WG	#150/#600	7mm initial slip – hold(~7hrs) – slip
	TKH5	WG	#150/#600	6mm initial slip – hold(~4hrs) – slip
	TKH9	WG	#600	3mm initial slip – hold(~22hrs) – slip
Slide-Hold-Slide	WG Rougher*)	WG	#150	Slip (2mm) – hold (10s) – slip (1mm) – hold (30s) – slip (1mm) – hold (100s) – slip (1mm) – hold (300s) – slip (1mm) – hold (1000s) – slip (1mm) – hold (3000s) – slip (1mm) – hold (10000s) – slip (1mm) - hold
	WG Smoother**)	WG	#600	
	GRS Rougher	GRS	#150	

*) 10000 s hold could not applied due to pump depletion

**) extra 5000 s hold applied after final slip

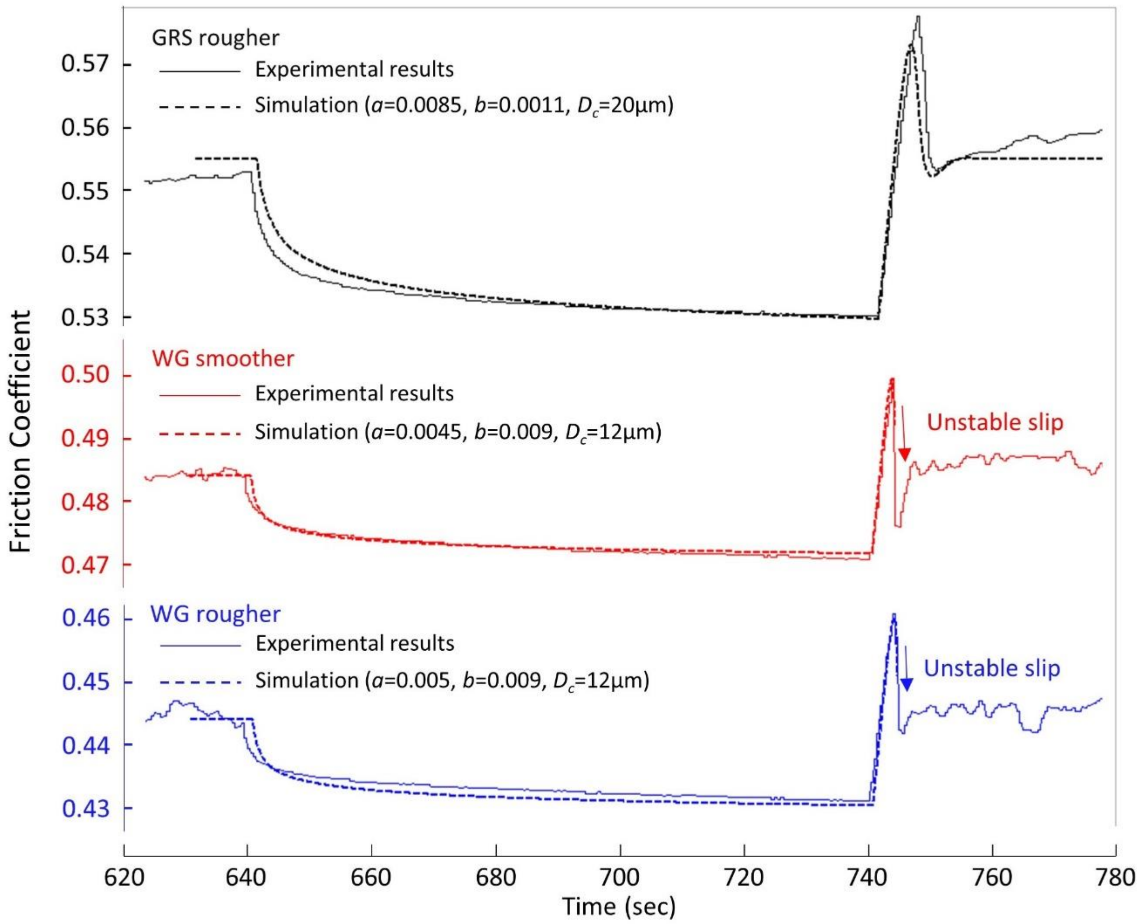

Figure 3-5 Zoomed-in views of friction response (solid lines) and rate and state model fits (dashed lines) of a single slide-hold-slide cycle (dashed box in Figure 3-2a). Rate and state simulations are conducted with a Ruina law and normalized stiffness, k/σ, 1000/m (where k is stiffness (Pa/m) and σ is normal stress (Pa)). The fitting parameters are shown in the figure. Westerly granite samples exhibit unstable stick-slip at the initiation of slips in both experiment and model. For the case of Westerly granite, the simulation is terminated during the acceleration stage since a quasi-static simulator is used.

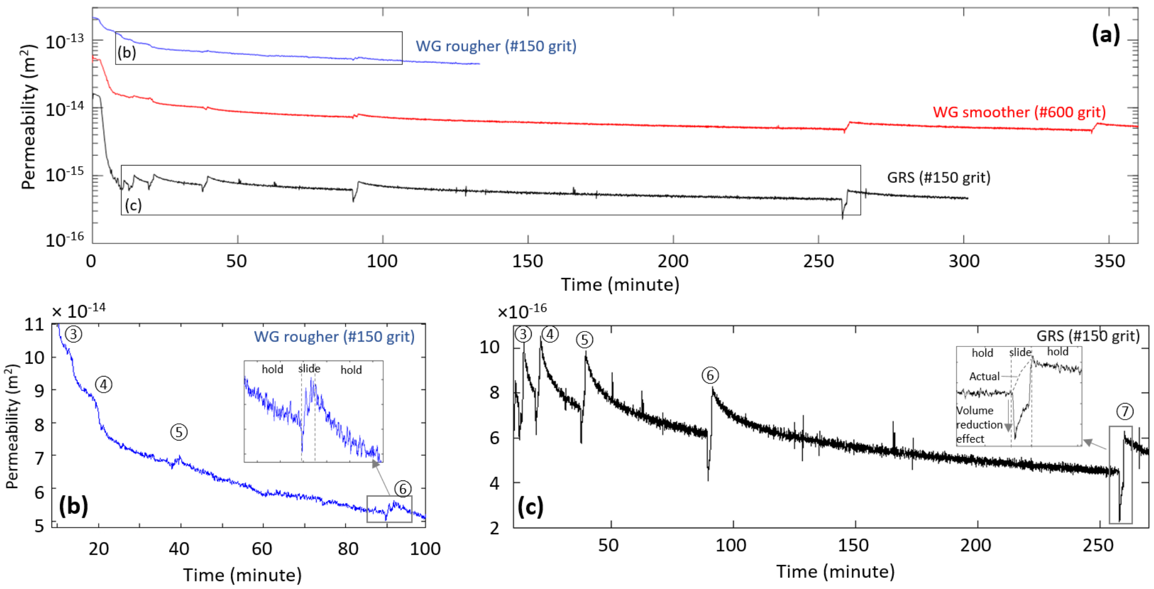

Figure 3-6 Permeability responses and zoomed-in view of WG rougher and GRS cases. Panels (b) and (c) are zoomed-in views corresponding to the box insert in panel (a). Single responses to sliding are highlighted in the small boxes in (b) and (c).

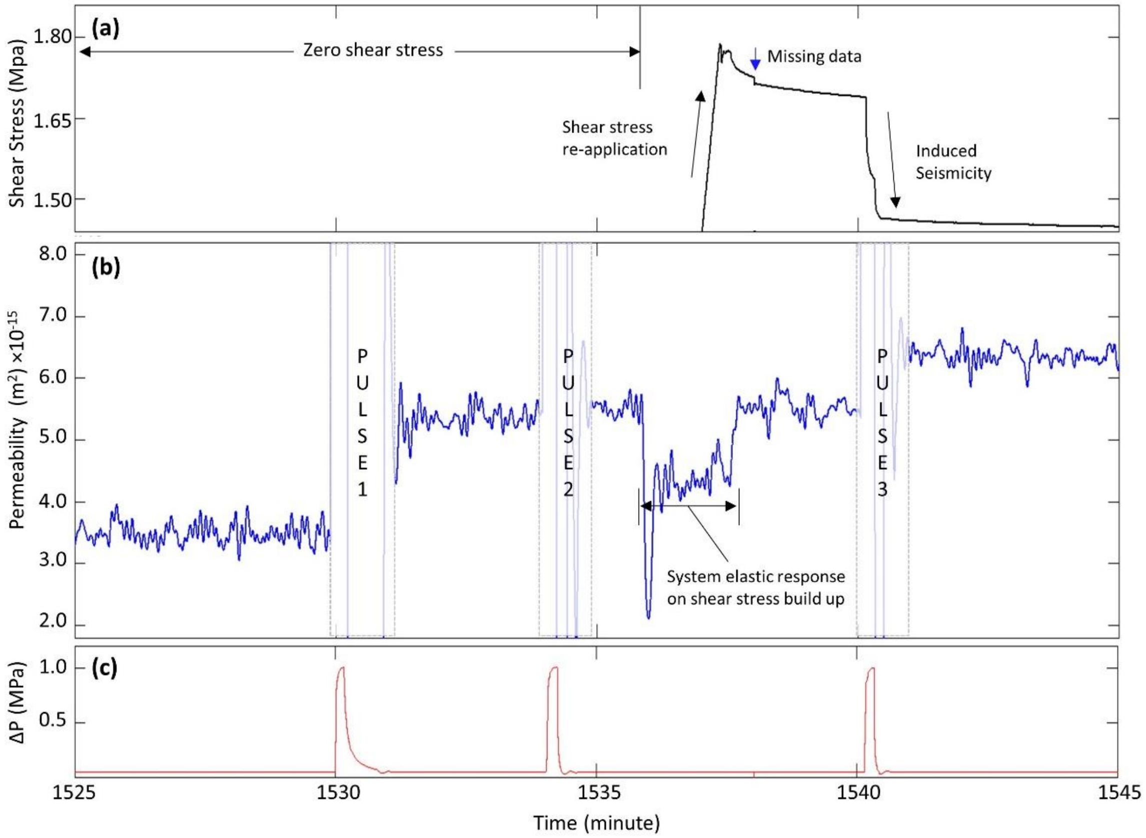

Figure 3-7 Permeability and shear stress response to three pore pressure pulses. Experiments are conducted after the application of a long hold period (~ 1 day). Presented in each panel are: (a): shear stress, (b) permeability and (c) pore pressure (pump C). Experiment is conducted with a constant pore pressure of 30kPa except for three applied pressure pulses at 1 MPa for a duration of 10 seconds. The first two pulses are applied with no applied shear stress to prevent the occurrence of shear slips. Conversely the third pressure pulse is applied after application of shear stress to generate an induced shear slip. Permeability significantly enhances with pulse 1, but no further enhancement is observed with pulse 2. Pulse 3 is associated with shear slip (see corresponding shear stress drop in (a)) and shows further permeability enhancement. Temporal permeability reduction ~1536 ~1537 minutes in panel (b) is an artifact of inlet chamber compaction (see main text) due to the application of shear stress. The discontinuity in panel (a) at ~ 1538 minutes (blue arrow) is due to lost data (this is not apparent in panel (b) since permeability is smoothed).

Acknowledgement

All experimental data are available as supporting information. This work is a partial result of support under projects DE-FE0023354. This support is gratefully acknowledged.

References

Brodsky, E.E., Roeloffs, E., Woodcock, D., Gall, I., and Manga, M., 2003, A mechanism for sustained groundwater pressure changes induced by distant earthquakes: J. Geophys. Res., v. 108, doi: 10.1029/2002JB002321.

Candela, T., Brodsky, E.E., Marone, C., and Elsworth, D., 2014, Laboratory evidence for particle mobilization as a mechanism for permeability enhancement via dynamic stressing: Earth and Planetary Science Letters, v. 392, p. 279–291, doi: 10.1016/j.epsl.2014.02.025.

Candela, T., Brodsky, E.E., Marone, C., and Elsworth, D., 2015, Flow rate dictates permeability enhancement during fluid pressure oscillations in laboratory experiments: J. Geophys. Res. Solid Earth, v. 120, p. 2037–2055, doi: 10.1002/2014JB011511.

Chen, J., Verberne, B.A., and Spiers, C.J., 2015, Interseismic re-strengthening and stabilization of carbonate faults by “non-Dieterich ” healing under hydrothermal conditions: Earth and Planetary Science Letters, v. 423, p. 1–12, doi: 10.1016/j.epsl.2015.03.044.

Chen, J., and Spiers, C., 2016, Rate and state frictional and healing behavior of carbonate fault gouge explained using microphysical model: J. Geophys. Res.: Solid Earth, v. 121, p. 8642–8665, doi: 10.1002/2016JB013470.

Dove, P. M., and D. A. Crerar, 1990, Kinetics of quartz dissolution in electrolyte solutions using a hydrothermal mixed flow reactor, Geochim.Cosmochim. Acta, 54, 955– 969.

Dieterich, J.H., 1992, Earthquake nucleation on faults with rate- and state-dependent strength: Tectonophysics, v. 211, p. 115–134.

Dieterich, J., and Kilgore, B., 1994, Direct Observation of Frictional Contacts: New Insights for State-dependent Properties: Pageoph, v. 143.

Elkhoury, J.E., Brodsky, E.E., and Agnew, D.C., 2006, Seismic waves increase permeability: Nature, v. 441, p. 1135–1138, doi: 10.1038/nature04798.

Elkhoury, J.E., Niemeijer, A., Brodsky, E.E., and Marone, C., 2011, Laboratory observations of permeability enhancement by fluid pressure oscillation of in situ fractured rock: J. Geophys. Res., v. 116, doi: 10.1029/2010JB007759.

Elsworth, D., and Goodman, R.E., 1986, Characterization of rock fissure hydraulic conductivity using idealized wall roughness profiles: int. J. Rock Mech. Min. Sci & Geomech., v. 23, p. 233–243.

Fang, Y., Elsworth, D., Wang, C., Ishibashi, T., and Fitts, J.P., 2017, Frictional stability-permeability relationships for fractures in shales: J. Geophys. Res. : Solid Earth, doi: 10.1002/2016JB013435.

Faoro, I., Niemeijer, A., Marone, C., and Elsworth, D., 2009, Influence of shear and deviatoric stress on the evolution of permeability in fractured rock: J. Geophys. Res. : Solid Earth, v. 114, p. 1–10, doi: 10.1029/2007JB005372.

Giger, S.B., Tenthorey, E., Cox, S.F., and Gerald, J.D.F., 2007, Permeability evolution in quartz fault gouges under hydrothermal conditions: J. Geophys. Res., v. 112, doi: 10.1029/2006JB004828.

Gratier, J.P., Renard, F., and Vial, B., 2014, Postseismic pressure solution creep: Evidence and time-dependent change from dynamic indenting experiments: J. Geophys. Res.: Solid Earth, v. 119, p. 2764–2779, doi: 10.1002/2013JB010768.

Guglielmi, Y., Cappa, F., Avouac, J., Henry, P., and Elsworth, D., 2015, Seismicity triggered by fluid injection – induced aseismic slip: Science, v. 348, p. 1224–1226.

Hill, D.P. et al., 1993, Seismiciy remotely triggered by the magnitude 7.3 Landers, California, earthquake: Science, v. 260, p. 1617–1623.

Hossain, M.M., Rahman, M.K., and Rahman, S.S., 2002, A Shear Dilation Stimulation Model for Production Enhancement From Naturally Fractured Reservoirs: SPE Journal,.

Ishibashi, T., Asanuma, H., Fang, Y., Wang, C., and Elsworth, D., 2016, Exploring the Link between Permeability and Strength Evolution during Fracture Shearing: Proceedings: 50th US Rock Mechanics / Geomechanics Symposium Houston, Texas,.

Lehner, F., 1995, A model for intergranular pressure solution in open systems: Tectonophysics, v. 245, p. 153–170.

Liu, J., Elsworth, D., Brady, B.H., and Muhlhaus, H.B., 2000, Strain-dependent Fluid Flow Defined Through Rock Mass Classification Schemes: Rock Mechanics and Rock Engineering, v. 33, p. 75–92.

Manga, M., Beresnev, I., Brodsky, E.E., Elkhoury, J.E., Elsworth, D., Ingebritsen, S.E., Mays, D.C., and Wang, C., 2012, Changes in Permeability Caused by Transient Stresses: Field Observations, Experiments and Mechanisms: Review of Geophysics, v. 50, doi: 10.1029/2011RG000382.

Manga, M., Brodsky, E.E., and Boone, M., 2003, Response of streamflow to multiple earthquakes: Geophys. Res. Lett , v. 30, doi: 10.1029/2002GL016618.

Marone, C., 1998, Laboratory-Derived Friction Laws and Their Application To Seismic Faulting: Annual Review of Earth and Planetary Sciences, v. 26, p. 643–696.

Mukuhira, Y., Moriya, H., Ito, T., Asanuma, H., and Haring, M., 2017, Pore pressure migration during hydraulic stimulation due to permeability enhancement by low-pressure subcritical fracture slip: Geophys. Res. Lett , v. 44, p. 3109–3118, doi: 10.1002/2017GL072809.

Niemeijer, A., Marone, C., and Elsworth, D., 2008, Healing of simulated fault gouges aided by pressure solution : Results from rock analogue experiments: J. Geophys. Res., v. 113, p. 1–15, doi: 10.1029/2007JB005376.

Niemeijer, A., Marone, C., and Elsworth, D., 2010, Frictional strength and strain weakening in simulated fault gouge : Competition between geometrical weakening and chemical strengthening: J. Geophys. Res., v. 115, doi: 10.1029/2009JB000838.

Ouyang, Z., and Elsworth, D., 1993, Evaluation of Groundwater Flow into Mined Panels: int. J. Rock Mech. Min. Sci & Geomech., p. 71–79.

Polak, A., Elsworth, D., Yasuhara, H., Grader, A.S., and Halleck, P.M., 2003, Permeability reduction of a natural fracture under net dissolution by hydrothermal fluids: Geophys. Res. Lett., v. 30, doi: 10.1029/2003GL017575.

Rice, J.R., 1993, Spatio-temporal Complexity of Slip on a Fault Rate- dependent friction: J. Geophys. Res., v. 98, p. 9885–9907.

Roeloffs, E.A., 1998, Persistent water level changes in a well near Parkfield , California , due to local and distant earthquakes: J. Geophys. Res., v. 103, p. 869–889, doi:10.1029/97JB02335

Roeloffs, E.A., 2006, Evidence for Aseismic Deformation Rate Changes Prior to Earthquakes: Annu. Re. Earth Planet. Sci, v. 34, p. 591–627, doi: 10.1146/annurev.earth.34.031405.124947.

Rojstaczer, S., and Stephen, W., 1992, Permeability changes associated with large earthquakes: An example from Loma Prieta, California: Geology, v. 20, p. 211–214.

Samuelson, J., Elsworth, D., and Marone, C., 2009, Shear-induced dilatancy of fluid-saturated faults: Experiment and theory: J. Geophys. Res., v. 114, doi: 10.1029/2008JB006273.

Scuderi, M.M., Marone, C., Tinti, E., Stefano, G. Di, and Collettini, C., 2016, Precursory changes in seismic velocity for the spectrum of earthquake failure modes: Nature Geoscience, v. 9, p. 695–700, doi: 10.1038/NGEO2775.

Segall, P., and Rice, J.R., 1995, Dilatancy , compaction , and slip instability of a fluid-infiltrated fault: J. Geophys. Res., v. 100, p. 155–171.

Tanikawa, W., Sakaguchi, M., Tadai, O., and Hirose, T., 2010, Influence of fault slip rate on shear - induced permeability: J. Geophys. Res.: Solid Earth, v. 115, p. 1–18, doi: 10.1029/2009JB007013.

Van der Elst, N., Savage, H., Keranen, K., and Abers, G., 2013, Enhanced Remote Earthquake Triggering at Fluid-Injection Sites in the Midwestern United States: Science, v. 341.

Wang, C.-Y., Liao, X., Wang, L.-P., Wang, C.-H., and Manga, M., 2016, Large earthquakes create vertical permeability by breaching aquitards: Water Resour. Res , p. 1–15, doi: 10.1002/2016WR018893.

Wang, C., and Manga, M., 2015, New streams and springs after the 2014 Mw6.0 South Napa earthquake: Nature Communications, v. 6, p. 1–6, doi: 10.1038/ncomms8597.

Wang, C., Elsworth, D., and Fang, Y., 2017, Influence of weakening minerals on ensemble strength and slip stability of faults: J. Geophys. Res. Solid Earth, v. 122, doi: 10.1002/2016JB013687.

Witherspoon, P., Wang, J., Iwai, K., and Gale, J., 1980, Validity of Cubic Law for Fluid Flow in a Deformable Rock Fracture: Water Resour. Res , v. 16, p. 1016–1024.

Xue, L., Li, H.-B., Brodsky, E.E., Xu, Z.-Q., Kano, Y., Wang, H., Mori, J.J., Si, J.-L., Pei, J.-L., Zhang, W., Yang, G., Sun, Z.-M., and Huang, Y., 2013, Continuous permeability measurements record healing inside the Wenchuan earthquake fault zone: Science, v. 340, p. 1555–1559, doi: 10.1126/science.1237237.

Yasuhara, H., and Elsworth, D., 2004, Evolution of permeability in a natural fracture : Significant role of pressure solution: J. Geophys. Res., v. 109, p. 1–11, doi: 10.1029/2003JB002663.

Yasuhara, H., and Elsworth, D. 2008, Compaction of a rock fracture moderated by competing roles of stress corrosion and pressure solution. Pure and Applied Geophysics, 165(7), 1289–1306. https://doi.org/10.1007/s00024-008-0356-2

Yasuhara, H., Elsworth, D., and Polak, A., 2003, A mechanistic model for compaction of granular aggregates moderated by pressure solution: J. Geophys. Res., v. 108, doi: 10.1029/2003JB002536.

Yasuhara, H., Polak, A., Mitani, Y., Grader, A. S., Halleck, P. M., & Elsworth, D., 2006, Evolution of fracture permeability through fluid-rock reaction under hydrothermal conditions. Earth and Planetary Science Letters, 244(1–2), 186–200. https://doi.org/10.1016/j.epsl.2006.01.046

Zhang, S., Tullis, T.E., and Scruggs, V.J., 1999, Permeability anisotropy and pressure dependency of permeability in experimentally sheared gouge materials: J. Struct. Geol., v. 21, p. 795–806.

Zoback, M.D., Kohli, A., Das, I., and McClure, M., 2012, The Importance of Slow Slip on Faults During Hydraulic Fracturing Stimulation of Shale Gas Reservoirs: SPE Journal, p. SPE 155476, doi: 10.2118/155476-MS.

Chapter 4

Cyclic Permeability Evolution during Repose then Reactivation of Fractures and Faults

Abstract

Cyclic growth and decay of permeability in fractures is explored during repeated reactivation and repose of saw-cut fractures of Green River shale. These slide-hold-slide experiments are constrained by measurements of fracture normal deformation and optical surface profilometry. Overall, we observe continuous permeability decay during repose periods (holds) and significant permeability enhancement during reactivation (slide). The permeability decay is accompanied by fault normal compaction. Both hydraulic aperture change (Δb_h) and measured compaction (Δb_s) are consistent with time dependent power law closure with a power exponent of ~0.2-0.4. These dual compaction magnitudes are positively correlated but $\Delta b_h > \Delta b_s$ in late stage holds. Permeability enhancement during shear reactivation is typically also accompanied by fault dilation. However, we also observe some cases where changes in hydraulic aperture and permeability decouple from the measured normal deformation, conceivably driven by mobilization of wear products and influenced by the development of flow bottlenecks. Pre- and post-test surface profiles show that the surface topography of the fractures is planed-down by shear removal. However, the flattened surfaces retain small scale roughness with mating and intergrowth anticipated to develop during the observed slow compaction. Flow simulations, constrained by the surface topography and measured deformation, indicate that small-scale roughness may control permeability at flow bottlenecks within a dominant flow channel. These results suggest cycles of permeability creation and destruction are an intrinsic component of the

natural hydraulic system present in faults and fractures and provide an improved mechanistic understanding of the evolution of permeability during fault repose and reactivation.

1. Introduction

Permeability evolution of fractures and faults is crucial in understanding the response of the natural hydraulic system to static and dynamic stress perturbations during the earthquake cycle [Brodsky et al., 2003; Elkhoury et al., 2006; Manga et al., 2003, 2012; Xue et al., 2013, Wang and Manga, 2015; Wang et al., 2016], and in the engineering of petroleum, geothermal and CO_2 sequestration reservoirs [Mukuhira et al., 2017; Zoback et al., 2012; Fang et al., 2017]. Fracture permeability is determined by size of pore throats [e.g. Witherspoon et al., 1980; Elsworth and Goodman, 1986] as well as the mobilization of fine gouge and wear products generated during dynamic shearing [Elkhoury et al., 2011; Candela et al., 2014, 2015]. Experimental observations show that shear slip applies two contrasting influences on fracture permeability. First, shear slip reduces contact asperity height by compaction, resulting in strong permeability reduction [e.g. Faoro et al., 2009; Zhang et al., 1999]. Second, shear slip can over-ride mated rough fracture surfaces, inducing shear dilation and resulting in permeability enhancement [e.g. Im et al., 2018]. These different modes of permeability evolution are likely controlled by roughness and matedness of the contacting fracture and the supply of wear products.

Roughness is one of the key factors that determines the dimensions of the pore space within the contacting fracture – larger pore throats will develop with the shear offset of rougher fractures. Natural faults exhibit scale-dependent roughness [Power et al., 1987; Candela et al., 2011; Renard and Candela, 2017] and shear slip will likely reduce surface roughness by brittle asperity comminution [Brodsky et al., 2011]. However, it is also reported that, even with laboratory prepared unmated surface, surface roughness can be increased by shear slip *via* grooving and slickensiding [Tesei et al., 2017].

For two surfaces in arbitrary (un-mated) contact, shear slip will potentially induce significant asperity comminution, compaction and therefore destroy permeability. However, if the two surfaces are well mated (interlocked) prior to shear offset, shear dilation [Junger and Tullis, 2003], even with significant comminution [e.g. Davidesko et al., 2014], may result with strong permeability enhancement. Highly mated and surface correlated natural faults are reported from facing surface profiling of the contacting hanging and foot walls [Power and Tullis, 1992]. This reasoning is consistent with studies of field scale fault reactivation that show gradual dilation at the onset of fault slip [Guglielmi et al., 2015].

Mechanisms of chemo-mechanical compaction, such as pressure solution, stress corrosion and mineral precipitation [Lehner, 1995; Yasuhara et al., 2003, 2004; Yasuhara and Elsworth 2008; Niemeijer et al., 2008] are all plausible mechanisms of inducing pre-slip asperity compaction of natural faults. Slow permeability reduction under static loading has been widely observed in both laboratory experiments [Polak et al., 2003, Giger et al., 2007; Yasuhara et al., 2006] and natural hydrological systems [Elkhoury et al., 2006; Xue et al., 2013]. Dissolution of asperities occurs over the microscopic contact and is not necessarily aligned with the mesoscale fracture orientation, thus solution driven compaction may enhance matedness of the contact.

Hence, short-term reactivations absent significant compaction or matedness may result in a reduction in permeability following reactivation and conversely, longer-term repose may result in fracture compaction and reactivation-related permeability increase [e,g, Im et al., 2018]. The following reports a systematic study of reactivation (slide) and repose (hold) via slide-hold-slide measurements to examine the influence of surface roughness and compaction on the evolution of fault permeability where normal deformations and the evolution of fracture topography are separately measured.

2. Experimental Method

We conduct fluid-flowthrough double-direct-shear experiments on fractures of Green River shale constrained by additional measurements of fracture normal displacement. A saw cut prismatic rock coupon (40.0mm × 25.2mm × 3.93mm) is sandwiched between two half-cylindrical core-plugs representing a dual fracture system – *i.e.* the two contact surfaces between the split cores and center block. The entire system is mechanically and hydraulically isolated by a latex jacket with normal stress applied to the exterior. Shear slip rate and an upstream fluid pressure are applied to the central coupon with permeability recorded by assumed steady state and Darcy's law. Shear displacement is measured *via* an LVDT (Linear Variable Differential Transformer) connected to loading piston.

Permeability (k) is calculated based on Darcy's law assuming steady state as,

$$k = \frac{\mu l}{A} \frac{(Q + whV)}{\Delta P} \tag{17}$$

where μ is fluid viscosity (8.9×10^{-4} Pa·s), l is flow path length (25mm), A is cross sectional area of the sample (core and center block) perpendicular to the flow path (4.71×10^{-4} m^2), Q is flow rate of Pump C, w is center block width (25.2mm), h is center block thickness (3.93 mm), V is slip velocity and ΔP is the pressure difference across the sample. The term whV in parentheses is a flow-rate correction for intrusion of the sample center block.

Evolution of fracture aperture, correlating with asperity height, can be estimated by converting the flowrate to an equivalent hydraulic aperture b_h of each fracture via the cubic law relation [Witherspoon et al., 1980]

$$\frac{Q+whV}{2}=\frac{{b_h}^3 w}{12\mu}\frac{\Delta P}{l} \tag{18}$$

where the notations are identical to equation (1). Note that equivalent flow rate ($Q + whV$) is halved since our experiment embeds two fractures. Accordingly, hydraulic aperture can be defined as,

$$b_h=\left(\frac{(Q+whV)}{2}\frac{l}{\Delta P}\frac{12\mu}{w}\right)^{\frac{1}{3}} . \tag{19}$$

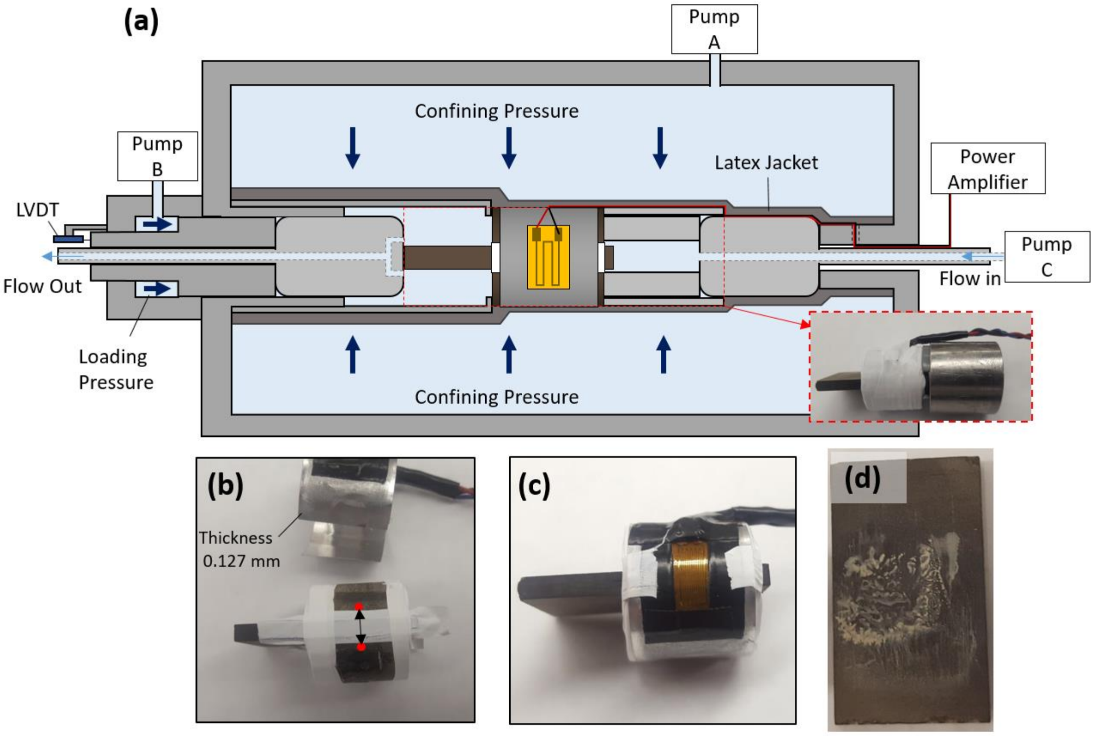

Figure 4-1 (a) Experimental configuration. (b) Green River shale sample before the strain gage assembly is added. Red dots represent fiducial locations for the measurement of cross-fracture displacement. (c) Sample with strain gage assembled. This is further wrapped with PTFE tape before final installation (see Figure 4-1a bottom right inset). (d) Condition of fracture surface post-experiment.

Fracture normal deformation is measured by the strain gage straddling the two fractures. The strain gage is attached on a thin (0.127 mm) aluminum shim and placed on the side of the center block (Figure 4-1b and c). The gage pattern fully covers the taped area with two anchoring points at the two ends (red dots marked in Figure 4-1(b)). The strain gage measures relative displacement of the two half-cylindrical cores during the test – hence the dilation of the two stacked fracture surfaces. We note that, in the slip phase, this relative displacement primarily measures thickness change of the center coupon. However, conversely, during hold, strain gage measurements directly represents change of fracture aperture (both fractures).

A reference length must be identified to convert measured strain to fracture normal displacement. Two potential endmember reference lengths may be defined. When the deformation occurs entirely within the pattern length of the strain gage (9.53 mm), then this pattern length can be used directly as a reference length. Conversely, if the deformation occurs over entire ring-shaped extent of the aluminum shim, the half circumference (~ 40mm) should be used as the reference length. The length of the shim contributing to the deformation can be estimated by force balance between the boundary force that drives the deformation of the shim (induced by compaction and dilation of the fracture), and the friction that resist that deformation. The force induced by fracture displacement δ over deformation length L is $F_s = Ew_a h\delta/L$ where E is the deformation modulus of aluminum, h is thickness of shim (0.127 mm) and w_a is the shim width. Conversely, the resisting frictional force is $F_f = \sigma\mu w_a L$ where σ is normal stress (3MPa) and μ is friction coefficient. Equating F_s and F_f gives estimated deformation length L *as*

$$L = \sqrt{\frac{Eh\delta}{\sigma\mu}}\ . \tag{20}$$

Substituting E = 69 GPa (aluminum), h = 0.127 mm, σ = 3MPa and assuming μ = 0.5 yields a deformation length L = 3.4 mm for a fracture normal displacement δ = 2 μm, implying that the few microns of repeated opening and compaction observed in this experiments (see Figure 4-5, following) likely occurs within the strain gage pattern area. Hence, in this work, we use the half of the pattern length as a reference length (“half” is used to measure single fracture normal displacement). However, we note that the large-scale compaction observed in the initial stage of the experiment may be underestimated since the deformation can extend beyond the strain gage pattern length.

We select apparently uniform surfaces of Green River shale. The surfaces are initially flattened by wet sending disk to achieve suitable flatness, and then ground with 60 grit aluminum oxide powder to create roughness. Green River shale is a clay poor brittle shale (carbonate ~ 52%, tectosilicate ~ 46%, and phyllosilicate ~2% [Fang et al., 2017]). Figure 4-2 shows an initial surface profile scanned by white light optical profilometry over a window 5.5 mm × 5.5 mm in dimension and with spatial resolution of 1.6μm. Vertical variations of the initial surface profile are mostly within ± 20 μm of the mean (see Figure 4-2a).

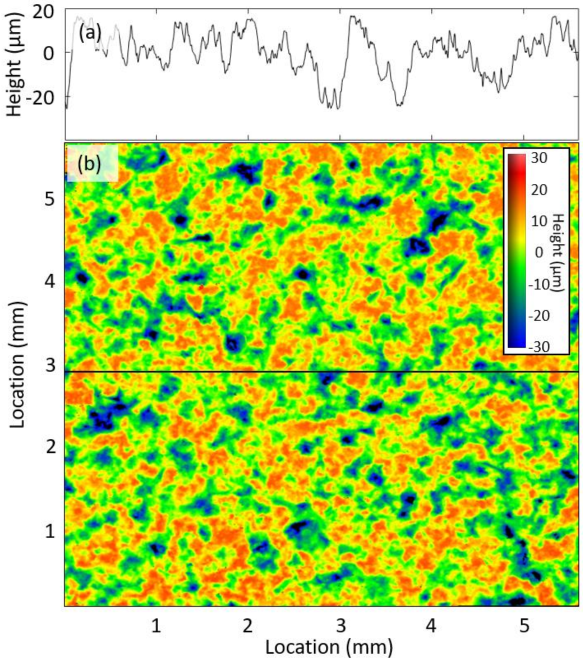

Figure 4-2 Initial surface profile pre-experiment. (a): cross section of aperture height (black line in (b)). (b): fracture surface topography within the scanned area.

We conduct four experiments on three different samples. Two experiments (KTS1 and KTS2) are conducted back-to-back with the same set of samples and the same configuration (initial position and shear direction). Surface wear products are washed off after KTS1 but no further surface grinding is conducted between the two experiments. Surface profiles are measured via optical profilometry before, in-between, and after these back-to-back experiments. Experiments are nominally designed to repeat 2 mm slips and 12 hour holds but are modified with due consideration of flowrate, pressure and remaining upstream reservoir volume (see Table 4-1 for detail). Loading rate for all shear slips is 10 μm/s.

Table 4-1 Experimental procedures of each experiments.

No.	Initial slip	Hold 1	Slip 1	Hold 2	Slip 2	Hold 3	Slip 3	Hold 4	Slip 4	Remarks
KTN1	2.5 mm	8 hr	1.5 mm	12 hr	2 mm	12 hr	2 mm	12 hr	2mm	
KTN2	5 mm	2 hr	1 mm	6 hr	2 mm	12 hr	2 mm	-	-	
KTS1	3 mm	8 hr	2 mm	12 hr	2 mm	12 hr	2 mm	-	-	Same sample Back-to-back Profile measured (fig. 4-7)
KTS2	3 mm	8 hr	2 mm	12 hr	2 mm	12 hr	2 mm	12 hr	2 mm	

3. Results

We explore cyclic permeability evolution during slide and then hold experiments on laboratory faults. The permeability evolution is converted into an equivalent hydraulic aperture and compared to the normal deformation directly measured by the straddling strain gage. We then explore the evolution of surface topography observed in back-to-back experiments. We use the measured surface topography to reconstruct fracture apertures and conduct flow simulations to analyze the characteristics of permeability structure in the fracture.

3.1. Permeability response

Figure 4-3b presents the evolution of permeability for the entire (~ 45 hours) duration of the tests. The permeability evolution clearly demonstrates cyclic destruction of permeability during the hold periods and enhancement during reactivations. During most of the holds, permeability continuously declines without any evidence of stabilizing to a steady-state. Conversely, during most of the reactivations, permeability significantly enhances. This cyclic destruction and enhancement of permeability becomes more evident with later sequences of holds-and-slips. For example, permeability response during the first slips at 8 h do not show significant permeability enhancement for all tests or even decrease for sample KTN1. However, the subsequent slips clearly and consistently enhance permeability.

Permeability response to initial shear slip is highlighted in Figure 4-3a, showing a strong destruction of permeability within a few millimeters of shear slip, in all cases (see Table 1 for initial slip distances). These strong destructive effects are consistent with previous observations [e.g. Im et al., 2018; Fang et al., 2017; Ishibashi et al., 2016] representing a strong shear driven comminution of fracture asperities on artificially prepared surface. The comminution is apparently reflected by the generation of wear products as shown in Figure 4-1d. The generation of wear products further suggests that the permeability decreases are not only caused by effects of aperture decrease but also by clogging by the fine wear products that clog the pore spaces.

Permeability continuously decreases during most of the holds. However, we observe one exception in experiment KTS1 in the initial 8-hour hold (dark red at 0~8 hour) as highlighted in Figure 4-3c. This shows permeability decline for the initial 5 hours but demonstrates occasional sudden fluctuations. These permeability fluctuations are initiated by adjustment of the pressure difference ΔP from 100 kPa to 200 kPa at 5 h. It is not surprising that the permeability is influenced by pore pressure perturbation [e.g. Candela et al., 2015]. But the permeability continues to occasionally fluctuate for the next ~2 hours where the pressure is maintained at a constant 200 kPa (circle highlighted in Figure 4-3c). During these fluctuations, only slight dilation is recorded upon application of the pressure change but no clear signal is observed over any of the subsequent permeability fluctuations, implying that this is a non-dilation related effect such as due to the intermittent transport of fine wear product and periodic clogging and unclogging. This reasoning is further supported by comparison with the result of KTS2. Experiments KTS1 and KTS2 are conducted sequentially with identical sample and experimental configurations. Therefore, the aperture height of KTS1 is unlikely to be smaller than KTS2. However, the permeability of KTS1 is significantly smaller than KTS2 during the initial hold (see Figure 4-3b initial 7 hours), implying that the dominant flow path is presumably clogged by wear products. Once the clogs appear to be have been removed at 7 hours, permeability of KTS1 never decreases below that of KTS2.

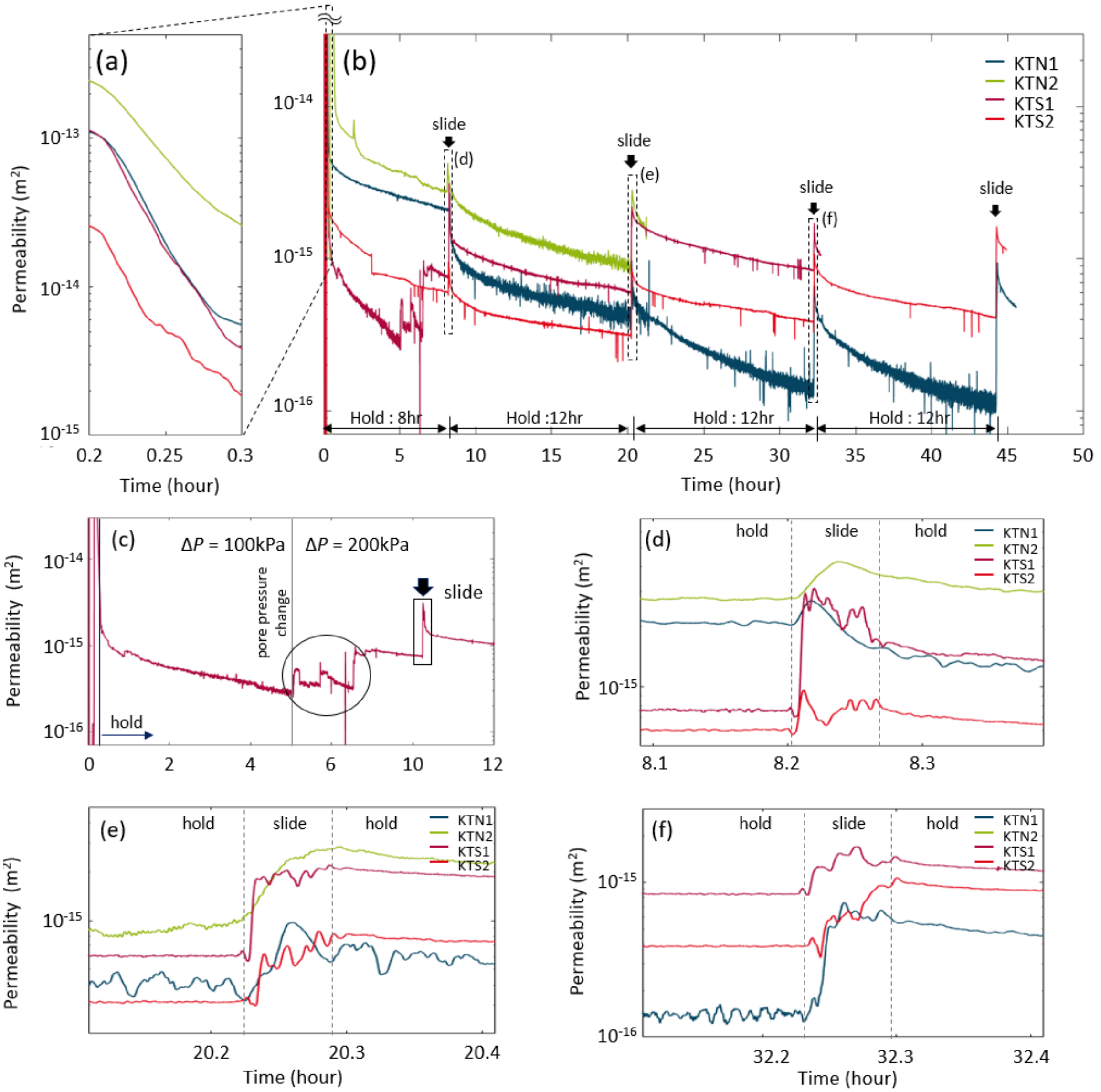

Figure 4-3 Permeability response to slide hold slide experiments (see Table 1 for detailed procedures for each experiment). (a) Permeability response to initial shearing-in; (b) Permeability response during the overall duration of the experiment (~45 hour); (c) Step permeability changes observed during experimental hold of KTS1; (d~f): Zoomed-in view of shear permeability responses marked at (b).

Permeability responses during slips are shown as zoomed-in plots in Figures 4-3d, e and f. During the slide phase, samples are sheared 2 mm at 10 μm/s with only a few exceptions (see Table 1). In all cases, permeability increases at the beginning of the slip.

However, the responses after this initial increase are varied and dissimilar. The first shear slips (Figure 4-3d) show that the permeability initially increases but soon begins to decrease as slip progresses. Conversely, permeability continues to increase with later stage slips (Figure 4-3f).

We use the cubic law to convert permeability into equivalent hydraulic apertures (equation 3) and to allow comparison with observed shear dilation as in Figure 4-4. These results show a few microns of hydraulic aperture change corresponding to cyclic permeability decay during holds (vertical decline) followed by permeability enhancement upon shear slip. Overall, the permeability response appears to be continuous (dashed lines) with troughs associated with hold. This behavior may be defined (dashed line in Figure 4-4) as a "dynamic" aperture which determines (hydraulic) aperture during shear slip. The dynamic aperture significantly declines upon initial shear slips (corresponding to Figure 4-3a), representing shear comminution and potential wear product clogging, and then, appears to stabilize as shear slip proceeds. During holds, as observed in Figure 4-3, the hydraulic aperture deviates from this dynamic aperture. However, when shear slip resumes, the hydraulic aperture recovers to the dynamic aperture and begins to repeat the same cycle. This observation clearly shows that the magnitude of shear permeability enhancement roughly scales to the magnitude of pre-slip compaction.

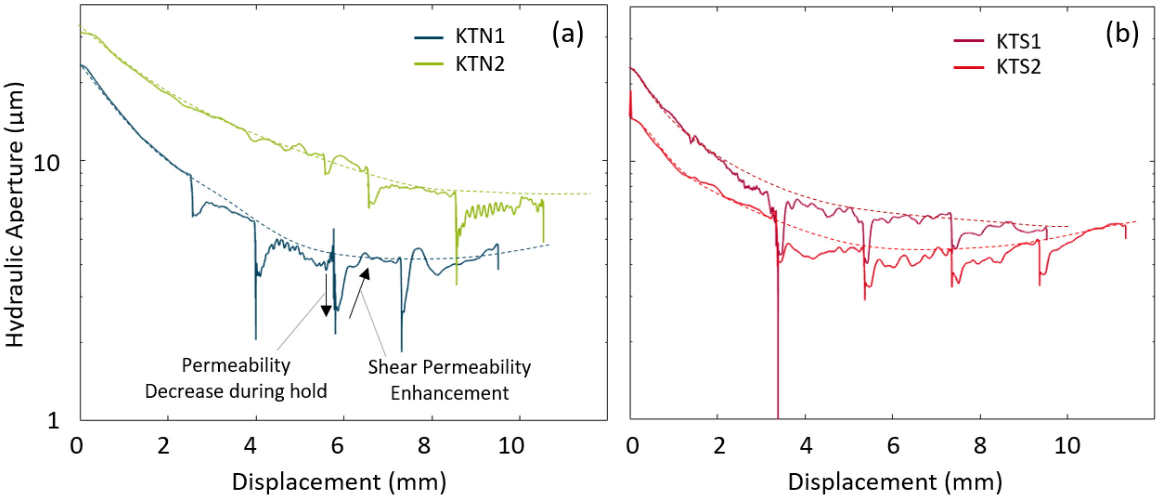

Figure 4-4 Evolution of hydraulic apertures calculated from the cubic law (equation 3) using the permeability data of Figure 4-3b.

3.2. Normal Deformation

Figure 4-5a shows the evolution of normal displacement (Δb_s). Since zero displacement ($\Delta b_s = 0$) is set at zero confining stress, strong compaction (15 ~ 50 μm) resulted in the initial stages of loading. The initial compaction results from (i) tightening of the grip between aluminum seat and the rock sample, (ii) fault compaction due to increased confining stress, and (iii) shear comminution with initial shear slip. KTS2 shows the smallest initial compactions as the experiment is conducted back-to-back after KTS1 and therefore its initial roughness is smaller than that of the other experiments. During holds, compactions are always observed - without exception. The magnitudes of the compactive events are typically less than a few microns and thus is of the same order as the observed and calculated changes in hydraulic apertures shown in Figure 4-4.

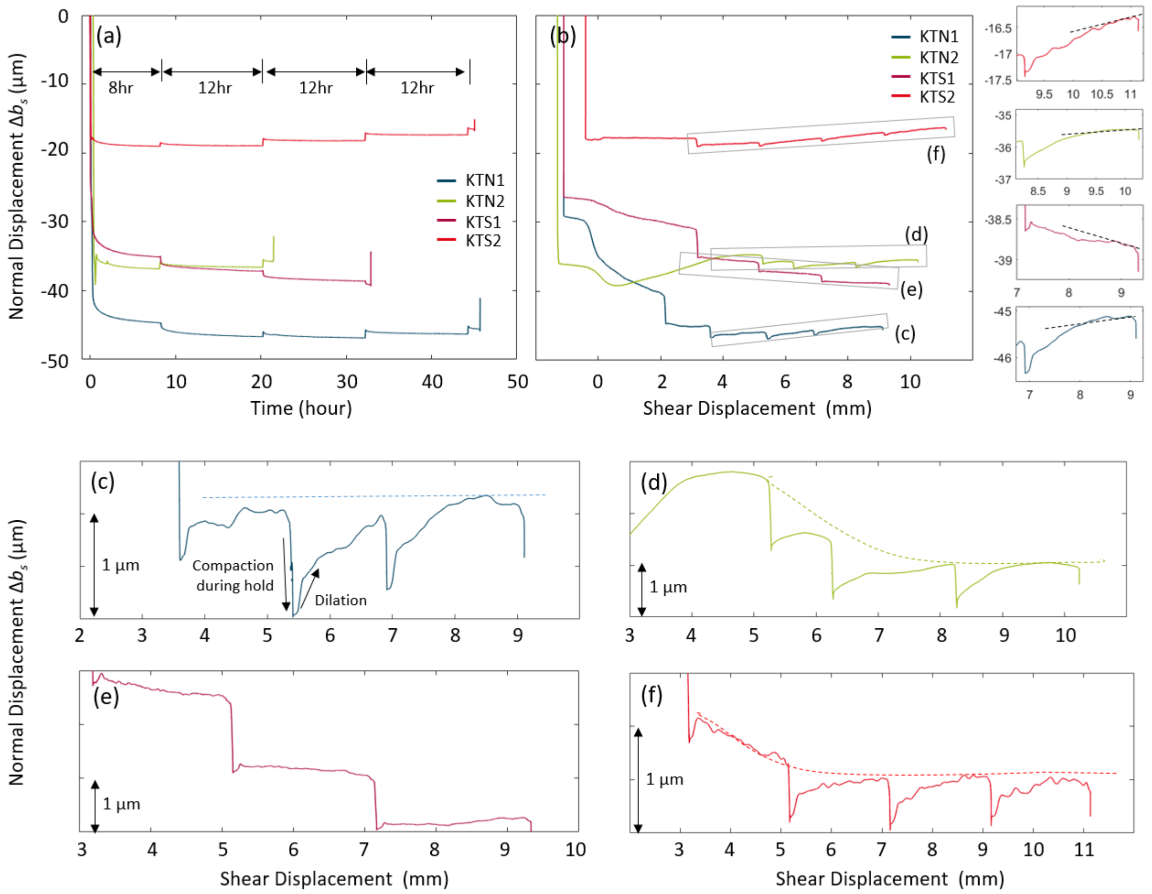

Figure 4-5 Normal deformations measured by circumferential strain gage (Δb_s), (a) and (b) show normal deformation with time then with shear displacement respectively, (c~f) zoomed-in view of normal displacement marked by rectangle in (b). The displacement in (c ~ f) are adjusted by the trend line shown on the right side of (b).

Figure 4-5b presents normal deformation with shear slip prior to detrending (identical results to Figure 4-2a). The initial strong compactions (vertical compactions) results from the application of confining stress. Over the following 2 mm slip, KTN1 and KTS1 show strong compaction which corresponds to permeability reductions (Figure 4-4). It is incongruous that the normal displacement of KTN 2 increases during the initial 2 mm of slip, and seemingly inconsistent with the initial permeability reductions. However, as noted before, the increase in the change in the normal displacement change here is likely an artifact that is induced by thickness change of a slightly tapered central rock coupon.

The normal deformation during shear slip should be detrended to estimate real aperture compaction/dilation. We use the later stage displacement as a reference trend (dashed lines on the right side of Figure 4-5b). Three of the detrended normal displacements (Figure 4-5 c,d and f) adequately represent the cyclic compaction during holds and shear induced dilation. The shear dilation during those experiments are initially rapid and slow over the later stages as similarly observed in the trend for hydraulic aperture (Figure 4-4) recovered from the permeability measurements. The exception to this behavior (Figure 4-5e) still shows compaction during the hold, but dilation is not apparent with slip. Moreover, the evolution of normal displacement in shown in Figure 4-5e is much flatter in time that the other cases. This observation may imply that the permeability enhancement is not solely dependent on aperture dilation. In fact, the magnitude of shear dilation observed in the other cases (Figure 4-5c, d & f) are also typically smaller than the hydraulic aperture changes (Figure 4-4).

3.3. Static Compaction

Figure 4-6 illustrates compaction measured by the strain gage (Δb_s, Figure 4-6a) and the evolution of hydraulic aperture change (Δb_h, Figure 4-6b) calculated from flowrate and the cubic law. Compaction evolves following a power law apparent from the near-linear plot in log-log space (Figures 4-6a&b). The power exponent (n) is uniformly of the order 0.2 ~ 0.4. Interestingly, this power law compaction rate is of similar range to that previously observed in solution-transport-driven indentation experiments [Gratier et al., 2014] and also observed for changes in hydraulic aperture on finely polished granite fractures [Im et al., 2018].

The magnitudes of the compactions in both cases are similar (0.5 ~ 4 microns), but not identical. Figure 4-6c compares the magnitudes of the two compactions at the end of holds, showing that the magnitude of the two compactions are positively correlated. However, generally, hydraulic aperture reductions (compactions, Δb_h) are larger than the strain gage measurements (Δb_s) with two exceptions on the initial holds (circles in Figure 4-6c). The two 4th holds (stars) show a change in hydraulic aperture that is more than two times larger than the measured compaction ($2\Delta b_s < \Delta b_h$). This behavior can be influenced by the artificial effect of deformation of the aluminum noted previously, or it could also be a real physical response where compaction does not proceed and related to permeability reduction due to, for example, mineral precipitation [Yasuhara et al., 2003, 2004].

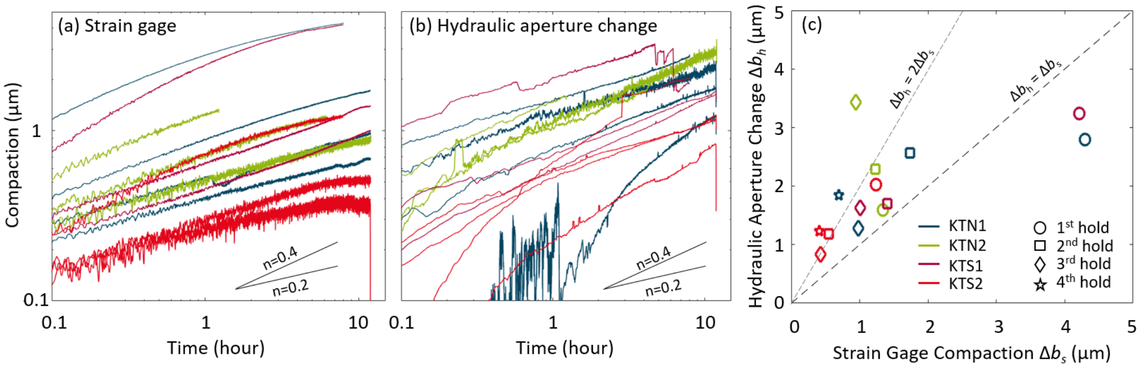

Figure 4-6 Compactions during holds observed *via* (a) Direct measurement by strain gage, Δb_s and (b) Equivalent hydraulic aperture calculated from the cubic law, Δb_h; (c) Comparison of the magnitude of final compactions between Δb_s and Δb_h.

3.4. Surface Profile

Three consecutive surface scans are conducted on two back-to-back experiments (KTS1 and KTS2) (Figure 4-7). We observe strong comminution and flattening during the first experiment with a rough surface. Comparison between Figures 4-7a and b indicate that the peaks of the fresh initial surfaces (Figure 4-7a) are planed-flatter after the experiment (Figure 4-7b). This significant comminution is apparent from the histogram of the surface scans (Figure 4-7d). Roughly 10 µm of asperity height is removed from initial state (black). The magnitude of the comminution is large in the first experiment (KTS1) but is significantly reduced for the second experiment (KTS2).

Figures 4-7e and 7f compare cross-sectional profiles of the initial rough surface (gray), after the first (KTS1; red) and second (KTS2; blue) experiments, aligned both along the slip direction (Figure 4-7e) and perpendicular to the slip direction (Figure 4-7f). Note that the red and blue curves represent identical surface locations on the sample. The observed roughness of the curves appear similar, but aperture height of the blue profile (before KTS2) is slightly smaller than that for the red profile (after KTS2) as similarly observed in the histogram in Figure 4-7d. Overall, the comminution effect between the two appears to be within a few microns which corresponds to the hydraulic aperture difference of KTS1 and KTS2 shown in Figure 4-4b.

Major troughs on these surfaces (i.e. high permeability zones) are developed during initial surface grinding using rough (60 grit) abrasives. However, we also observe a smaller scale, of the order of a few microns, roughness developed on the top of the planed surface. Apparently, major flow channels develop by connecting the initially disjointed major troughs. If the major troughs are well connected, permeability of this system will be dominated by these deep troughs. Conversely, if these troughs do not become well connected (for example by shear flattening and chemo-mechanical compaction) fluid must be transported only through the small scale roughness that acts as bottlenecks to the major flow channels. In this case, the overall permeability is controlled by the permeability of the bottleneck. To address this complex permeability structure, we conduct flow simulations using the surface profiles.

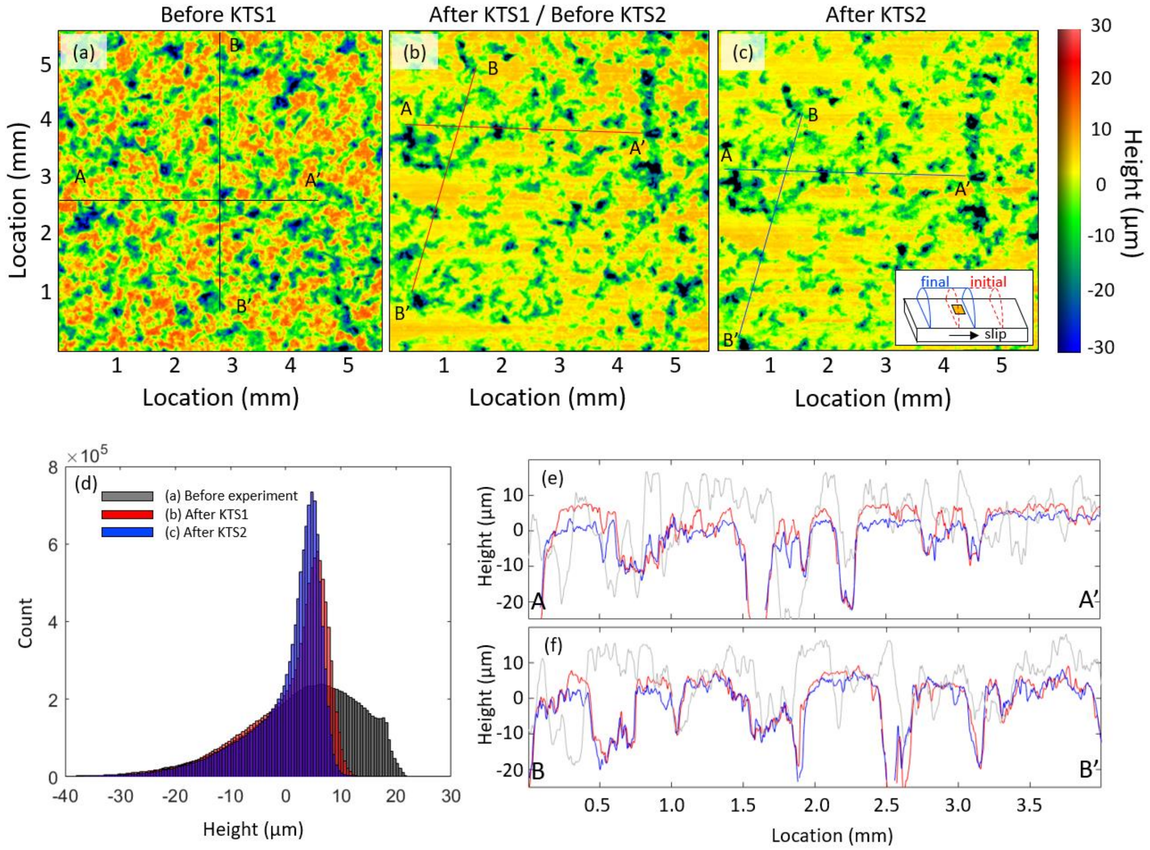

Figure 4-7 Surface profilometry measured consecutively over two back-to-back experiments, KTS1 and KTS2: (a) Initial laboratory surface (before KTS1), (b) Surface profile after first experiment and (c) Surface profile after second experiment. Note that (b) and (c) are roughly identical locations on the surface while (a) is at different locations. (d): Histograms of surface heights. The x-axes of the initial surfaces are adjusted to exhibit similar tails (negative heights) to compare the effects comminution directly. (e & f): Cross section of surface profile. Location and color corresponds to the lines shown in (a~c). Red and blue profiles show identical locations in the sample both before and after the second experiment while gray is at a different location.

3.5. Flow simulation

We use the surface profile data in Figure 4-7b for the flow simulation. To reduce the computational load, 20 × 20 pixels (1 pixel ~ 1.6 µm × 1.6 µm) are combined into a single node. We assume that the facing fracture is flat which may lead to an underestimation of permeability. We do not consider other factors that reduce permeability such as, the presence of wear products and elastic compaction due to normal stress. Aperture (Figure 4-8a) is directly converted from the surface scan data (Figure 4-7b). Fluid flows horizontally across the fracture domain between opposite pressure boundaries transiting from 50 kPa and 0 kPa on left and right sides of the fracture and with no flow boundaries at top and bottom. The pressure difference (50 kPa over 5.5 mm flow) is scaled relative to the full fracture size (200 kPa for 25 mm flow). We calculate steady state flowrate from the cubic law (equation 2) at each node. To analyze the permeability response to the compactions, the aperture is reduced by 4 different magnitudes: 0, 2, 3 and 4 µm. Figure 4-8b shows the cross sectional profiles (color profiles correspond to lines in Figure 4-8a) with the level of the applied compactions (dashed lines). To avoid a singularity in the numerical solutions, a 1 nm aperture height is assigned on nominally contacting surfaces.

Simulation results (Figure 4-8 c~f) illustrate the development of channels with increased fracture compaction. Initially, diverse channels are developed on the non-compacted surface (Figure 4-8c) but as compaction proceeds, a few major channels dominate in carrying the overall flow rate (Figure 4-8f). The channels develop by connecting major troughs created during the initial surface grinding. The red dashed line in Figure 4-8a represents one of the major flow channels developed after 4 µm compaction (red dashed line in Figure 4-8f). Apparently, the flow channel develops by connecting major troughs, showing that the distribution of troughs is important in defining permeability of the fault.

To estimate the hydraulic aperture of system, total flow rate to the outflow boundary is converted into an hydraulic aperture (b_h) using a cubic law and presented in Figures 4-8c, d, e and f (bottom left). The magnitude of flow rate roughly corresponds to the hydraulic apertures observed in our experiments (Figure 4-4). Hydraulic compaction is slightly larger than the applied compaction. For example, a total compaction of 4 μm yields 4.56 μm of hydraulic compaction (from 8.4 μm to 3.84 μm; Figure 4-8 c to f). This may result from the spatial closing of fluid channels and partly explains the observation that hydraulic compaction is generally larger than normal displacement (Figure 4-6).

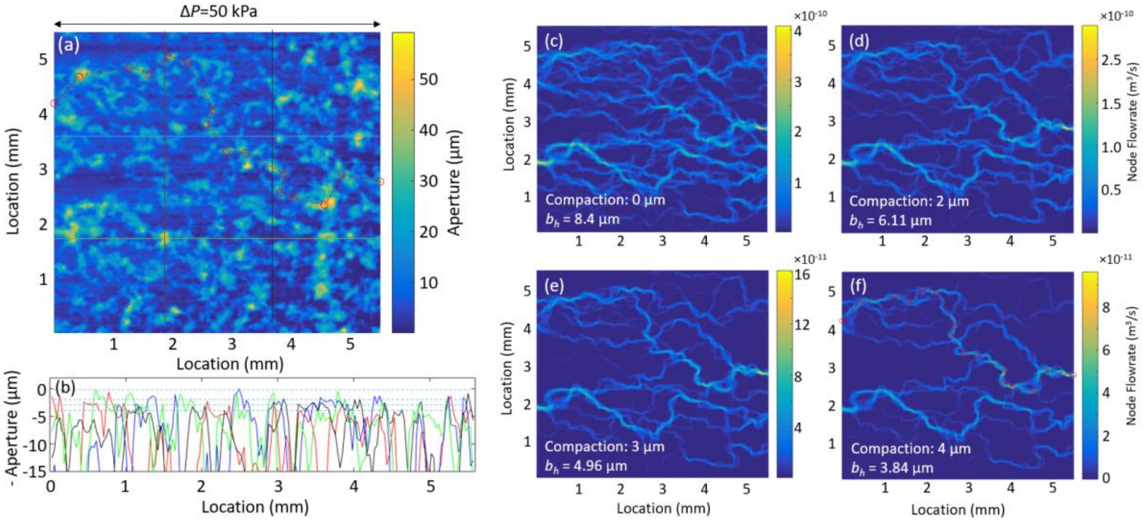

Figure 4-8 (a): Aperture heights of a non-compacted surface constructed from the surface profile of Figure 4-7b. (b): Cross sections of aperture heights with color corresponding to the line in (a). Dashed horizontal lines show the level of compaction applied for the simulation results. (c ~ f): Simulation results. Applied compactions and resulting equivalent hydraulic aperture is presented to the bottom left of each result. Red dashed lines in (a) and (f) indicate the same locations showing major flow channel developing by the connecting of the major previously-disconnected surface troughs.

Figure 4-9 shows the pressure distribution along the major flow channel (red dashed line in Figures 4-8a&f and 9 inset) at 4 μm compaction (Figure 4-8f). The pressure distribution illustrates occasional step-like pressure drops, implying that the flowrate is controlled by several low permeability-zone bottlenecks. For example, ~30% of the total pressure drop occurs at only one bottleneck (red arrows). This result shows that the permeability of the overall fracture system is effectively controlled by the aperture at the bottleneck developed over a major flow path.

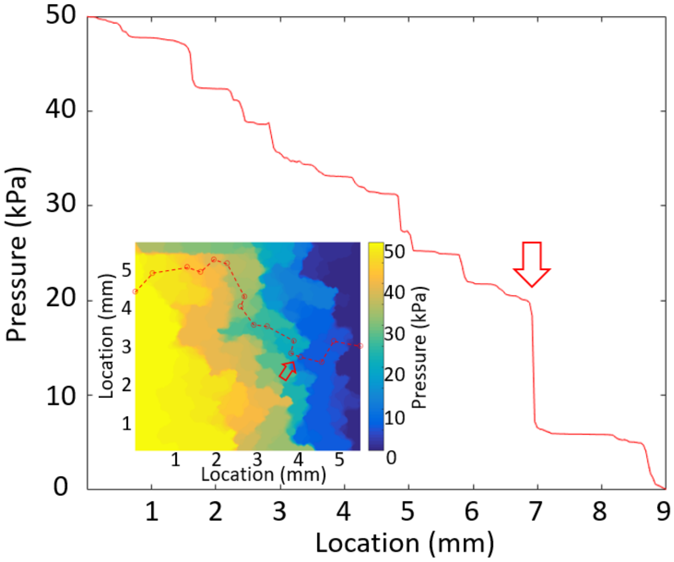

Figure 4-9 Pressure together with major flow channels at 4 μm compaction (red dashed line in inset and Figures 4-8a&f). Inset: pressure distribution of the simulation result. Red arrow corresponds to the location of the red arrow in the inset.

4. Discussion

Our experiments replicate, in real-time, cycles of slow permeability reduction and earthquake-induced permeability enhancement observed in nature [Elkhoury et al., 2006; Xue et al., 2013]. Permeability decline and enhancement are associated with fault compaction and dilation. However, the measured compaction and hydraulic aperture change are not completely coupled. Here we discuss possible mechanisms of the permeability changes.

4.1 Permeability decay, compaction and matedness

We show that the sealing is accompanied by aperture compaction. Compaction both directly measured by strain gage and inferred/calculated from flow rates track together and follow power law decay with a power exponent of ~0.2-0.4. The slow and continuous process of compaction implies that it is likely a result of chemo-mechanical process such as pressure solution, stress corrosion and mineral precipitation [Lehner, 1995; Yasuhara et al., 2003, 2004; Yasuhara and Elsworth 2008]. Such power law compaction is consistent with similarly observed solution-driven intrusion of a stressed rigid indenter [Gratier et al., 2014].

Measured compaction (Δb_s) and hydraulic aperture change (Δb_h) are similar in magnitude at ~0.5-4 µm during ~8-12 hours of hold. The two compactions show strong positive correlations, but their magnitudes are not identical. Generally, the hydraulic compaction Δb_h appears to be larger than the mechanical compaction Δb_s except for the first two hold cases (Figure 4-6). We note that this behavior ($\Delta b_h > \Delta b_s$) can be an artifact due to deformation of the aluminum sheath extending beyond the extent of the strain gage pattern. Separate from this artifact, there are several plausible mechanisms that can explain such behavior. Spatial closing of flow path is one possibility as observed in the results of flow simulation (Figure 4-8). Also, mineral precipitation is another candidate as it can significantly reduce permeability without the need for mechanical compaction [Yasuhara et al., 2003, 2004]. The opposite behavior ($\Delta b_h < \Delta b_s$) is only observed during the first holds, where the flow rate is relatively larger than the other cases and therefore the influence of mineral precipitation is likely smaller and particle mobility of fine wear products is higher.

Since the compaction may be driven by mineral dissolution over the microscopic contact, which is not necessarily aligned with the mesoscale fracture orientation, it may lead to an increase in the matedness of the fault. Figure 4-10 illustrates hypothetical compaction processes using two 1 mm lengths of the surface profiles shown in Figure 4-7b. The two profiles of the upper and lower surfaces are taken from the planed-down surface along slip direction (blue lines in Figure 4-10a). The surface profiles (e.g. Figure 4-10b) show that micro scale roughness exists even on these planed-down surfaces. This small scale roughness is also observed and shown to be independent of the slip directions [Candela and Brodsky 2016]. Assuming that mineral dissolution rates are identical between the upper and lower surfaces, Figure 4-10 shows that significant mating can result from the magnitude of compaction we observe in our experiments (~1-2 μm). As dissolution proceeds (Figure 4-10 b → c → d), real area of contact (red) increases. Since the microscopic real contact is not parallel to the mesoscale contact surface, the compaction process increases matedness. Figure 4-10d illustrates this strongly mated hypothetical contact.

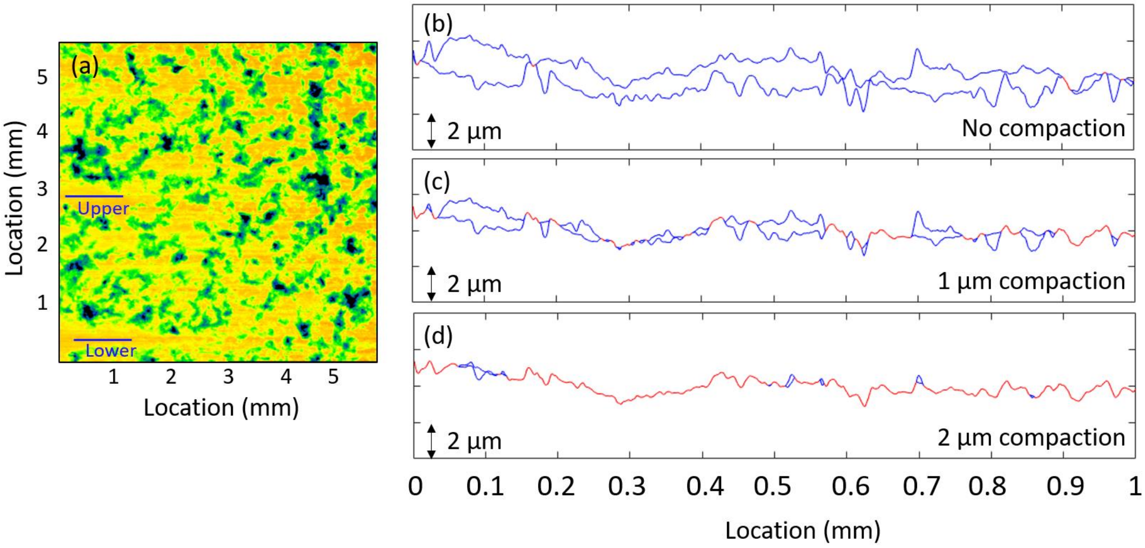

Figure 4-10 Hypothetical compaction of fine-scale roughness developed on the sheared surface. (a) Surface profile (identical to Figure 4-7b). (b ~ d) Hypothetical compaction driven by mineral dissolution at the real contact (red). The surface is taken from the flattened surface shown in (a). Identical dissolution rate on upper and lower surfaces is assumed.

4.2 Mechanism of permeability enhancement

Permeability response to shear slip is controlled by pre-slip sealing [Im et al., 2018]. If shear slip is applied on the unsealed surface (e.g. Figure 4-10b), significant comminution and consequent permeability destruction will occur. This explains the initial shear-driven strong permeability reduction on fresh surfaces (Figure 4-3a). Conversely, if shear slip is applied on the surface which has been strongly sealed as shown in Figure 4-10d, the established seal may be breached by shear slip and accordingly induce permeability enhancement.

Most of the shear permeability enhancements are associated with dilation - in these experiments. However, we also observe some behaviors that are different from this norm where the permeability enhancement are not well coupled with aperture changes in experiment KTS1 (Figure 4-5e). This experiment (KTS1) demonstrates sudden permeability fluctuations presumably driven by particle mobilization (Figure 4-3c). Interestingly, permeability enhancement with shear slip in KTS1 similarly appears as a step increase at the initiation of shear deformation (Figure 4-11a; also Figure 4-3&4), implying that such particle mobilization may also be triggered by the initiation of shear slip. Throughout all experiments, we observe two significantly different permeability enhancement behaviors with shear slip: (i) sudden permeability enhancement at the initiation of shear slip (Figure 4-11a) and (ii) gradual and continuous permeability enhancement with shear slip (Figure 4-11b). The sudden permeability enhancements are often shown in earlier stage slips. Conversely, gradual displacement-dependent permeability enhancement is more general in later slips (comparing Figures 4-3d and f). The result implies that particle mobilization and unclogging may also be triggered by shear slip and contribute to the shear permeability enhancement process.

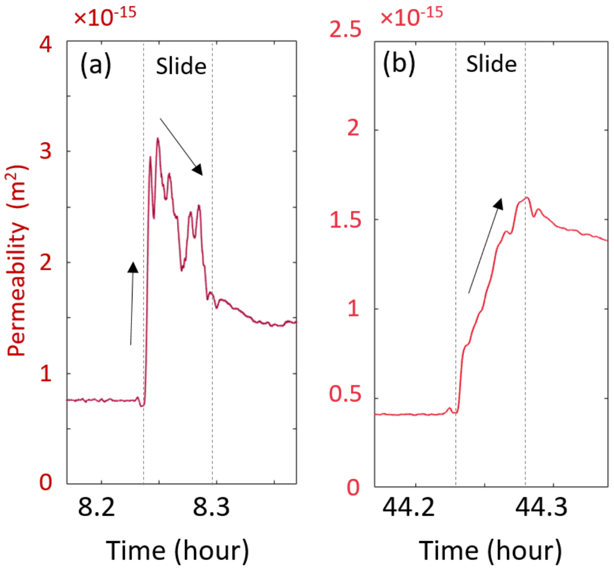

Figure 4-11 Two different permeability evolution behaviors. (a) Significant initial permeability increase than gradual decrease (KTS1 first slip). (b) Gradual permeability increase with shear slip (KTS2 4th slip).

4.3. Implications for natural systems

Our experiments on laboratory faults substantially replicate permeability cycles observed in nature – albeit at different timescales. We observe that shear permeability enhancement requires pre-slip sealing. Indeed, gradual permeability decay of the natural hydraulic system during the inter-seismic period is a well-documented phenomenon [Elkhoury et al., 2006; Xue et al., 2013; Wang et al., 2016]. The slow and gradual nature of the permeability evolution behavior implies that the sealing may be driven by chemo-mechanical processes such as pressure solution and stress corrosion [Yasuhara et al., 2003, 2004; Yasuhara and Elsworth 2008]. Since mineral dissolution rate is significantly dependent on temperature and applied stress [Dove and Crerar, 1990], compaction of natural faults during the inter-seismic period should be more significant than in our experiments due to higher temperatures, larger normal stresses and longer duration in nature. Accordingly, the contacting surfaces are likely strongly mated in their natural state. Indeed, highly mated natural faults are reported from profiling of opposing surfaces [Power and Tullis, 1992].

Shear slip on the strongly mated contact will breach the interlocking of the surfaces and induce dilation. Therefore, the co-seismic permeability enhancement observed in nature can be significantly contributed to by shear breaching and dilation of the sealed/mated surface. This mechanism further suggests that remotely triggered seismicity (fault shear) [e.g., Hill et al., 1993; Van der Elst et al., 2013] could be considered in explaining the permeability enhancement induced by distant earthquakes [Brodsky et al., 2003; Manga et al., 2012] in addition to the existing explanation – flux driven unclogging of colloidal seals [Brodsky et al., 2003; Elkhoury et al., 2011; Candela et al., 2014, 2015], which is also presumed in our experiment.

5. Conclusion

We observe cycles of permeability creation and destruction during slide-hold-slide experiments with measurements of fault normal deformation *via* a strain gage. The experimental results demonstrate that permeability response to shear slip is controlled by pre-slip sealing. During hold periods, normal deformation and hydraulic aperture compaction follow power law decay with a power exponent of ~ 0.2-0.4. The magnitude of the two (hydraulic and mechanically measured) compactions show a strong positive correlation but are not identical. Generally, hydraulic aperture decline is larger than the measured compaction with two exceptions at first holds. Shear permeability enhancements are also accompanied by shear dilation but again with some exceptions. Those observations imply that permeability cycles observed during fault repose and reactivation are controlled by chemo-mechanical compaction and mated surface dilation. However, there are more factors which can contribute to the complex behavior, such as mobilization of wear products.

Surface profile scans post-experiment show significant comminution during the experiments. This observation explains the strong permeability reduction observed during the initial shear-in of fresh laboratory prepared surfaces. The comminution effect is significantly reduced when the sample is reused for a back-to-back test. Micro scale roughness is developed on the top of the planed surface. We note that the magnitude of compaction observed in the experiment (a few microns) may increases the matedness of those micro-roughness contacts. If the mated contacts behave as a bottleneck on major flow paths, they can control overall permeability. Breaching the mated seal *via* shear slip can significantly enhance permeability.

Acknowledgement

All experimental data are available as supporting information. This work is a partial result of support under projects DE-FE0023354. This support is gratefully acknowledged.

References

Brodsky, E. E., Gilchrist, J. J., Sagy, A., & Collettini, C. (2011). Faults smooth gradually as a function of slip. Earth and Planetary Science Letters, 302(1–2), 185–193. https://doi.org/10.1016/j.epsl.2010.12.010

Brodsky, E.E., Roeloffs, E., Woodcock, D., Gall, I., and Manga, M., 2003, A mechanism for sustained groundwater pressure changes induced by distant earthquakes: J. Geophys. Res., v. 108, doi: 10.1029/2002JB002321.

Candela, T., & Brodsky, E. E., 2016, The minimum scale of grooving on faults. Geology, 44(8), 603–606. https://doi.org/10.1130/G37934.1

Candela, T., Brodsky, E.E., Marone, C., and Elsworth, D., 2014, Laboratory evidence for particle mobilization as a mechanism for permeability enhancement via dynamic stressing: Earth and Planetary Science Letters, v. 392, p. 279–291, doi: 10.1016/j.epsl.2014.02.025.

Candela, T., Brodsky, E.E., Marone, C., and Elsworth, D., 2015, Flow rate dictates permeability enhancement during fluid pressure oscillations in laboratory experiments: J. Geophys. Res. Solid Earth, v. 120, p. 2037–2055, doi: 10.1002/2014JB011511.

Candela, T., Renard, F., Bouchon, M., Schmittbuhl, J., and Brodsky, E. E., 2011, Stress drop during earthquakes: Effect of fault roughness scaling. Bulletin of the Seismological Society of America, 101(5), 2369–2387. doi:10.1785/0120100298

Davidesko, G., Sagy, A., & Hatzor, Y. H., 2014,. Evolution of slip surface roughness through shear. Geophysical Research Letters, 41, 1492–1498. https://doi.org/10.1002/ 2013GL058913

Dove, P. M., & Crerar, D. A., 1990,. Kinetics of quartz dissolution in electrolyte solutions using a hydrothermal mixed flow reactor. Geochimica et Cosmochimica Acta, 54(4), 955–969. https://doi.org/10.1016/0016-7037(90)90431-J

Elkhoury, J.E., Brodsky, E.E., and Agnew, D.C., 2006, Seismic waves increase permeability: Nature, v. 441, p. 1135–1138, doi: 10.1038/nature04798.

Elkhoury, J.E., Niemeijer, A., Brodsky, E.E., and Marone, C., 2011, Laboratory observations of permeability enhancement by fluid pressure oscillation of in situ fractured rock: J. Geophys. Res., v. 116, doi: 10.1029/2010JB007759.

Elsworth, D., & Goodman, R. . , 1986, Characterization of rock fissure hydraulic conductivity using idealized wall roughness profiles.pdf. Int. J. Rock Mech. Min. Sci., 23(3), 233–243.

Fang, Y., Elsworth, D., Wang, C., Ishibashi, T., and Fitts, J.P., 2017, Frictional stability-permeability relationships for fractures in shales: J. Geophys. Res. : Solid Earth, doi: 10.1002/2016JB013435.

Giger, S.B., Tenthorey, E., Cox, S.F., and Gerald, J.D.F., 2007, Permeability evolution in quartz fault gouges under hydrothermal conditions: J. Geophys. Res., v. 112, doi: 10.1029/2006JB004828.

Hill, D. P. et al., 1993, Seismiciy remotely triggered by the magnitude 7.3 Landers, California, earthquake. Science, 260, 1617–1623.

Im, K., Elsworth, D., and Fang, Y., 2018, The influence of preslip sealing on the permeability evolution of fractures and faults. Geophysical Research Letters, 45. https://doi.org/10.1002/2017GL076216

Ishibashi, T., Asanuma, H., Fang, Y., Wang, C., and Elsworth, D., 2016, Exploring the Link between Permeability and Strength Evolution during Fracture Shearing: Proceedings: 50th US Rock Mechanics / Geomechanics Symposium Houston, Texas,

Junger, J.A., and T.E. Tullis. 2003. Fault roughness and matedness suggest significant fault-interface dilatancy with slip. EOS Trans. Am. Geophys. Union: Abstr. S51B-03.

Lehner, F., 1995, A model for intergranular pressure solution in open systems: Tectonophysics, v. 245, p. 153–170.

Manga, M., Beresnev, I., Brodsky, E.E., Elkhoury, J.E., Elsworth, D., Ingebritsen, S.E., Mays, D.C., and Wang, C., 2012, Changes in Permeability Caused by Transient Stresses: Field Observations, Experiments and Mechanisms: Review of Geophysics, v. 50, doi: 10.1029/2011RG000382.

Manga, M., Brodsky, E.E., and Boone, M., 2003, Response of streamflow to multiple earthquakes: Geophys. Res. Lett , v. 30, doi: 10.1029/2002GL016618.

Mukuhira, Y., Moriya, H., Ito, T., Asanuma, H., and Haring, M., 2017, Pore pressure migration during hydraulic stimulation due to permeability enhancement by low-pressure subcritical fracture slip: Geophys. Res. Lett , v. 44, p. 3109–3118, doi: 10.1002/2017GL072809

Niemeijer, A., C. Marone, and D. Elsworth (2008), Healing of simulated fault gouges aided by pressure solution: Results from rock analogue experiments, J. Geophys. Res., 113, B04204, doi:10.1029/2007JB005376

Polak, A., Elsworth, D., Yasuhara, H., Grader, A.S., and Halleck, P.M., 2003, Permeability reduction of a natural fracture under net dissolution by hydrothermal fluids: Geophys. Res. Lett., v. 30, doi: 10.1029/2003GL017575.

Power, W. L., Tullis, T. E., Brown, S. R., Boitnott, G. N., & Scholz, C. H., 1987, Roughness of natural fualt surfaces. Geophysical Research Letters, 14(1), 29–32.

Power, W. L., and Tullis, T.E., 1992, The contact between opposing fault surfaces at Dixie Valley, Nevada, and implications for fault mechanics, J. Geophys. Res., 97(B11), 15425–15435, doi: 10.1029/92JB01059.

Renard, F., & Candela, T., 2017, Scaling of Fault Roughness and Implications for Earthquake Mechanics. In Fault Zone Dynamic Processes (eds M. Y. Thomas, T. M. Mitchell and H. S. Bhat). doi:10.1002/9781119156895.ch10

Tesei, T., Carpenter, B. M., Giorgetti, C., Scuderi, M. M., Sagy, A., Scarlato, P., & Collettini, C. (2017). Friction and scale-dependent deformation processes of large experimental carbonate faults. Journal of Structural Geology, 100, 12–23. https://doi.org/10.1016/j.jsg.2017.05.008

Van der Elst, N., Savage, H., Keranen, K., & Abers, G., 2013, Enhanced remote earthquake triggering at fluid-injection sites in the Midwestern United States. Science, 341.

Wang, C., and Manga, M., 2015, New streams and springs after the 2014 Mw6.0 South Napa earthquake: Nature Communications, v. 6, p. 1–6, doi: 10.1038/ncomms8597.

Wang, C.-Y., Liao, X., Wang, L.-P., Wang, C.-H., and Manga, M., 2016, Large earthquakes create vertical permeability by breaching aquitards: Water Resour. Res , p. 1–15, doi: 10.1002/2016WR018893.

Wang, C., Elsworth, D., and Fang, Y., 2017, Influence of weakening minerals on ensemble strength and slip stability of faults: J. Geophys. Res. Solid Earth, v. 122, doi: 10.1002/2016JB013687.

Witherspoon, P. A., Wang, J. S. Y., Iwai, K., & Gale, J. E., 1980, Validity of cubic law for fluid flow in a deformable rock fracture. Water Resour. Res., 16(6), 1016–1024, doi: 10.1029/WR016i006p01016.

Xue, L., Li, H.-B., Brodsky, E.E., Xu, Z.-Q., Kano, Y., Wang, H., Mori, J.J., Si, J.-L., Pei, J.-L., Zhang, W., Yang, G., Sun, Z.-M., and Huang, Y., 2013, Continuous permeability measurements record healing inside the Wenchuan earthquake fault zone: Science, v. 340, p. 1555–1559, doi: 10.1126/science.1237237.

Yasuhara, H., and Elsworth, D. 2008, Compaction of a rock fracture moderated by competing roles of stress corrosion and pressure solution. Pure and Applied Geophysics, 165(7), 1289–1306. https://doi.org/10.1007/s00024-008-0356-2

Yasuhara, H., Elsworth, D., and Polak, A., 2003, A mechanistic model for compaction of granular aggregates moderated by pressure solution: J. Geophys. Res., v. 108, doi: 10.1029/2003JB002536.

Yasuhara, H., Elsworth, D., and Polak, A 2004, Evolution of permeability in a natural fracture : Significant role of pressure solution: J. Geophys. Res., v. 109, p. 1–11, doi: 10.1029/2003JB002663.

Yasuhara, H., Polak, A., Mitani, Y., Grader, A. S., Halleck, P. M., & Elsworth, D., 2006, Evolution of fracture permeability through fluid-rock reaction under hydrothermal conditions. Earth and Planetary Science Letters, 244(1–2), 186–200. https://doi.org/10.1016/j.epsl.2006.01.046

Zoback, M.D., Kohli, A., Das, I., and McClure, M., 2012, The Importance of Slow Slip on Faults During Hydraulic Fracturing Stimulation of Shale Gas Reservoirs: SPE Journal, p. SPE 155476, doi: 10.2118/155476-MS.

Chapter 5

Conclusions

These prior studies explore the co-evolution of fault/fracture friction and permeability during static loading and dynamic reactivation. We investigate stable and unstable fault slip with full consideration of inertia in a rate and state frictional framework with a novel continuous numerical solution of spring slider motion. Furthermore, we investigate co-evolution of friction and permeability during static hold and reactivation with fluid-flowthrough experiments in a triaxial pressure cell. Here we repeat, verbatim, the conclusions from these various studies.

We demonstrate in Chapter 1 that the magnitude and recurrence of stick-slip motion is significantly controlled by the frictional state at the conclusion of the dynamic slip phase. The definition of healing in the rate and state framework demonstrates an essential and prominent physical property of healing in that frictional strengthening is rapid on weakly healed surfaces (small θ_i) and conversely slow on strongly healed surface (high θ_i). Therefore, for the same change of frictional state ($\Delta\theta$), healing can be significant with a small initial state while it may be negligible at a large initial state. This property suggests that the magnitude of healing at a given time should be scaled to initial state θ_i. In typical slide-hold-slide experiments, θ_i is always regulated by D_c/V_{lp}. We show that in log-linear healing, the cut-off time is scaled to D_c/V_{lp}.

As applied to earthquake faults, our results predict that higher earthquake slip velocity will cause a larger initial rate of frictional healing and therefore longer recurrence time with a given tectonic loading rate. Our novel continuous numerical solution of spring slider motion demonstrates that the cut-off recurrence interval in periodic stick-slip evolution also scales with frictional state at the conclusion of the dynamic slip process and that this frictional state can be evaluated from $\theta_i = D_c/V_{peak}$. Laboratory observations strongly support this explanation of evolution in friction drop. It is clearly shown that when peak velocity is slow the evolution of friction drop is delayed.

Using the numerical method developed in Chapter 1, we investigate dynamic effects on frictional stability and their characteristics in Chapter 2. We show that frictional stability on high velocity slipping contacts is indeed controlled by inertia and related to dynamic effects. Furthermore, we observe that these dynamic effects determine the dynamic characteristics of the resulting unstable slip motions: stick-slip and quasi-harmonic oscillation. Magnitudes of shear stress oscillations decrease with increased velocity in the quasi-harmonic (stick-slip) regime while, it significantly increases with velocity in the dynamic (quasi-harmonic oscillation) regime. Frequency increases with increased velocity but there exists a frequency limit at the natural frequency of the system. Dynamic frictional instability coefficient ($\eta = MV^2/\sigma a D_c$) is a key parameter that defines the potential for dynamic instability and determines the dynamic characteristics of unstable slip motions.

Fluid-flowthrough experiments in Chapter 3 demonstrate a cycle of the creation then destruction of permeability during laboratory slide-hold-slide experiments which substantially reproduce natural observations [Elkhoury et al., 2006]. We observe that both comminution and dilation can be driven by shear slip. The comminution effect is mostly dominant during initial shear-in on artificial fresh surfaces and for short healing/sealing periods – which may not be broadly representative of natural systems. Conversely, the effects of dilation become increasingly significant with the increased duration of healing – conditions much more representative of natural condition on faults subject to inter-seismic repose. During experimentally imposed periods of hold the permeability continuously declines, described by power law compaction and cubic law flow. Upon reactivation, the magnitude of permeability increase scales with an increase in repose period. Indeed, applying a substantial pre-reactivation repose period is essential to follow the correct path of permeability evolution present through the seismic cycle.

These results are further explored with longer term slide-hold-slide experiments with measurements of fault normal deformation *via* a strain gage and with the measurement of surface profiles *via* white light profilometry. The experimental results reconfirm that permeability response to shear slip is controlled by pre-slip sealing. During hold periods, normal deformation and hydraulic aperture compaction follow power law decay with a power exponent of ~ 0.2-0.4. The magnitude of the two (hydraulic and mechanically measured) compactions show a strong positive correlation but are not identical. Generally, hydraulic aperture decline is larger than the measured compaction with two exceptions at first holds. Shear permeability enhancements are also accompanied by shear dilation but again with some exceptions. Those observations imply that permeability cycles observed during fault repose and reactivation are controlled by chemo-mechanical compaction and mated surface dilation. However, there are more factors which can contribute to the complex behavior, such as mobilization of wear products.

Surface profile scans post-experiment show significant comminution during the experiments. This observation explains the strong permeability reduction observed during the initial shear-in of fresh laboratory prepared surfaces. The comminution effect is significantly reduced when the sample is reused for a back-to-back test. Micro scale roughness is developed on the top of the planed surface. We note that the magnitude of compaction observed in the experiment (a few microns) may increases the matedness of those micro-roughness contacts. If the mated contacts behave as a bottleneck on major flow paths, they can control overall permeability. Breaching the mated seal *via* shear slip can significantly enhance permeability.

Vita

Kyungjae Im

EDUCATION

The Pennsylvania State University 2013 – 2019

- Ph.D. (Candidate) in Energy and Mineral Engineering
- M.S. in Petroleum and Natural Gas Engineering (2015)

Seoul National University, 2007

- B.S. Major in Geoscience / Minor in Physics

PROFESSIONAL EXPERIENCES

Samsung Oil & Gas USA Corp, Houston, TX 2011 - 2013

- Associate Operation Manager / Asset Acquisition Task Force

Samsung C&T Corporation, Seoul, Korea 2007 – 2011

- Geologist, Oil and Gas Investment Division

RESEARCH EXPERIENCES

Research Assistant, The Pennsylvania State University 2014 - 2018

- Geophysical and mineralogical controls on the rheology of fracture slip and seal breaching
- Surface and subsurface geodesy combined with active borehole experimentation for the advanced characterization of EGS Reservoir
- DOE Geothermal technologies office – Code comparison study

JOURNAL PUBLICATIONS

- **Im, K**., Marone, C., Elsworth, D. (2019) The transition from steady frictional sliding to inertia-dominated instability with rate and state friction. **Journal of the Mechanics and Physics of Solids**. *DOI: 10.1016/j.jmps.2018.08.026*
- **Im, K**., Elsworth, D., Fang, Y. (2018) The influence of pre-slip sealing on the evolution of permeability on fractures and faults. **Geophys. Res. Lett.** *DOI:10.1002/2017GL076216*
- **Im, K**., Elsworth, D., Marone, C., Leeman, J. (2017) The impact of frictional healing on stick-slip recurrence interval and stress drop: Implications for earthquake scaling. **J. Geophys. Res: Solid Earth.** *DOI: 10.1002/2017JB014476*
- **Im, K**., Elsworth, D., Guglielmi, Y., Mattioli, G., (2017), Geodetic imaging of thermal deformation in geothermal reservoirs – production, depletion and fault reactivation. **J. Volcanol. Geotherm. Res**. Vol 338. pp 79-91, *DOI: 10.1016/j.jvolgeores.2017.03.021*

Summited / In revision

- **Im, K**., Elsworth, D., Wang, C., Experimental observation of permeability evolution of fracture and fault during repose and reactivation. **J. Geophys. Res: Solid Earth.** *In-revision*